Charged particle diagnostics for PETAL, calibration of the detectors and development of the demonstrator

Nesrine Rabhi

To cite this version:

Nesrine Rabhi. Charged particle diagnostics for PETAL, calibration of the detectors and development of the demonstrator. Other [cond-mat.other]. Université de Bordeaux, 2016. English. NNT : 2016BORD0339 . tel-01450052

HAL Id: tel-01450052

https://theses.hal.science/tel-01450052

Submitted on 31 Jan 2017

THÈSE PRÉSENTÉE

POUR OBTENIR LE GRADE DE

DOCTEUR DE

L'UNIVERSITÉ DE BORDEAUX

ÉCOLE DOCTORALE DES SCIENCES PHYSIQUES ET DE L'INGÉNIEUR
Astrophysique, plasmas et nucléaire

Par **Nesrine RABHI**

Charged particle diagnostics for PETAL, calibration of the detectors and development of the demonstrator

Sous la direction de : Jean-Eric DUCRET

Soutenue le 6 Décembre 2016 à Talence

Membres du jury :

M. MEVEL Eric, Professeur, Université de Bordeaux	Président
M. CECCOTTI Tiberio, Chargé de Recherche, CEA-Saclay	Rapporteur
M. MARGARONE Daniele, Directeur de recherche, Institut de Physique CAS, Prague	Rapporteur
M. DUCRET Jean-Eric, Professeur, Université de Bordeaux	Directeur de thèse
M. TATARAKIS Michael, Professeur, Technological Educational Institute of Crete (TEI of Crete)	Examinateur

Diagnostics de particules chargées pour PETAL, étalonnage des détecteurs and développement d’un démonstrateur

Résumé :

Afin de protéger leurs systèmes de détection de l'impulsion électromagnétique géante générée par l'interaction du laser PETAL avec sa cible, les diagnostics de PETAL seront équipés de détecteurs passifs. Pour les ensembles SEPAGE et SESAME, une combinaison d'Imaging Plates (IP) et de couches de protection de matériaux de grand numéro atomique sera utilisée, qui permettra: 1) d'assurer que la réponse des détecteurs sera indépendante de son environnement mécanique proche dans les diagnostics et donc homogène sur toute la détection, 2) de blinder les détecteurs contre les photons de haute énergie produits dans la cible de PETAL. Dans le travail présenté ici, nous avons réalisé des expériences d'étalonnage avec les IPs auprès d'installations générant des électrons, des protons ou des ions, dans le but de couvrir le domaine en énergie cinétique de la détection des particules chargées de PETAL, de 0.1 à 200 MeV. L'introduction a pour but de décrire les méthodes et outils utilisés au cours de cette étude. Le second chapitre présente les résultats de deux expériences réalisées avec des électrons dans le domaine d'énergie cinétique [5-180] MeV. Le troisième chapitre décrit une expérience et ses résultats avec les protons entre 80 et 200 MeV étaient envoyés sur nos détecteurs. Le quatrième chapitre est consacré à une expérience utilisant des protons et des ions entre1 et 22 MeV en énergie de protons et dont l'objectif était l'étude de détecteurs et le test du démonstrateur de SEPAGE. Nous avons utilisé GEANT4 pour l'analyse de nos données et prédire la réponse de nos détecteurs dans le domaine 0.1 à 1000 MeV.

Mots clés: Imaging Plates, Les diagnostics PETAL+, physiques des plasmas, l'interaction laser matière, simulation GEANT4, accélération de particules par laser, détection de particules

Charged particle diagnostics for PETAL, calibration of the detectors and development of the demonstrator

Abstract :

In order to protect their detection against the giant electromagnetic pulse generated by the interaction of the PETAL laser with its target, PETAL diagnostics will be equipped with passive detectors. For SESAME and SEPAGE systems, a combination of imaging plate (IP) detectors with high-Z material protection layers will be used to provide additional features such as: 1) Ensuring a response of the detector to be independent of its environment and hence homogeneous over the surface of the diagnostics; 2) Shielding the detectors against high-energy photons from the PETAL target. In this work, calibration experiments of such detectors based on IPs were performed at electron and proton facilities with the goal of covering the energy range of the particle detection at PETAL from 0.1 to 200 MeV. The introduction aims at providing the reader the methods and tools used for this study. The second chapter presents the results of two experiments performed with electrons in the range from 5 to 180 MeV. The third chapter describes an experiment and its results, where protons in the energy range between 80 and 200 MeV were sent onto detectors. The fourth chapter is dedicated to an experiment with protons and ions in the energy range from 1 to 22 MeV proton energy, which aimed at studying our detector responses and testing the demonstrator of the SEPAGE diagnostic. We used the GEANT4 toolkit to analyse our data and compute the detection responses on the whole energy range from 0.1 to 1000 MeV.

Keywords : Imaging Plates, PETAL+ diagnostics, particle diagnostics, plasma physics, laser-matter interaction, GEANT4 Monte Carlo simulations, laser acceleration of particles, detection

---

CELIA centre lasers intenses et applications
Laboratoire CELIA UMR5107
CNRS, CEA, Université de Bordeaux
43 Rue Pierre Noailles Bât C6
33400 TALENCE

Remerciements

First of all, I would like to thank the CELIA director, Philippe Balcou, for welcoming me in the laboratory that allowed to make my dream of obtaining PhD degree in physics possible.

I am enormously grateful to Jean-Eric Ducret for accepting to be the director of my thesis. I appreciate the time and effort you spent guiding me in my work. You did not only taught me how to prepare and perform experiments but also provided valuable insights in difficult moments when I felt stuck in writing the code of my GEANT4 simulations and sacrificed a lot of time to help me progress in my work. Thank you also for allowing me to travel around Europe and to present parts of this work to the scientific community. And last but not least, thank you for your kindness and humanity.

I am very grateful to all members of the defence committee: Tiberio Ceccotti and Daniele Margarone, who spent a huge amount of time reading, understanding and commenting on this work. Their comments and questions helped me greatly to improve the quality of the thesis. I equally value help of Eric Mevel, his decision to accept to be the president of the defence committee, and his kindness and friendliness during three years of my studies. I am very grateful to Michael Tatarakis as well for becoming a member of the defence committee and for taking a long trip from Crete to Bordeaux. Your participation was an honor as the summer school in Crete, which you organized, was one of the first steps on the way to obtain my PhD degree. It helped me a lot to deepen my knowledge and I made many new friends there.

An important part of my work was performing experiments. Therefore, I sincerely thank to Benjamin, Isabelle, Anna−Lisa, Catherine, Cedric, Kim, Jean-Paul, Alain and Philippe, who I collaborated with during the experimental campaigns, and their work is thus related to my success.

CELIA laboratory offered perfect conditions for work during all my studies. I am very grateful to Celine for her support since my first day and her help not only in solving administrative issues. My thanks also belong to Sonia for her kindness and sympathy.

I want to thank particularly to all my colleagues from CELIA laboratory,

namely to Dimitri, Katarzyna, Joao, Fabien, Sebastien, Guillaume, Georgiaan, Jonathan, Mathieu, Timea, Mokrane, Oliver, Julien, Gabriel, Dario, Pierre, Basil and Lorenzo.

I am enormously grateful to my parents for the unswerving support during all my life. Their tenderness, love and advices always help me to overcome hard moments and stand up again to continue my way.

And thank you, my dear husband Karel, for supporting me since the first day we met. You helped me to understand many problems in physics, you stand next to me in all difficult moments and you always believe in my success. I feel lucky to have a person like you to share my life with.

Publications related to this thesis

Some results from this PhD research work:

1. N. Rabhi, K. Bohacek, D. Batani, G. Boutoux, J.-E. Ducret, E. Guillaume, K. Jakubowska, C. Thaury, and I. Thfoin., Rev. Sci. Instrum. **87**, 053306 (2016)
2. N. Rabhi et al., Calibration and response functions of imaging plates detectors between [1-220 MeV] protons for PETAL+ diagnostics. To be submitted in RSI
3. G. Boutoux, N. Rabhi, D. Batani, A. Binet, J.-E. Ducret, K. Jakubowska, J.-P. Nègre, C. Reverdin, I. Thfoin. Rev. Sci. Instrum. **86**, 113304 (2015)
4. F. Ingenito, G. Boutoux, M. Cipriani, F. Consoli, G. Cristofari, A. Curcio, R. De Angelis, G. DiGiorgio, J.-E. Ducret, P. Forestier-Colleoni, S. Hulin, K. Jakubowska, N. Rabhi et al. JINST **11** C05012 (2016)
5. G. Boutoux, D. Batani, F. Burgy, J.-E. Ducret, P. Forestier-Colleoni, S. Hulin, N. Rabhi, A. Duval, L. Lecherbourg, C. Reverdin, K. Jakubowska et al., Rev. Sci. Instrum. **87**, 043108 (2016)

Some results have been partially presented in the following conferences and workshop:

1. Forum Lasers et Plasmas, Orcières−Merlette, France, 2014 (poster)
2. COST LMJ Workshop, Bordeaux, France, 2014 (poster)
3. Workshop PETA−phys and PETAL+, Bordeaux, France, 2015 (oral)
4. 1st EPS Conference on Plasma Diagnostics, Frascati, Italy, 2015 (Poster)
5. 42nd EPS Conference on Plasma Physics, Lisbon, Portugal, 2015 (Poster)

6. OPTIQUE Bordeaux 2016, Bordeaux, France, 2016 (oral)

and in the following graduate schools:

1. HIPOLIN Erasmus Intensive Programme, Rethymno, Crete, 2014 (Poster)

2. École d'Aquitaine Ondes et Matière, Les phénomènes de transport dans les plasmas chauds, Bordeaux, France, 2014 (Poster)

0.1 Abstract

In order to protect their detection against the giant electromagnetic pulse generated by the interaction of the PETAL laser with its target, PETAL diagnostics will be equipped with passive detectors. For SESAME and SEPAGE systems, a combination of imaging plate (IP) detectors with high-Z material protection layers will be used to provide additional features such as: 1) Ensuring a response of the detector to be independent of its environnement and hence homogeneous over the surface of the diagnostics; 2) Shielding the detectors against high-energy photons from the PETAL target.

In this work, calibration experiments of such detectors based on IPs were performed at electron and proton facilities with the goal of covering the energy range of the particle detection at PETAL from 0.1 to 200 MeV. The introduction aims at providing the reader the methods and tools used for this study. The second chapter presents the results of two experiments performed with electrons in the range from 5 to 180 MeV. The third chapter describes an experiment and its results, where protons in the energy range between 80 and 200 MeV were sent onto detectors. The fourth chapter is dedicated to an experiment with protons and ions in the energy range from 1 to 22 MeV proton, which aimed at studying our detector responses and testing the demonstrator of the SEPAGE diagnostic. We used the GEANT4 toolkit to analyze our data and compute the detection responses on the whole energy range from 0.1 to 1000 MeV.

Keywords: Imaging Plates, PETAL+ diagnostics, Particle diagnostics, plasma physics, laser−matter interaction, GEANT4 Monte Carlo simulations,, laser acceleration of particles, detection

0.2 Resumé

Afin de protéger leurs systèmes de detection de l'impulsion électromagnétique géante générée par l'interaction du laser PETAL avec sa cible, les diagnostics de PETAL seront équipés de detecteurs passifs. Pour les ensembles SEPAGE et SESAME, une combinaison d'Imaging Plates (IP) et de couches de protection de matériaux de grand numéro atomique sera utilisée, qui permettra: 1) d'assurer que la réponse des détecteurs sera indépendante de son environnement mécanique proche dans les diagnostics et donc homogène sur toute la détection, 2) de blinder les détecteurs contre les photons de haute énergie produits dans la cible de PETAL.

Dans le travail présenté ici, nous avons réalisé des expériences d'étalonnage avec les IPs auprès d'installations générant des électrons, des protons ou des ions, dans le but de couvrir le domaine en énergie cinétique de la détection des particules chargées de PETAL, de 0.1 à 200 MeV. L'introduction a pour but de décrire les méthodes et outils utilisés au cours de cette étude. Le second chapitre présente les résultats de deux expériences réalisées avec des électrons dans le domaine d'énergie cinétique [5-180] MeV. Le troisième chapitre décrit une expérience et ses résultats avec les protons entre 80 et 200 MeV étaient envoyés sur nos détecteurs. Le quatrième chapitre est consacré à une expérience utilisant des protons et des ions entre 1 à 22 MeV en énergie de protons et dont l'objectif était l'étude de détecteurs et le test du demonstrateur de SEPAGE.

Nous avons utilisé GEANT4 pour l'analyse de nos données et prédire la réponse de nos détecteurs dans le domaine 0.1 à 1000 MeV.

Mots clés: Imaging Plates, Les diagnostics PETAL+, physiques des plasmas, l'interaction laser matiéres, simulations GEANT4, accélération de particules par laser, détection de particules

Contents

List of Figures

Chapter 1

Introduction

The subject of my thesis is the development and calibration of the charged-particle detectors of the PETAL+ project. This chapter introduces the elements that will be used in the following chapters. I will present shortly the Laser MegaJoule (LMJ), the Petawatt Aquitaine Laser (PETAL), the PETAL+ project and its diagnostics, the simulation GEANT4 used to analyze our results and the passive detectors named imaging plates (IP).

1.1 The Laser Megajoule

The Laser MegaJoule (LMJ) is installed in le Barp, Bordeaux, France. This facility will be composed of 176 laser beams that will deliver 1.8 MJ to a target using the method of indirect drive [1], and a maximum power of 550 TW of 0.35 μm UV light on target with a typical pulse duration of a few ns (see Fig. 1.1 and Tab.1.1). The interaction chamber of LMJ is an aluminum sphere of 140 tons and 10 m diameter equipped with a plasma and laser diagnostics and contains the target at its center.

The 176 beams located in LMJ sphere are assembled into 22 bundles of 8 beams. Each bundle is composed of two quadruplets (set of four beams). Each quadruplet should deliver up to 30 kJ of energy with a duration of a few ns, and provide intensity of 10^{15} W/cm^2.

The scientific cases of LMJ and the National ignition Facility (NIF) in the

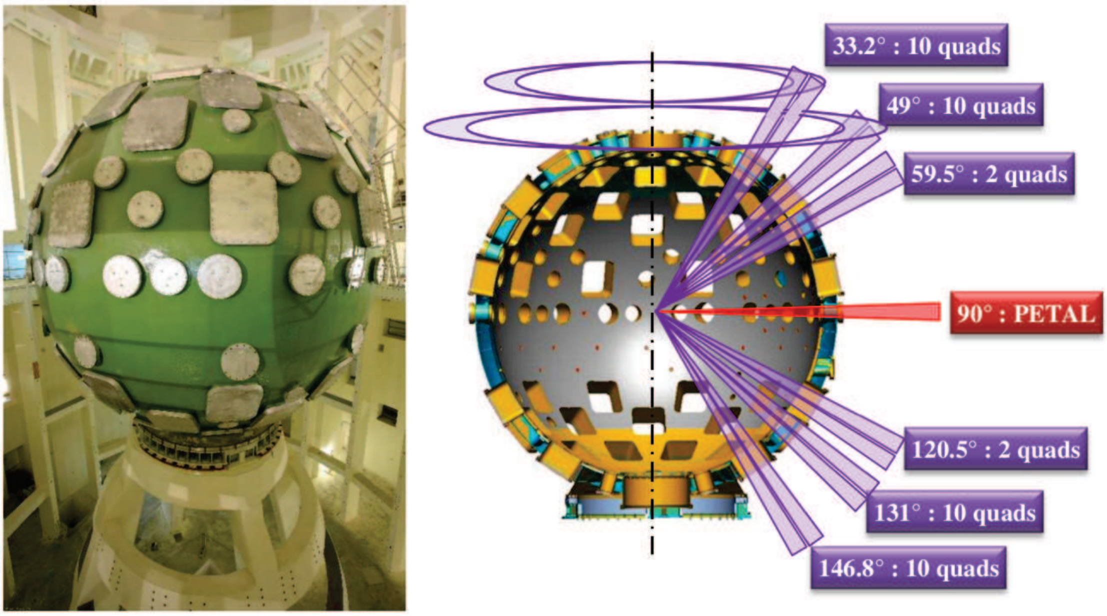

Figure 1.1: Geometry of the LMJ sphere. [1].

United States have many features in common and have been presented in [2] and [3] respectively. Both facilities will take advantage of their large number of ns high-energy beams, to setup experiments usually distributed in three categories:

- High-energy density physics, where relatively low temperatures (a few eV) at extremely high pressure (above TPa) and matter density will be studied,

- Laboratory astrophysics, where experiments aiming either at studying the microphysics of steller plasmas or astrophysical phenomena such as shocks will be performed,

- Studies for inertial confinement fusion by direct drive, within the scope of reaching conditions for the production of energy.

1.2 The Petawatt Aquitaine Laser

The PETawatt Aquitaine Laser (PETAL) is a kJ multi-Petawatt beam coupled with the LMJ facility. Tab.1.1 presents the characteristics of the PETAL and LMJ lasers.

The short pulse of PETAL will be used either directly on LMJ targets or to accelerate particles from a specific target. The secondary accelerated particles may be used, for example, to probe an imploding LMJ target. TNSA (Target Normal Sheath Acceleration) [4], [5], [6], [7] is the main physical mechanism at play to accelerate particles with PETAL.

	PETAL	1 Quad LMJ
Energy (kJ)	> 3	30
Wavelength (nm)	1053	351
Pulse duration	$0.5 - 10$ ps	a few ns
Intensity on target W/cm^2	10^{20}	$>$ a few 10^{15}
Intensity contrast (short pulse)	10^{-7} at -7 ps	
Energy contrast (long pulse)		10^{-3}

Table 1.1: Characteristics of the PETAL and LMJ laser system.

In the TNSA mechanism (see Fig. 1.2), the ions and protons are indirectly accelerated by the short-pulse laser. In fact, the laser couples to the plasma electrons, which are accelerated by the ponderomotive force. The heated electrons propagate throughout the thin target (typically a PETAL target will be a few-micrometer thick, depending on the experiment) to reach the back surface, where a part of them escape into vacuum. These escaping electrons create behind them an electric force, which pulls the surface ions out of the target and accelerate them. Note that the TNSA mechanism has been extensively studied experimentally (see e.g. [8], [9] and [10]).

The diagnostics being built in the framework of the PETAL+ project (EquipEx) will have as a first goal to study the particle acceleration mechanism occuring with the PETAL target. For such a study, the energy spectra of the accelerated particles (electrons, protons and ions) have to be determined. This will be the purpose of the SESAME and SEPAGE diagnostics.

Furthermore, to get a deeper insight into the TNSA mechanism, the hot-electron transport through the PETAL target has to be studied. This will be the purpose of the hard-X ray spectrometer SPECTIX, using the method of the K$_\alpha$ excitation process in a multi−layer target.

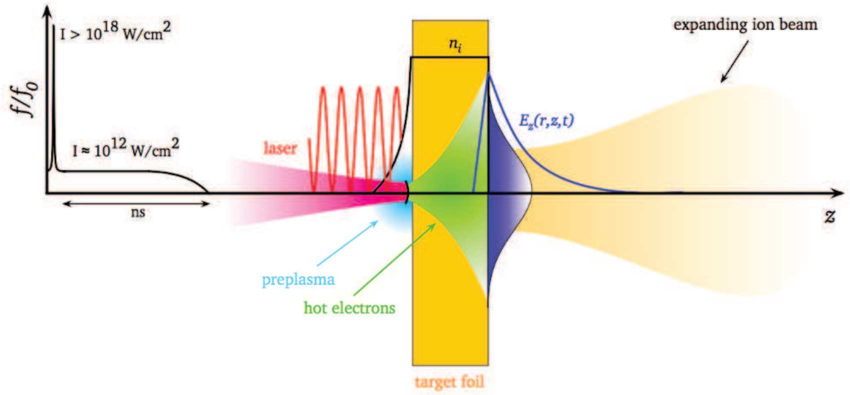

Figure 1.2: The TNSA mechanism [8].

1.3 The PETAL diagnostics

The goal of the PETAL+ project [11, 12] is to design and build diagnostics dedicated to the experiments with PETAL. It is also meant to produce dedicated insertion systems. The diagnostics include:

- SPECTIX, a hard X-ray photon spectrometer in the energy range [5,100] (keV).
- A set of charged particle diagnostics:
  - SEPAGE, a spectrometer that measures at 0 degree with respect to the PETAL target normal, the energy spectra of the particles emitted from the interaction point of PETAL on its target, and going to be positioned inside the LMJ sphere by a System for Insertion of Diagnostic (SID);
  - CRACC: the proton radiography detector of the LMJ plasmas;
  - SESAME, a set of two magnetic spectrometers which will determine the

angular distribution of the electron, proton and ion energy spectra around the PETAL axis.

The geography of the positioning of the PETAL+ diagnostics in the equatorial plane of the LMJ sphere is given in Fig. 1.3.

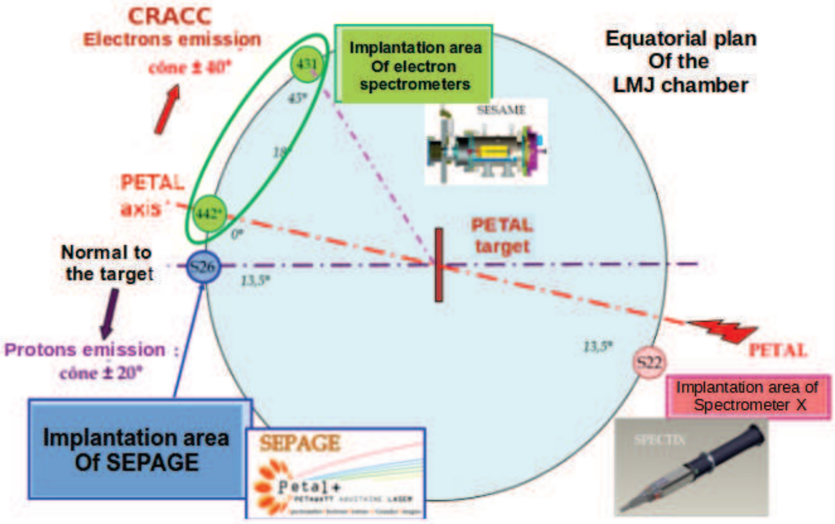

Figure 1.3: Geometry of the PETAL diagnostics in the equatorial section of the LMJ chamber [15].

1.3.1 SPECTIX

SPECTIX is a large band X−ray spectrometer [13]. Its spectral range will span from 5 to $\sim$ 100 keV, permitting the detection of K_α emission lines from titanium to uranium. Its resolution, between 1/100 and 1/300 will enable to distinguish the $K_{\alpha 1}$ and $K_{\alpha 2}$ lines. The spectrometer is based on the Cauchois optics [14] using crystals in transmission. SPECTIX will include two channels of measurement, each equipped with its own crystal. The photons will be detected with Imaging Plates. Moreover, SPECTIX will be equipped with a dipole magnet at its entrance in order to deviate the high-energy electrons away from the detector and from the crystals.

SPECTIX works on the principle that the number of K_α detected photons is directly linked to the number of hot electrons going through the PETAL target with an energy above the K_α transition. Each elements works, inside the target, as a sort of energy threshold detector.

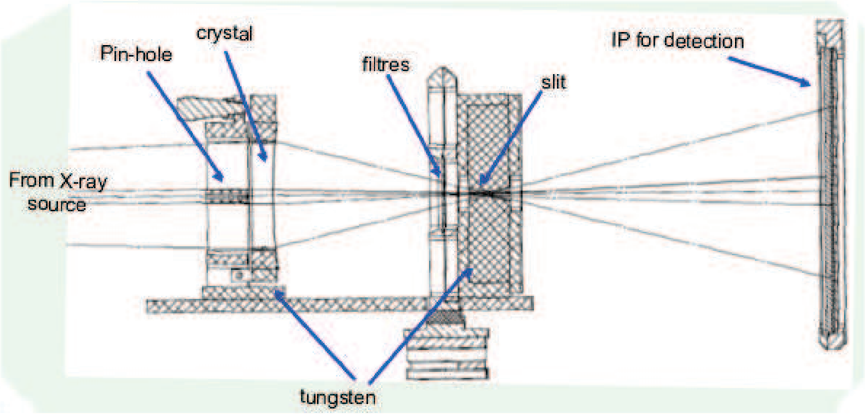

Figure 1.4: Optics of the SPECTIX spectrometer [13].

1.3.2 SEPAGE

The diagnostic named Spectromètre d'Électrons et de Protons A Grande Énergie (SEPAGE) (see Figs. 1.5, 1.6) will be positioned inside the LMJ sphere on the normal to the PETAL target at 13.5° with respect to the laser PETAL axis (see Fig. 1.3) with a System for Insertion of Diagnostic (SID). SEPAGE is composed of two Thomson parabolas that deflect particles with electric and magnetic fields, determining their energies and identifying them. Charged particles will be detected in two channels:

- A so-called "low-energy" channel for particles (electrons, ions and protons) above 0.1 MeV
- A "high-energy" channel for particles above 8 MeV kinetic energy

The specifications during the design of both channels in SEPAGE are:

- an energy resolution of better than 10% over the whole energy range, for electrons, protons and ions ($^{12}\mathrm{C}^{q+}$ were used along with protons in the calculations of the magnetic and electric transport in SEPAGE)

- Enough electric field strength to separate $^{12}\mathrm{C}^{6+}$ tracks from protons at:

- 20 MeV proton kinetic energy in the low-energy channel

- 150 MeV proton kinetic energy in the high-energy channel.

Notice that in the numbers given here, the track separations are provided for a given magnetic rigidity, p/q where p is the particle momentum and q its charge. This corresponds to the kinetic energy of an ion A^{q+} of mass m_A for the same magnetic rigidity, as for proton of kinetic energy E_p, which is given by:

$$\mathrm{E}(\mathrm{A}^{q+}) = q^2 \frac{m_p}{m_A} E_p \tag{1.1}$$

where m_p is the proton mass.

These specifications on the separating power of $^{12}\mathrm{C}^{6+}$ and protons in the low and high-energy channels fix the values of the electric field integrals of both channels. It should be underlined that as computed with the simulations, the separation of the $^{12}\mathrm{C}^{6+}$ and $^{12}\mathrm{C}^{5+}$ tracks is not possible for the highest magnetic rigidities in the low-energy channel [15].

The magnet strengths of both channels are constrainted by:

- The required energy resolution;

- The available transverse space inside the mechanics of the diagnostic, itself limited by the dedicated insertion system used to install the diagnostic in the LMJ chamber;

- The minimal detected proton and electron kinetic energies : 0.1 and 8 MeV in the low and high-energy channels respectively, for both electrons and protons.

Both channels of SEPAGE have their respective collimators. The hole diameters were chosen so as:

- To provide a sufficient energy resolution for protons and electrons at the highest specified energies in each channel (respectively 20 and 150 MeV);

- To be as large as possible, in order to remain feasible mechanically and provide as large as possible solid angles. The low-energy channel Thomson Parabola has a collimator of 200 μm diameter. The diameter of the high-energy channel collimator is 500 μm.

Taken into account their distance to the PETAL targets, they span solid angles of the order of 10^{-8} sr. A calculation performed with this geometry from the predictions of pic codes [16] could show that there remains a large amount of signal on the detectors, for electrons and protons [18].

The calculation used in the last chapter of this manuscript for the calibration of transport of ions in the low-energy channel Thomson Parabola of SEPAGE are given in appendix A. It should be underlined here that in both channels of SEPAGE the transport of electron does not follow the same line of the paraxial approximation (small deviation angles and transverse displacements with respect to the initial direction of the particles), especially for the lower part of their kinetic energy ranges. For these parts of the energy ranges, the electrons are bent at very large angles in SEPAGE (almost 90° with respect to the initial direction). This has put constraints on the design of the dipoles of both channels which had, in particular, to be either open on one side or rather wide in the dispersive direction, orthogonal to the dipole field.

The detection of particles will be based on passive imaging plates as will be detailed below. These detectors will be positioned at different places depending on the type of particles and their energies as shown in Figs. 1.5 and 1.6.

Different particle types are created in the interaction of the PETAL laser shot with its target. The goal of SEPAGE is to measure the energy spectra of protons, ions and electrons and to discriminate protons and ions (carbon, oxygen. . .) above 100 keV and up to 150-200 MeV (proton energy).

The SEPAGE spectrometer is composed of two additional elements, besides the detectors and Thomson Parabolas, which are the SID (Systemes d'insertion des diagnostics) and the BTDP (Boite de Transfert des Diagnostics Plasma). All these systems are shortly described below.

Systeme d'Insertion de Diagnostic (SID)

The système d'Insertion de Diagnostic (SID) allows to move the spectrometer into the chamber. The SID is rotatable and translatable in the X, Y and Z axis in

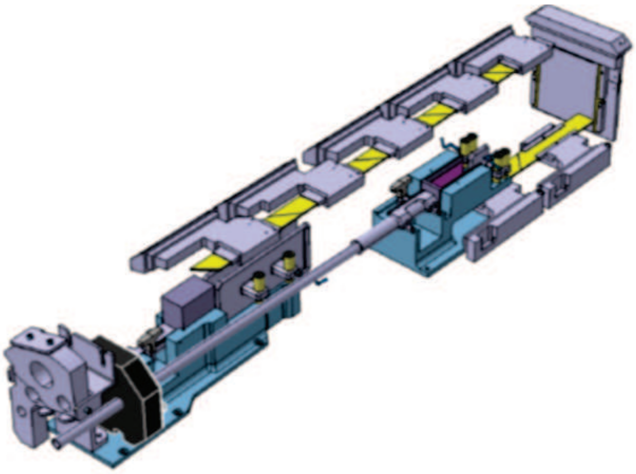

Figure 1.5: The design of the SEPAGE: the two Thomson Parabolas ("low−energy" and "high−energy" channels) and their related detectors.

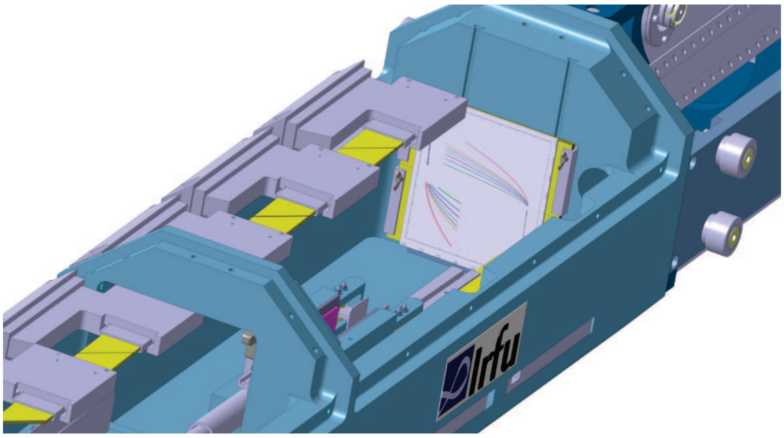

Figure 1.6: Zoom on the detection area (electrons and ions) [15]. The lateral electron detectors are shown in yellow color. The detector for high-energy electrons (on the upper side) is 100 cm long, and the detector for low-energy electrons (on the lower side) is 40 cm long. The front detectors for protons, ions, and electrons are shielded by 5 mm of tungsten placed behind.

order to adjust the distance between the center of the chamber and the position of the diagnostics. This SID has been designed and built especially for PETAL+ (SEPAGE and SPECTIX) from a design of the LMJ SID.

Boite de Transfert de Diagnostic Plasma (BTDP)

A transfer box called Boite de Transfert de Diagnostic Plasma (BTDP) allows to transfer the diagnostics and to collect the detectors after the laser shot and do basic maintenance of the diagnostics.

1.3.3 SESAME

The spectrometers called Spectromètres ÉlectronS A Moyenne Énergie (SESAME) will be placed on the wall of the LMJ chamber at 0° and 45° with respect to the PETAL laser axis (see Fig. 1.3).

The main goal of this set of two spectrometers is to sample the angular distribution of the electrons accelerated with PETAL and measure the energy spectrum of electrons at these two angles. As such the "active" part of this diagnostic is a dipole magnet, there is no requirement for a separation of ion species as in a Thomson Parabola. This dipole magnet will bend the electrons passing through the entrance collimator towards a detector which will be mechanically installed on a plane parallel to the dipole and diagnostic entrance axis (see Fig. 1.7). An additional detector will be installed at the bottom of the detection volume, orthogonal to the diagnostic entrance direction, to provide the 0° deflection spot, which will be used in the data analysis to reconstruct the energy spectrum from the dispersion on the detectors.

As shown by the long-dashed lines in Fig. 1.7, SESAME spectrometers will be equipped with detection planes symmetric to the electron detector with respect to the dipole axis, to provide detection capabilities for protons and ions.

The dipole magnet's characteristics were chosen to provide enough bending power for the high-energy tail of the electron distribution computed with particle-in-cell simulations performed specifically for the PETAL laser (around 150 MeV maximum energy). As a consequence, there is a threshold energy for the SESAME spectrometer below which the electrons don't escape from the field lines of the magnet, which is 5 MeV, as shown by dedicated Monte Carlo simulations performed for the design of the SESAME spectrometers [19]. The presence of such a detection threshold is by no mean a problem since the practical aim of the SESAME spectrometers is to provide an indication of the "quality" of PETAL laser shot interaction with its target, the high-energy part of the electron distribution being the most sensitive to the acceleration mechanism.

Let's mention here that this energy threshold of 5 MeV for electrons corresponds to a different threshold for the protons. The reason of this is the difference in magnetic rigidity of these two types of particles, as measured by the ratio m/q, where m is the particle mass and q its charge. Let $\mathrm{R_{th}}$ be the bending radius, in the magnetic field of SESAME of 5 MeV electrons. The condition for the protons to get out of the same dipole magnet is to have a bending radius of at least $\mathrm{R_{th}}$. We have:

$$\mathrm{R_{th}} = \frac{\mathrm{m_e}\gamma_\mathrm{e}\beta_\mathrm{e}}{\mathrm{eB}} = \frac{\mathrm{m_p}\gamma_\mathrm{p}\beta_\mathrm{p}}{\mathrm{eB}} \tag{1.2}$$

since protons and electrons have the same charge (e), in absolute value of course. In the equation above, the quantities are indexed for electrons and protons, $\beta = \mathrm{v/c}$ is the reduced velocity and γ is the Lorentz factor.

5 MeV electrons are relativistic with a Lorentz factor $\gamma_\mathrm{e} \sim 11$. For those electrons, we have therefore $\beta \sim 1$. To solve in proton kinematics the equation above, we have:

$$\mathrm{m_p}\gamma_\mathrm{p}\beta_\mathrm{p} = \gamma_\mathrm{e}\mathrm{m_e} \tag{1.3}$$

given that $\mathrm{m_e/m_p} \sim 1/1800$, it follows that $\gamma_\mathrm{p}\beta_\mathrm{p} << 1$, which means in particular that $\gamma_\mathrm{p} \sim 1$ and $\beta_\mathrm{p} << 1$. The reduced velocity of the protons at the detection threshold in SEPAGE is therefore:

$$\beta_\mathrm{p} = \gamma_\mathrm{e}\frac{\mathrm{m_e}}{\mathrm{m_p}} \simeq 6.10^{-3} \tag{1.4}$$

This gives an energy threshold (non relativistic protons):

$$\mathrm{E_p} = \frac{1}{2}\mathrm{m_p}\beta_\mathrm{p}^2 = \frac{1}{2}\frac{\gamma_\mathrm{e}^2\mathrm{m_e^2}}{\mathrm{m_p}} \simeq \ 17\ \mathrm{keV} \tag{1.5}$$

This value of the minimal kinetic energy of the detected protons in SESAME will put a constraint on the detectors to be used for the protons and ions in this set of spectrometers.

Fig.1.8 shows a detailed drawing of a SESAME spectrometer, with its tungsten entrance shielding its collimator, dipole magnet detectors and vaccuum system. Notice that contrary to a Thomson Parabola, the transport of charged particles in the dipole magnet requires to form a point like source only in the dispersive direction, orthogonal to the dipole field and the entrance direction. Therefore, the SESAME entrance collimation system is not a cylindrical one, as in SEPAGE, but an adjustable slit, to be set as a compromise between solid angle and energy resolution.

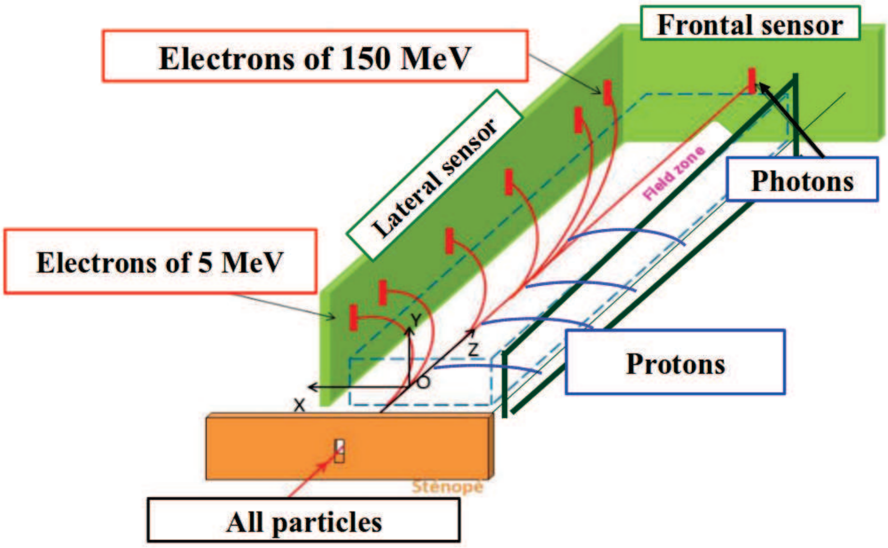

Figure 1.7: Illustration of functioning of the SESAME spectrometer [19].

The solid angle of SESAME is in the order of 10^{-7} sr.

1.3.4 CRACC

The CRACC (cassette de radiographie au centre chambre) is a proton radiography detector that measures the divergence of the PETAL proton beam (see Fig. 1.3) as a function of the proton energy. Eventually CRACC will be placed 100 mm from the target in front of SEPAGE. It will be equipped with Radiochromic films (RCF) [20].

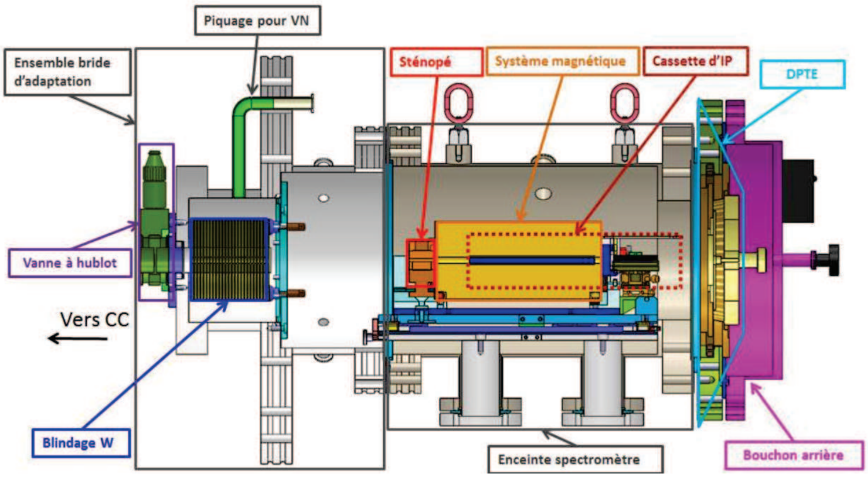

Figure 1.8: Drawing of SESAME, showing the mechanical structure and the shielding [19].

1.4 Imaging Plates (IP)

1.4.1 Detector description

Imaging Plates have been chosen as passive detectors for the PETAL diagnostics SESAME, SEPAGE and SPECTIX. Imaging Plates are commercialized by Fuji since 1980s [21], and in the beginning, they were used for medical purposes and X-ray imaging. Quickly, they started to be used as detectors of particle beams accelerated by laser [22, 23, 24, 25].

Imaging Plates (IP) or photostimulable phosphoric plates are detectors of roughly 500 μm total thickness, sensitive to ionizing particles and composed of three or four layers. Five types of IP produced by Fujifilm are used in our experiments (MS, SR, TR, MP and ND). Fig. 1.9 shows three types of IPs. We can distinguish the IP types by their phosphoric atomic compositions, their thicknesses, the compositions and the number of the different layers (see Tab. 1.2). The TR IP does not contain a protective layer. IPs are flexible to precise positioning and minimize distortion (see Fig. 1.10). Note that the compositions of BAS-MP and BAS-ND are unknown to us. Therefore we didn't do simulations of the interaction of ionizing particles with these two types of detectors.

The particle beams generated by a laser-plasma interaction have certain characteristics (e.g flux of particles, intensity...) that make diodes or photomultipliers difficult to use due to the saturation by the flux, or the perturbed reading of the detection electronics by the high electromagnetic field generated by the interaction of the laser with its target. For these reasons, using passive IP is an advantageous way in these conditions. They can be used in vacuum or in air, they are reusable many times. A big advantage of IP is the achievable position resolution (tens of μm). Perhaps their most important characteristic is their large dynamic range, roughly 8 orders of magnitude as discussed in [26], which is larger than the Radiochromic films (RCF) values [20].

Figure 1.9: Imaging plates Fuji BAS-MS, BAS-SR, BAS-TR.

Figure 1.10: Flexibility of imaging plates.

Layer	SR	MS	TR
PROTECTIVE			
Composition	C_2H_2	C_2H_2	No layer
Density (g.cm^3)	1.273	1.66	0
Thickness (μm)	6	9	0
SENSITIVE			
Composition	BaFBr : Eu	$BaFBr_{0.85}I_{0.15}$: Eu	$BaFBr_{0.85}I_{0.15}$: Eu
Density (g.cm^3)	3.1	3.31	2.85
Thickness (μm)	120	115	50
SUPPORT			
Composition	C_2H_2O		
Density (g.cm^3)	1.237	1.66	1.66
Thickness (μm)	188	190	250
MAGNETIC			
Composition	$ZnMn_2Fe_5NO_{40}H_{15}C_{10}$		
Density (g.cm^3)	3.1	2.77	2.77
Thickness (μm)	160	160	160

Table 1.2: Atomic compositions, densities and thicknesses of three types of IPs: Fuji BAS-SR, MS and TR. (From T. Bonnet [29]).

After the irradiation, IPs are placed into a scanner for the digitalization of the detected signal. When the readout is finished, the IP is placed into a dedicated instrument to erase the signal using white light (an eraser, see Fig. 1.11).

The intensity of the signal is related to the number of electron-hole pairs created by the particles in the IP active layer (see section 1.5 for the explanation of the Photoluminescence principle).

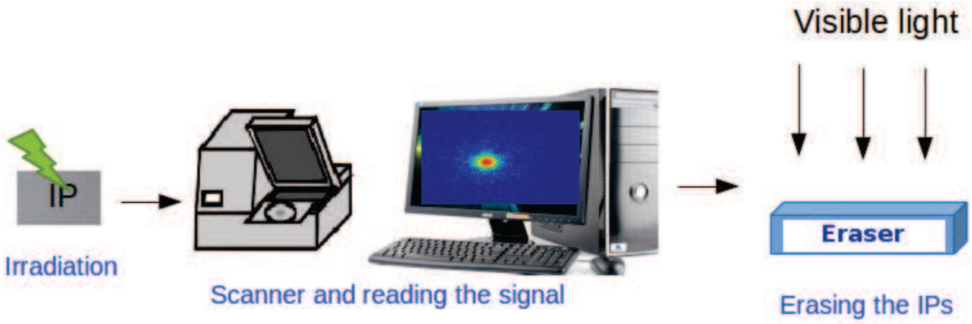

Figure 1.11: Scanning process of IP signal.

One of the goals of this thesis is to determine the absolute efficiency or response of our detectors to particles in an energy range (tens of MeV) corresponding to what is expected at PETAL, where published data were scarce or incoherent when we started this work [22, 23, 27, 28, 29] (see Figs.1.12, 1.13). Such a calibration of the absolute efficiency (response) will allow to determine the absolute spectra of particles emitted by the interaction of the PETAL laser with its target.

For the sake of completeness, it must be underlined here that the choice of imaging plate based detectors was not fully obvious when the PETAL+ project started. Other alternatives such as Radiochromic Films (RCF) [30], [31], [32] or CR39 detectors were discussed. Lanex screens [33] did not represent a solution for us since they require an electronic readout on the experimental setup and could not respond to the project needs. The CR39 option was discussed in the PETAL+ project team. A regulation problem arose them, linked to the rule in the LMJ-PETAL facility that everything which is put into the vacuum of the LMJ chamber has to be considered as contaminated. This means in particular that etching of the CR39 detectors, if this technology was chosen, has to be done in glove boxes. This happens to be either unpractical or expensive (or both).

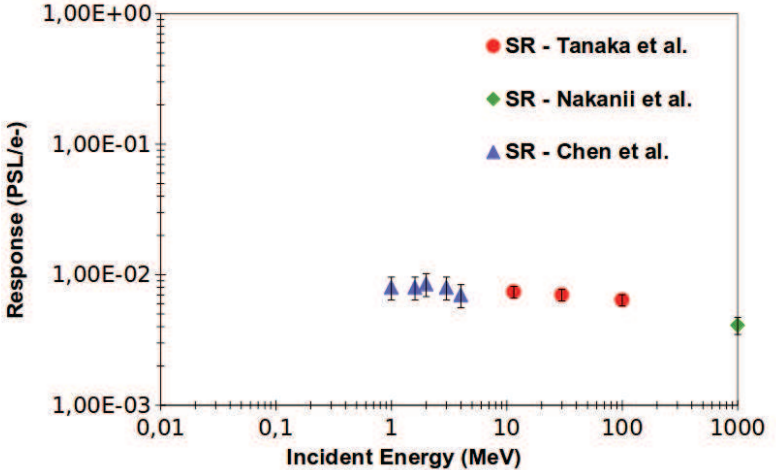

Figure 1.12: The existing data on IP responses to electrons when this work was begun.

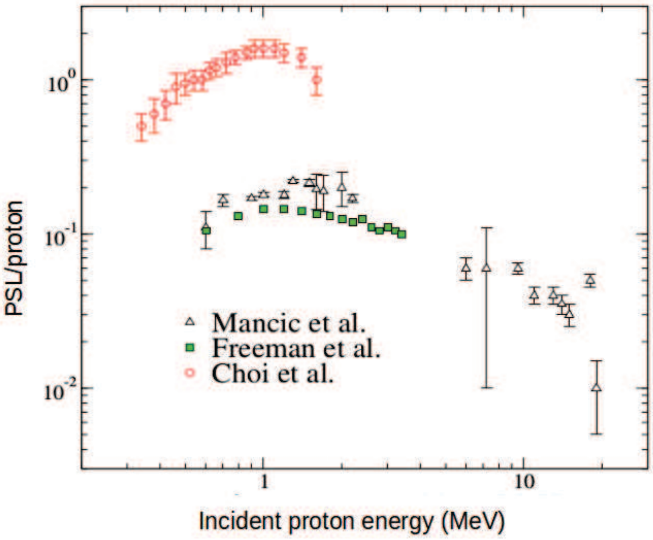

Figure 1.13: The existing data of TR IP responses to protons when this work was begun [29].

Moreover, as for the performances of CR39 to few tens of MeV protons, nothing proved at that time that they were noticeably more efficient than Imaging Plates. We can also add that the protons in this energy range punch rather small holes at the surfaces of CR39, whose counting after the etching process may depend on the etching time, which could have therefore produced physics signals dependent on the etching method. All in all, this technology was not chosen.

Radiochromic films were chosen for the proton radiography diagnostic of PETAL (CRACC), as mentioned above. Anyway, it was not chosen for the detection of the particles inside the other diagnostics because RCF are usually used at rather high particle fluxes, which may not be what we will have, especially during the ramp-up of the PETAL energy. Imaging plates were thus preferred to RCF because of their higher sensitivities. Given the solid angles of e.g. SESAME or SEPAGE, this is in retrospect a non-negligible argument.

1.5 Photostimulated luminescence PSL principle in the active layer of an IP

When a high-energy particle goes into the active layer of an IP, it ionizes the material on its track, in particular Eu^{2+} ions going to Eu^{3+} states. The emitted electrons can be trapped in a F(Br) or F(I) sites to form metastable states of $F(Br^-)$ or $F(I^-)$ [34]. The number of collisions of an ionizing particle, especially in the MeV or above kinetic energy range with electrons of the medium being very large, these ionization processes are essentially of statistical nature. The number of metastable states varies then proportionally with the total ionization of the active layer on the particle track. Hence, the number of metastable states keeps the information on the particle deposited energy.

The recombination of the electron-hole pairs corresponding to these metastable states can occur in various ways. It can be spontaneous in particular, because of the thermal motion of electrons. This effect is called fading and has to be measured precisely (see below). The recombination of an electron with an Eu^{3+} ion can be stimulated by photons as it is depicted in Fig. 1.15. This recombination can occur either by transport of electrons in the valence bond, or by quantum tunnelling of an electron from the $F(Br^-)$ or $F(I^-)$ sites that are close to Eu^{3+} ions [34].

The photon spectrum of scanners used to readout the IP signals contains two maxima, for wavelengths of 500 nm (2.5 eV) (eq. 1.6) and 600 nm (2.1 eV) (see Fig. 1.14), corresponding to transitions shown in Fig. 1.15. Photons of these wavelengths can thus be used for the stimulation of the recombination [34]. The lines in Fig.1.15 show the transitions from 1s to 2p states of $F(Br^-)$ or $F(I^-)$ sites.

$$\lambda(\mathrm{nm}) = \frac{1240}{\mathrm{E(eV)}} \tag{1.6}$$

As described below, this stimulated recombination is usually performed in a scanner. The recombination of electrons with Eu^{3+} emits a 3 eV photons. This process is called Photo-Stimulated Luminescence (PSL) [34].

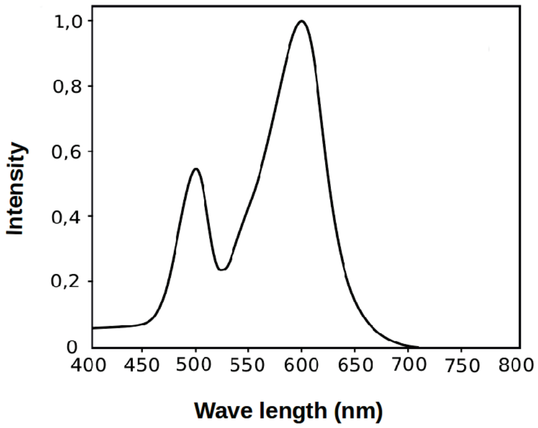

Figure 1.14: The IP scanner photon spectrum [34].

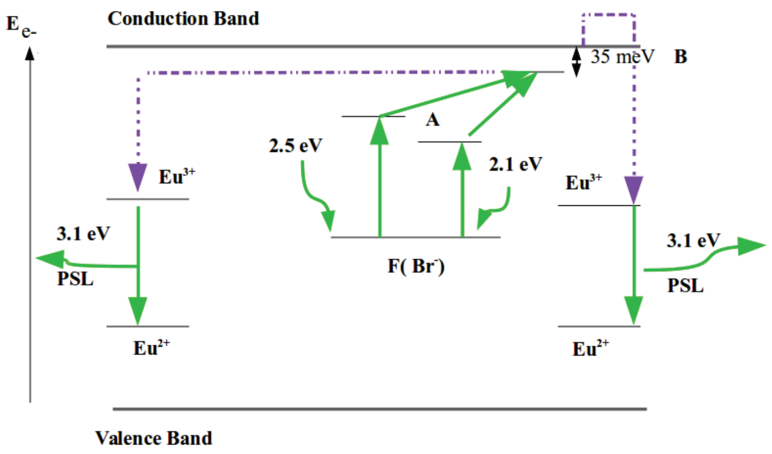

Figure 1.15: Photostimulated luminescence principle (PSL) in the active layer of an IP.

1.5.1 The procedure of read-out the IP

After the irradiation, the IP is placed into a scanner for the read-out. The IP surface is pixelated by the scanner which codes the signal. The scanner provides a source of photons to stimulate the transitions from the $F(Br^-)/F(I^-)$ sites and the emitted photons are detected. The detected signal is proportional to the number of emitted photostimulated luminescence photons. Therefore, it is proportional to the number of particles that went through the pixel. Note that the scanning process can be done several times since its not 100% efficient to trigger PSL photons.

The transition from the $F(Br^-)$ and $F(I^-)$ to the sub-conduction surface states occuring spontaneously is called fading (see paragraph 1.10). Such a phenomenon must be taken into account in the data analysis of experiments. With the fading corrections we can obtain a signal which is proportional to the actual number of $F(Br^-)/F(I^-)$ sites and hence to the number of ionizing particles which have gone through the IP in each pixel area.

It is important that the procedure of irradiation and IP reading is done in the obscurity to avoid any IP signal loss.

The scanner generates a matrix containing a numerical value for each pixel named Quantum Level (Q_L). The response of the scanner is logarithmic, i.e. the dependence of $\mathrm{Q_L}$ on the number of detected luminescence photons is a logarithm. Values in $\mathrm{Q_L}$ are converted into the PSL numbers using the function (1.7) that was calibrated by the manufacturer:

$$\mathrm{PSL} = \left(\frac{\mathrm{Res}}{100}\right)^2 * \frac{4000}{\mathrm{S}} * 10^{\mathrm{L}*\left(\frac{\mathrm{Q_L}}{2^{\mathrm{D}}-1}-\frac{1}{2}\right)} \tag{1.7}$$

- PSL : photoluminescence photon number read in the pixel;
- Res : size of pixels in μm;
- S : sensitivity;
- L : latitude;
- D : read-out dynamic range (8 bits or 16 bits);
- $\mathrm{Q_L}$: numerical value of the pixel (coded between 0 and $2^{\mathrm{D}} - 1$).

All IP readouts in this work were made with a Fuji scanner FLA7000, with a resolution of 50 μm, sensitivity of 4000, the latitude of 5 and the 16-bit dynamic range. In our case, if $\mathrm{Q_L} = 0$ we obtain $\mathrm{PSL} = 10^{-3}$, which means that any PSL number below roughly 10^{-2} is unsignificant.

1.6 GEANT4 simulation

GEANT4 is a code for Monte Carlo simulations particularly suited to the calculation of the particle propagation through matter [35]. For each type of particle, there is a list of processes that might occur in matter (e.g. for photons: photoelectric effect, Compton scattering and electron-positron pair production). To describe the propagation of particles through matter, GEANT4 calculates the step from the cross section of each process selected to compute the probability of interaction with matter according to the medium characteristics (density, composition...).

The interaction of charged particles (electrons, protons and ions) whose kinetic energies are in the detection range of the charged particle PETAL diagnostics [0.1 - 200 MeV] occurs essentially via electromagnetic processes. At the microscopic

level, two particle collisions such as:
- electron-electron scattering
- electron-atomic nucleus scattering
- ion (proton) - electron scattering
- ion (proton)- atomic nucleus scattering

The theory of this particle-matter interaction has been described in many articles and text books, for example [36] [39]. Rewriting the whole theory is beyond the scope of this work. Anyway, we just want to underline here the basic quantitative difference between electron-matter and proton/ion-matter interaction in this energy range. This difference finds its ground essentially in two facts:
- The possibility for MeV electrons, which are relativistic, to produce secondary photons from Bremsstrahlung in the electrostatic field created by the atomic nucleus charge in its vicinity;
- The kinematics of the two body collision, described in Appendix C for Rutherford scattering.

The photon produced by Bremsstrahlung have a non−negligible probability to take a large part of the incoming electron energy. This means that those secondary photons will be also ionizing and will subsequently scatter on electrons of the medium to which they can transfer also an important kinetic energy, hence becoming also ionizing electrons.

The probability of few MeV protons to produce Bremsstrahlung photons is, by contrast essentially 0.

The kinematics of the two−particle collisions, mediated by the electromagnetic interactions , puts also in evidence a big difference between the interactions of electrons/ions with matter. There, the argument has to do with the mass difference between electrons and protons/ions. As a reminder, the ratios of the masses between protons and electrons is approximately

$$\mathrm{m_p/m_e} \sim \ 1800$$

Such a mass difference induces that, if the angular scattering of identical particles is taken as a reference,
- electron-atomic nucleus collisions in average to much larger angles
- proton/ion -electron collisions lead basically to very small scattering angles.

When one adds to this the screening of the atomic nucleus electric field by the atomic electrons, meaning that the collisions with electrons are much more probable than the collisions with the atomic nuclei, we qualitatively understand a big difference between electron−matter and proton/ion −matter interactions.

In GEANT4, the positions and the momenta of the particles are modified after each step of the simulation. The positions and the momenta of possibly produced secondary particles are saved and wait to be treated. After each step, if the particle energy is smaller than a threshold which can be determined by the user, the particle tracking is stopped. Until this occurs, or the particle escapes the user-defined volume describing the system to be simulated, the particle continues its path through matter in the simulation. We consider the event ends when the primary particle and all its secondary particles were tracked. For our needs, in order to compute the energy left inside the active layers of the IPs, the energy left by the primary particle is added to the energy losses of all produced secondary particles. A new particle is then shot and the algorithm continues to shoot the particles until the total number of particles N is shot. Note that N is defined by the user.

For the description of IPs in our simulation, the IP layers data given in Tab. 1.2 were used. For each interaction, we can determine the name of the physical process, the type of the secondary particles possibly generated, the position of the interaction in the space and in the matter and the quantity of energy deposited in the matter. Notice that we have introduced the possibility not to track the secondary particles in order to determine the contribution of primary and secondary particles to the energy losses in the IP active layer.

As explained in section 1.8 below, the main goal of our GEANT4 simulation is to compute precisely the average energy loss of a particle, for which we know experimentally:
- The type (either electron or proton);
- The kinetic energy;
- The incident angle with respect to the normal of the IP plane;

The problem is rather well defined. A calculation is, in our case, mandatory because the average energy loss inside the active layer of an IP is not an experimental observable. In fact, what could be measurable would be the average energy loss of a particle in traversing an Imaging Plate, i.e. going through the three or four layers. Such an energy loss may not be dominated by the average energy loss inside the active layer of the IP.

Moreover, three additional reasons lead us to choose GEANT4. The first one is linked to the dimensions of our detectors, made of layers from a few 10 μm thick to cm thick for our needs, we have hence to ensure the tracking of the particles precisely on this energy range of dimensions at least, which GEANT4 can do. The second reason of our choice is that the active layers of imaging plates are composite materials, for which effective energy losses have to be computed accurately. This feature is also available in GEANT4. The third reason of our choice has to do with the fact that we need to use well tested models for electrons and protons in a range corresponding to the PETAL accelerated particle kinetic energy range (below 150 MeV) and particle types: protons, ions and electrons. This also is available in GEANT4.

As mentioned above, in the energy range of this study, the interaction of charged particles with detectors is essentially driven by electromagnetic processes. For few-tens of MeV protons, some inelastic nuclear scattering come into play with, anyway, very low probabilities in our thin detectors. They have been neglected in our calculations. This also allows the simulation to run faster. In our GEANT4 simulations, these electromagnetic processes are, for charged particles:
* Multiple scattering
* Bremsstrahlung
* Ionisation

For positrons, we have included annihilation as a possible mechanism of their interaction with detectors.

For photons, which are secondary particles in our study, we have implemented in our calculation:
* Photoelectric effect
* Compton scattering
* $e^- - e^+$ pair production

We have not done any systematic study of the relative importance of each individual process in the particle interactions with increasing plates. It was beyond the scope of the present thesis.

As detailed below, there exists in GEANT4 different libraries describing these electromagnetic processes. Their existences within the toolkit are explained either historically or by the goals they are aiming at: particle energy range of application, types of electrons etc...

The choice of the number of particles sent into the matter is a general problem related to the use of Monte Carlo methods. This number should be sufficiently high to obtain statistically reliable results. In Fig. 1.16 a test of convergence is shown to calculate the energy deposited by 3 MeV protons in the sensitive layer of an MS IP. It presents the mean deposited energy per proton in the sensitive layer calculated from all protons sent in the simulation. For each simulation we initialize differently the seed of the random generator in order to have statistically independent event populations. We can see from the figure, that when the proton number is small (N=1 ... N=10), the mean deposited energy varies significantly from one simulation to another, because the statistical sample is too small. When the number of computed protons is large enough, the value of the mean deposited energy converges. The specified number of simulated particles should be a compromise between a large number, causing possibly unnecessarily long calculation times, and a small number of particles that don't produce statistically meaningful results. For this reason, the optimum value of 10^4 particles has been chosen for the calculation of the average energy loss in the IP active layer. It should be underlined that in case more detailed information is needed on the computed particles, a higher statistics will be required.

1.7 GEANT4 libraries

GEANT4 tracks particles and provides information about the particle step and the energy deposited in the matter at each step. There are many classes in GEANT4 simulations, which define the geometry of the detector, the atomic compositions of materials, and the physical processes. The physical processes of the interaction of particles with matter are described by different libraries. The electromagnetic process GEANT4 library is composed of:

- PENELOPE model (PENetration and Energy LOss of Positrons and Elec-

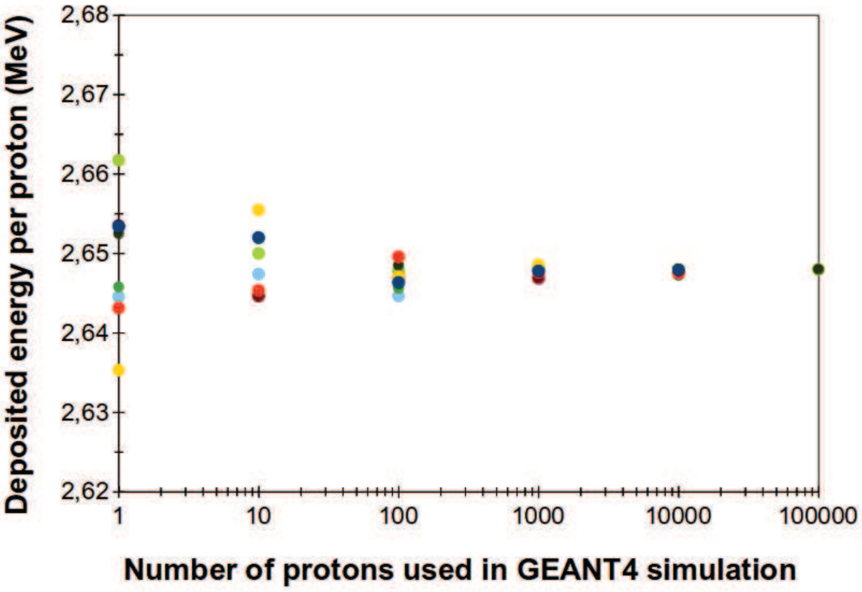

Figure 1.16: Test of convergence of the deposited energy in the active layer of MS IP using 3 MeV protons.

trons), which describes the low-energy physics, and treats the EM interactions of electrons and photons in the energy range between 250 eV and 1 GeV;

- EM OPT3, designed for applications that require higher accuracy of tracking particles, which interact electromagnetically, without magnetic fields;
- EM OPT1, designed for the analysis of the Compact Muon Solenoid (CMS), TeV ranges and specific detector materials and the predicted energy loss of the EM OPT1 could differ up to a factor 2 with respect to other models;
- Livermore library, based on the evaluated photon, electron and atomic libraries.
- EM-STD, multipurpose libraries.

Fig. 1.17 shows the deposited energy in the active layer of MS IP using electrons between 0.1 and 10 MeV, obtained using various libraries: 1) PENELOPE, 2) LIV-

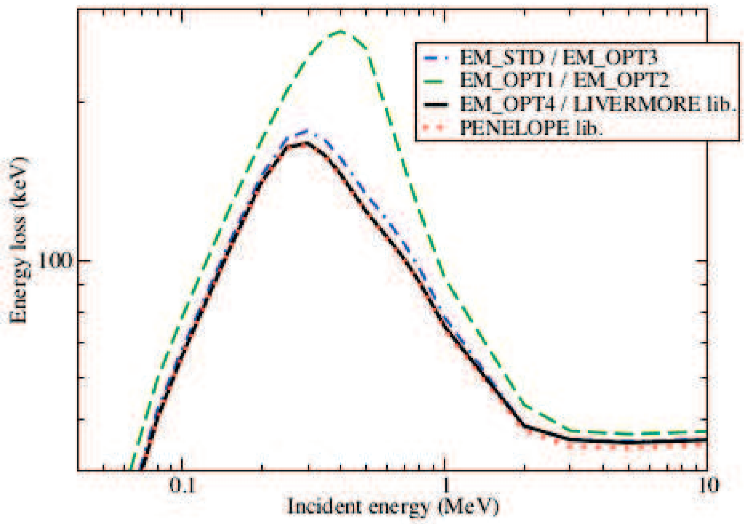

Figure 1.17: The deposited energy of electrons inside the active layer of an IP MS computed with various libraries.

ERMORE, 3) EM_OPT1, 4) EM_OPT2 5), EM_OPT3, 6) EM_OPT4, and 7) EM_STD. The EM-OPT4, PENELOPE and LIVERMORE libraries give similar results. There are a few percent differences between the results from EM-OPT3 and EM-STD but the time of calculation is faster than with the other libraries. EM-OPT1 and EM-OPT2 give similar results. In this work, the EM-OPT3 and EM-STD libraries are used. The reason to use EM-OPT3 is to compare our results with older data sets that were obtained using this library. The reason to choose EM-STD is to decrease the calculation time without affecting the precision of the results for high-energy particles when compared to those obtained with EM-OPT3. It should be underlined that the same comparison, with analog results for protons. There exists an extensive literature on the simulation of particle interactions with matter computed with GEANT4, and for part of it compared with experimental data. This literature was produced either in the framework of detection studies, e.g. for nuclear physics or particle physics experiments, understanding the interaction of cosmic rays with satellites, or to predict doses in cancer oncology with particle beams. In the energy range of our studies the different electromagnetic libraries of GEANT4, when compared to data, either for electrons or protons (see e.g. [40, 41]), show that a better agreement is obtained with EM-STD or EM-OPT4.

1.8 Link between the PSL and the deposited energy in the IP active layer

As mentioned above, the number of metastable sites created inside the active layer of an IP is related to the ionization of the active layer on the particle track. This ionization is quantified by the energy loss inside the active layer. Moreover, the number of PSL detected in the scanner (called IP response in the following) is directly proportional to the number of these metastable states. It is not a strict equality for two reasons. The first is that the excitation of the transitions from the $F(Br^-)$ or $F(I^-)$ 1s states to 2p states is not 100% efficient, i.e. not all the sites of a given pixel are excited. The second has to do with the solid angle covered by the read-out phototube which equips the scanner, which is only one part of 4π, whereas the photon emission at 3.1 eV from the recombination of the $Eu^{3+} + e^- -> Eu^{2+}$ is isotropic.

Therefore, the number of the detected PSL is directly connected to the energy loss inside an IP. It is a purpose of a calibration to quantify this relationship. We should keep in mind here that such a relationship a-priori depends on the IP and on the scanner. Therefore, an additional work is needed to adapt this relationship to other scanners as in [38].

1.9 Modelling of the response of the imaging plates in the sensitive layer of the IP

For our work, two models to describe the relationship between the IP response and the average energy loss (Edep) of the particles inside the IP active layer were used. The first model is of Hidding et al. [25] and considers a linear relationship between the average deposited energy and the IP response per particle:

$$\mathrm{R(E)} = \alpha.\mathrm{Edep(E)} \tag{1.8}$$

where E is the energy of the incident particle, R(E) in PSL is the response of the IP. The coefficient α in PSL/keV represents the sensitivity of the screen, which means its capacity to produce luminescence photons per unity of deposited energy. We mention that α varies from an IP type to another for a given scanner. Edep(E) in keV is the deposited energy in the active layer. This energy is the total energy deposited by the incident particle and its possible secondary particles. In our experiments, the response R(E) is measured for the case of a source of monoenergetic particles depositing their energy, the characteristics of which are known. The deposited energy Edep is calculated using the GEANT4 simulation. The sensitivity α is computed as the ratio between the average deposited energy, obtained from the GEANT4 simulation, and the measured response R(E). Figs. (1.18) and (1.19) present the calculation of the mean deposited energy in the active layer of an MS IP as a function of the incident energy for electrons and protons using the EM-STD libraries. For each simulation 10^4 identical particles were used. The dependences seen in these two figures are different, corresponding to the two types of particles and the differences of their interaction with matter. Protons interact primarily by ionisation of the matter that they pass through. The curve of the deposited energy obeys the Bethe law (the stopping power is greater for lower energy particles). All protons with energy lower than 600 keV stop in the protection layer, and don't reach the sensitive layer. Protons with energy between 600 keV and 3.5 MeV have enough energy to reach the sensitive layer and deposit all their remaining energy and stop in this layer. When the proton incident energy exceeds 3.5 MeV, the particle deposits a fraction of its energy in the active layer and continues its trajectory. For electrons, the shape of the curve has similarities and slight differences with that of protons, with the maximum energy of 300 keV for electrons that deposit all their energy in the phosphoric layer, with anyhow a narrower maximum.

The second model of Bonnet et al. [29] [42] takes into account the depth of the PSL photon emission in the active layer of an IP:

$$\mathrm{R(E)} = \alpha \int_0^{\epsilon} \frac{\mathrm{dE}}{\mathrm{dz}}.\exp(-\frac{\mathrm{z}}{\mathrm{L}})\,\mathrm{dz} \tag{1.9}$$

where ϵ is the thickness, z is the depth in the active layer, dE/dz is the energy loss power and L a parameter of the model which can be interpreted as the absorption length of the photons (the photons emitted by the scanner losses as well as those from the Eu ion recombination). BaFBr/I:Eu^{2+} being in simulations [43], such an absorption corresponds only to transition between bound electron states of the crystalline structure to the conduction band with binding energies below 2 eV/3 eV.

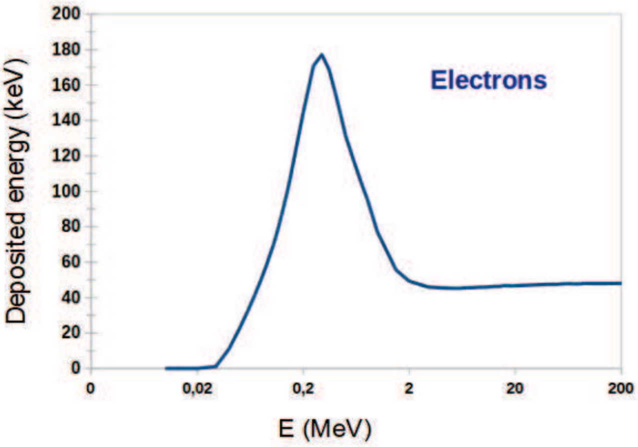

Figure 1.18: The calculation of the mean deposited energy in the active layer of an IP MS as a function of the incident energy for electrons.

The model of Bonnet et al. is based on the fact that the photons of the scanner and the photostimulated luminiscence can be absorbed inside the protective or phosphoric layer before any detection of the luminiscence photons. Therefore, some signal created by particle depositing its energy deep inside IP might never reach the photo-multiplier of the scanner and this signal would be lost. As the energy of particles increases, they interact deeper in the sensitive layer of IP and deposit their energy, which has then a lower chance to be read-out. The Bonnet et al. model introduces a correction for this effect and, as a consequence, a dependence of the IP response on the energy loss profile within the active layer of the IP. As explained in Appendix B these two models are equivalent for high-energy particles for which the energy loss profile is constant in the active layer, ”high−energy“ meaning here that ΔE, the energy loss in the active layer is much smaller than the particle kinetic energy.

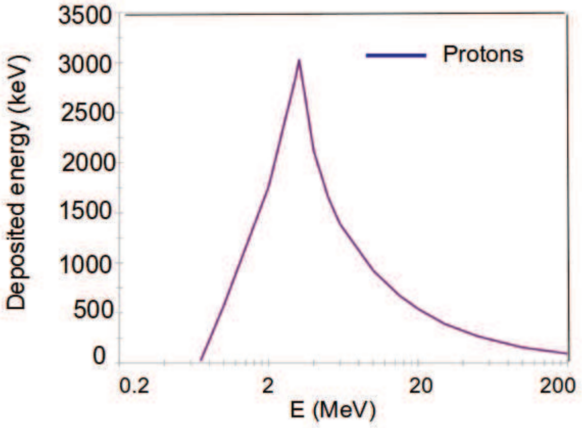

Figure 1.19: The calculation of the mean deposited energy in the active layer of an IP MS as a function of the incident energy for protons.

In the present study, we didn't perform measurements at low particle kinetic energies with as small bins as what was done by T. Bonnet et al. Therefore, contrary to their work, we were not able to fit our data with a free value of L for each type of IP and we used the values of [28] and [42], i.e.:

For electrons:

- L(MS) = 222 μm
- L(SR) = 44 μm
- L(TR) = 118 μm

For protons

- L(MS) = 213 μm
- L(SR) = 116 μm
- L(TR) = 43.8 μm

Figs. 1.20, 1.21, 1.22 and 1.23 present the curves of the deposited energy as a function of the depth in the MS IP. The simulations were performed for charged particles, electrons (0.5, 1, 5, 10 and 18 MeV), and protons (1, 3, 10, 18 and 50 MeV) using 10^4 incident particles.

It can be seen that the deposited energy profile is constant for electrons above 2 MeV. For protons, the deposited energy decreases when we increase the incident energy. More explanations will be given in next chapters.

As examples, the energy loss profiles of 0.5 and 1 MeV electrons in the active layer of an MS IP are given in Fig. 1.20. Those for electrons of energies corresponding to our experiment at ELSA (5, 10 and 18 MeV) are given in Fig. 1.21. We see a qualitative difference between the first two curves (see Fig. 1.20) and the three curves of our experiment at ELSA (see Fig. 1.21), which are essentially flat except for the last micrometers, where a sharp increase is to be noted. Such an increase is due to low-energy electrons emitted from the electron multiple scattering in the support layer.

In Fig. 1.22, the energy loss profiles of 1 and 3 MeV protons in an MS active layer are shown. These protons stop inside the active layer of the IP. We see from Fig. 1.23 that the energy loss profiles are clearly flattening when the proton kinetic energy increases.

1.10 Fading measurements

As mentioned above, spontaneous electronic transitions occurs between $F(Br^-)$ and $F(I^-)$ sites and sub-conduction band states, reducing therefore the number of occupied $F(Br^-)$ and $F(I^-)$ at a rate constant with time. Such a phenomena is called fading in the following. In case of LMJ, it is anticipated that the time between the laser shot and the scanner reading of IP may be up to five hours because of the transport of detectors from the system to the read-out scanner and of the radioprotection procedures. On the other hand, this time was fairly low (usually few minutes) during our calibration experiments at smaller-scale facilities. It is therefore necessary to determine the effect of fading for this time range in order to correct the signal amplitude in our measurements and have meaningful results for PETAL/LMJ experiments.

Measurements of the fading effect were performed with a radioactive source (^{55}Fe) of activity which can be considered as constant over the whole duration of our measurements and the duration of our experiment, to determine the time dependence of the signal, and thus to obtain the fading functions.

Note that the fading measurements of T. Bonnet [29] were performed with three sources ^{90}Sr/^{90}Y, ^{55}Fe and ^{60}Co, i.e. with some ionizing particles more penetrating

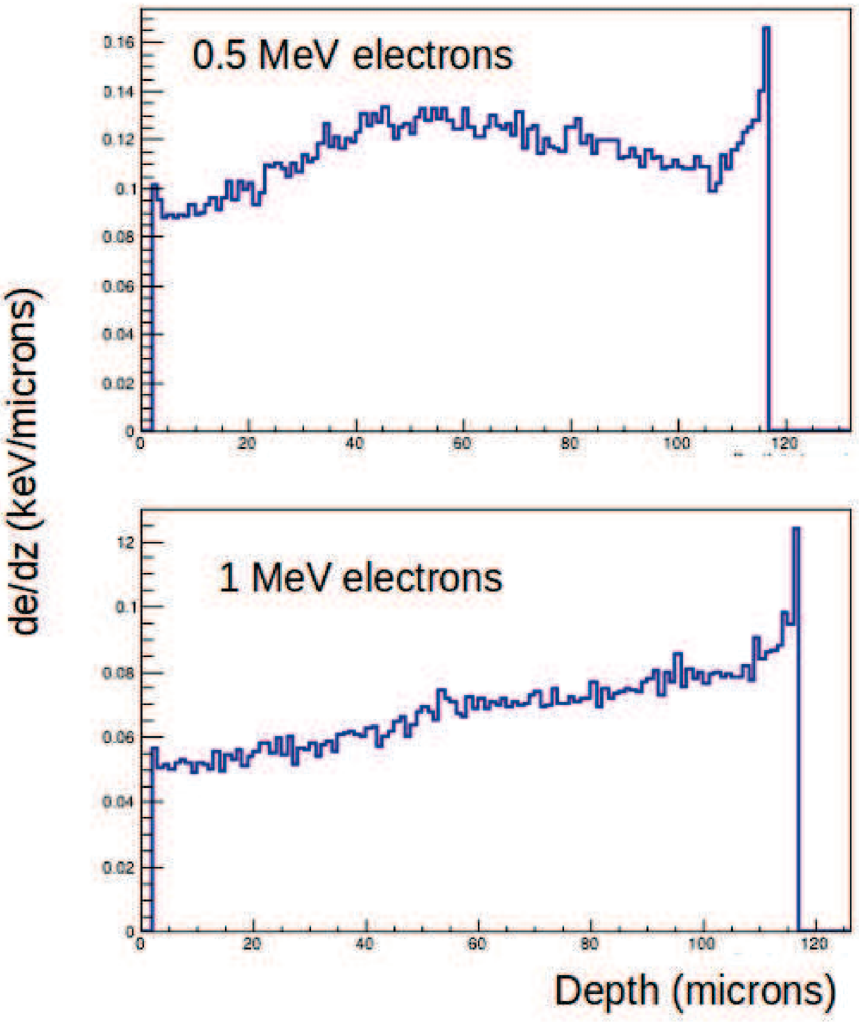

Figure 1.20: Energy loss profiles in the active layer of an IP MS as a function of the incident energy for electrons 0.5 MeV (on top) and 1 MeV (on bottom).

than the low-energy photons of ^{55}Fe (∼ 5 keV). Anyway, the error they estimate on the fading functions they obtain with the different ionizing particles is of the order of 10% [29].

^{55}Fe decays into ^{55}Mn with a half-life of 2.737 years. This half-life is indeed long with respect to a measurement with a source of a few seconds, via electron capture emitting X-ray photons with energy of 5.9 and 6.5 keV. The activity of the source was 808 kBq. During the measurements, the IPs were exposed to this source for a fixed time of 90 s to provide a signal uniform in time without saturation of the signal read-out. The uncertainty in the exposure time was within a few percents (2 seconds). The signal on IP was read out in the scanner after various measured times to estimate the fading functions. The fading functions of the signal with respect to time passed since the irradiation (see Fig. 1.24) were fitted with double exponential curves [44]:

$$\mathrm{f(t) = A_1.e^{(-t/B1)} + A_2.e^{(-t/B2)}} \tag{1.10}$$

The choice of the function (1.10) follows the ideas developed in Tanaka et al. [27], Bonnet et al. [28], and Ohuchi et al. [44] [45]:

1) The decrease dN/dt is proportional to the number of decaying sites N

2) There exists different channels of decay, of different probabilities at least two in the level scheme principle of Fig. 1.15: one via Tunnel effect from the sub-conduction band states to $\mathrm{Eu^{3+}}$ sites and one through electron transport in the conduction band before recombination on a $\mathrm{Eu^{3+}}$ site.

In equation (1.10), f(t) is the probability that an electron-hole pair exists at a given time t after its creation. ($\mathrm{A_i}$) can be interpreted as the branching ratio of channel i. ($\mathrm{B_i}$) characterize the slopes of the exponentials (average decay times). The higher these numbers are the slower the curves decrease. Note that the coefficients $\mathrm{A_i}$ and $\mathrm{B_i}$ do not depend on the duration of irradiation.

The function f(t) being a probability, the sum of $\mathrm{A_i}$ is normalized to unity: $\sum_\mathrm{i} \mathrm{A_i}$=1. Both $\mathrm{A_i}$ and $\mathrm{B_i}$ are intrinsic to each type of IP and should not depend on the ionizing particles.

The coefficients of this fit are summarized in Tab. 1.3. The values were obtained using Matlab fitting tools. Additionally, Kaleidagraph was used on the experimental data and the values mentioned in Tab. 1.3 were extracted in order to compare them with those from Matlab. The results obtained by Matlab and Kaleidagraph are the same. The obtained curves are normalized to the extrapolated signal amplitude at t = 0 (see Fig. 1.25). The uncertainty on the fading

	A_1	B_1	A_2	B_2
MS	0.33±0.01	107.32±9.7	0.67 ±0.01	33974±11235
SR	0.58±0.021	15.05±1.58	0.42±0.01	3829.5±650.9
TR	0.53±0.02	23.81±2.20	0.46±0.01	3837.2±498.1
MP	0.56±0.021	18.46±2.09	0.43±0.01	6117.5±1358.9
ND	0.56±0.017	18.18±1.59	0.44±0.01	3907.0±530.2

Table 1.3: A_i and B_i values given in minutes for five types of IP.

function measurements is about 2% because the IP is exposed for 90 s. As underlined in [46], the comparison between our fading functions and those determined by [29] is almost of 8%, i.e. within the uncertainties estimated by [29] from the use of different ionizing particles. Therefore, we took as a total uncertainty on these fading functions this value of 10%.

It was related by Ohuchi et al. [44] that the fading effect is similar for irradiation by electrons and photons, and independent of the incident particle energy. Nevertheless the signal fading was found to be faster for ion irradiation in the same reference. This difference was related to the higher stopping power of ions, which causes them to deposit all their energy near the surface of the sensitive layer and hence creating electron-hole pairs more densely in the region than deeper into the sensitive layer. We estimated the absorption length of 5 keV photons in the IP to be in the order of 7 μm to be compared with the roughly 50 μm range of the ^{244}Cm-emitted α particles of Ohuchi et al. [44]. The photons in our measurement are thus absorbed in the first micrometers of the IPs. Following the argument of Ohuchi et al., our fading functions should be on the faster side of fading. Since for PETAL+ we will detect essentially high-energy particles which will go through IPs, an additional measurement of these fading functions with a high-energy particle source may be useful.

Fig. 1.25 shows the differences between our results and the results of Bonnet et al. [29]. They used 1.5 MeV protons and the same IP scanner. The signal fading differs from our values up to 8 % for protons. In agreement with other works on this topic, it is estimated that the uncertainty when applying the fading functions to electron and ion signals is within 10 %. This systematic error must be taken into account.

The measurements of fading functions can be altered by the type of IP scanner used. It was described in Ohuchi et al. [45] that differences up to 50 % can occur between fading functions measured by BAS-1000 and BAS-5000 scanners. As can be noticed from Fig. 1.25, the data of Tanaka et al. [27] for SR IP differ from our data and measurements done in Bonnet et al. [29]. The authors explained the differences by the usage of a different read-out system (BAS-1800). To compare sets of data we chose the same conditions (same temperature, scanner), or we have to perform relative calibrations between two scanning procedures with same source of ionizing particles.

One also has to remember that the signal fading depends on the temperature, as it was explained in Ohuchi et al. [44] and the fading is faster at higher temperatures. The reason is that some charges stay trapped at localized defects but some recombine with holes after irradiation for a time, depending on the temperature and the activation energy of the traps. The measurements should therefore be performed at controlled ambient temperature (in our case it was $22°C$), variations of a few degrees can be considered as negligible. When working at very different temperatures, the signal fading functions are different from what is described in this work and new measurements may also be necessary.

Even though the p−value of the χ^2 per degree freedom of the double exponential fit is below 1%, (χ^2/N $\sim$ 0.65 for N=24) it seems that the double exponential function does not fit as well the fading time range between 20 and 90 minutes with an apparent underestimate of our data points for the five types of IPs. We obtain with this three−exponential for a χ^2/N $\sim$0.33 with an even smaller p−value. For that reason, we made an attempt to fit the experimental data with three exponentials:

$$\mathrm{f(t) = A_1.e^{(-t/B1)} + A_2.e^{(-t/B2)} + A_3.e^{(-t/B3)}} \tag{1.11}$$

Fig. 1.26 and Tab. 1.4 show the curves and the coefficients of the three exponential fit. The coefficients in Tab. 1.4 and the error bars are higher than the values of Tab. 1.3.

As seen in Fig. 1.26, for the time longer than 20 min from irradiation, a three exponential function seems to fit the experiment data on signal fading in a better

	A_1	A_2	A_3	B_1	B_2	B_3
MS	0.20±0.46	0.17±0.37	0.62±0.16	60.92±22.6	331.14±230.5	$110360\pm1.98.10^5$
SR	0.29±0.46	0.37±0.08	0.33±0.44	44.44±10.81	5081.36±732.4	5.76±1.36
TR	0.20±0.44	0.22±0.42	0.58±0.14	12.91±1.75	107.99±30.46	5278.53± 615.9
MP	0.36±0.49	0.06±0.50	0.576±0	$72.16\pm8.838.10^6$	$72.69\pm3.59.10^7$	6689.9±9523
ND	0.29±0.49	0.06±0.49	0.637 ± 2.10^{-5}	$83.96\pm 9.63.10^4$	$77.09\pm4.23.10^5$	5175±7625

Table 1.4: A_i and B_i values given in minutes for five types of IP.

way when compared to a two exponential function fit.

1.11 The use of stacks in SEPAGE and SESAME

High-energy photons are produced from the interaction of PETAL with its target. These photons come either directly from the target plasma or indirectly from the decay of materials of the LMJ sphere activated by plasma produced photons or neutrons. The IPs are sensitive to ionizing particles in a large energy range. IPs should be shielded against high-energy photons above a few tens of keV (below this value they are sufficiently shielded by the mechanical structure of the diagnostics). The most efficient way to protect the signal in the IPs is to use high-Z material such as tungsten. Therefore, in our work we studied the response of IP with high Z-materials close to them. Such composite detectors are called stacks in the following. Moreover, the presence of material close to IPs may change the IP responses. Ensuring the independence of the IP signal in their close environment inside the PETAL+ diagnostics is another reason to study the IP response within stacks.

Therefore, in this thesis, we have also performed measurements with IPs with plates of tungsten and lead in order to measure the influence of this high Z-material on the IP response. This is one of the goals of the present work, to give the results and their comparison with the GEANT4 simulation. This type of measurement does not exist in the literature and will allow us to determine the spectra of particles emitted by the interaction of the PETAL laser with its target.

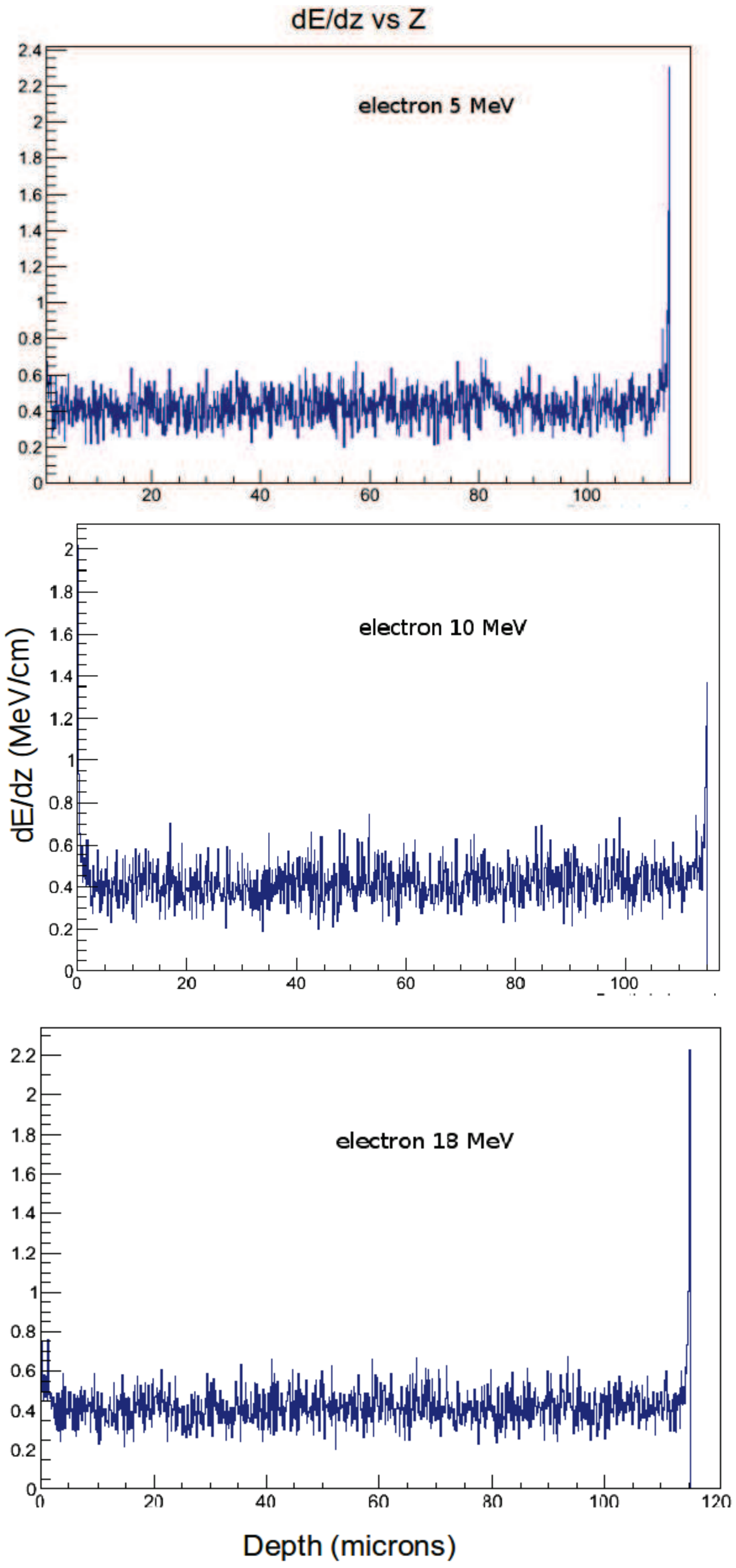

Figure 1.21: Energy loss profiles as a function of the depth in the active layer of an MS IP for electrons, for each kinetic energy value, calculated using 10^4 incident particles.

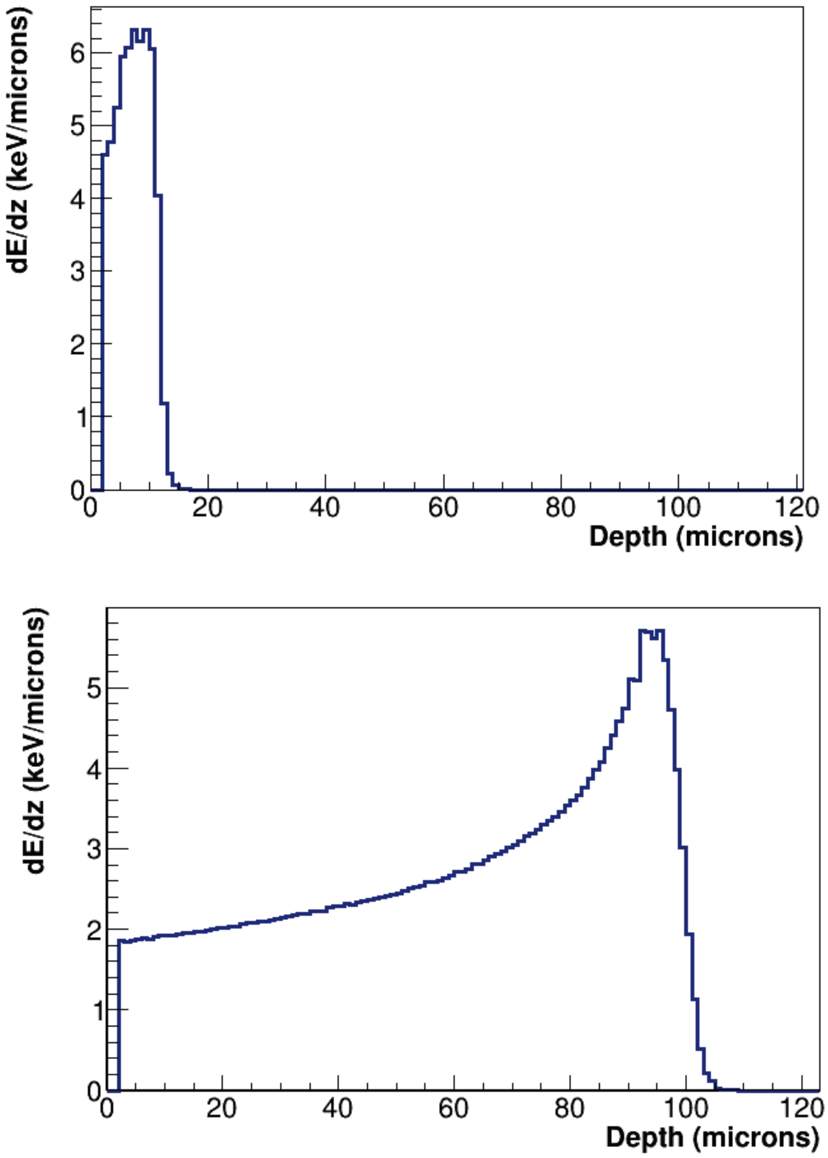

Figure 1.22: Energy loss profiles in the active layer of an IP MS as a function of the incident energy for protons 1 MeV (top) and 3 MeV (bottom).

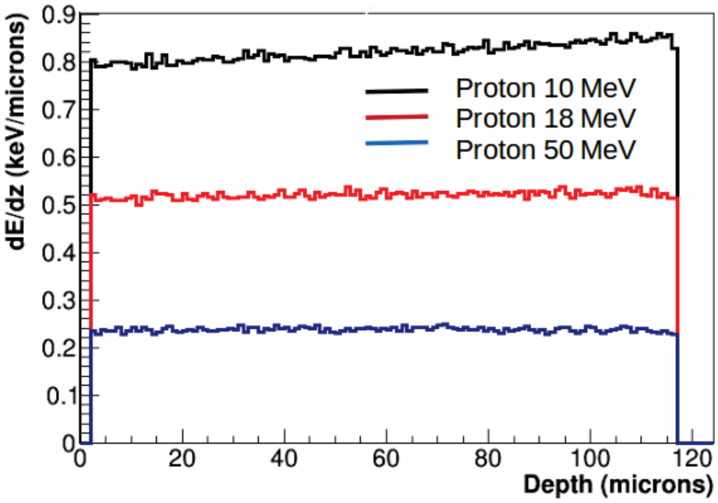

Figure 1.23: Energy loss profiles in the active layer of an MS IP for protons. The mean deposited energy is calculated using 10^4 incident particles for each kinetic energy value.

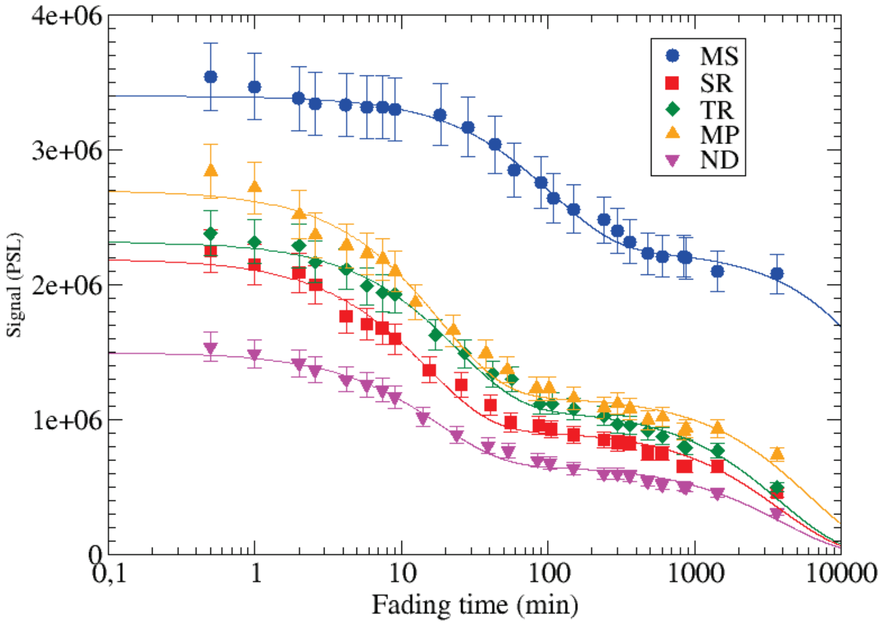

Figure 1.24: The signal of the five type of IPs as function of time (minutes) [46].

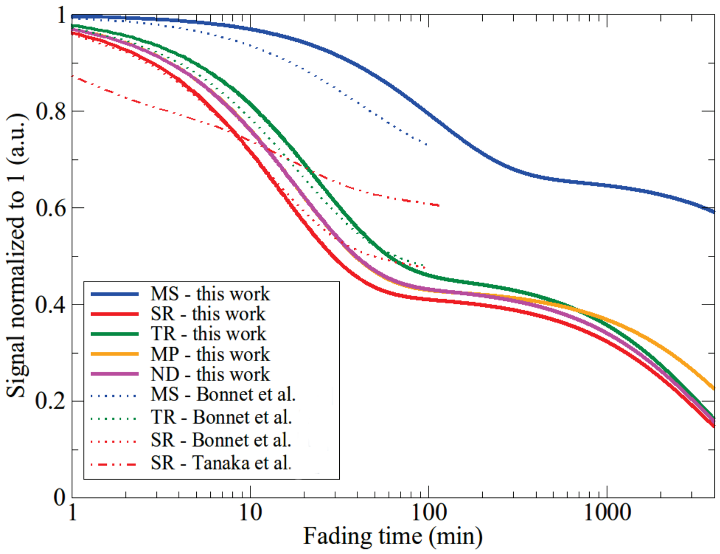

Figure 1.25: The normalized signal as a function of fading time for five types of IPs and comparison with the literature [46].

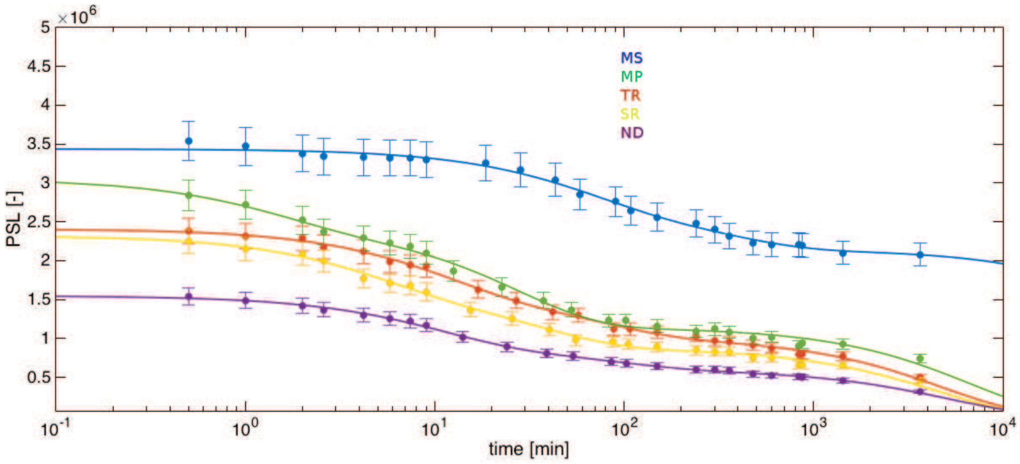

Figure 1.26: The signal in function of fading time for five types of IPs using three exponential curve.

Chapter 2

Response functions of Imaging Plates to 0.1-1000 MeV electrons

This chapter is focused on the response functions of Imaging Plates (IPs) for electrons in the energy range between 0.1 and 1000 MeV. Two experiments for the calibration of single IPs or more complicated systems were performed at ELSA, Bruyères-Le-Chatel, France, where the used electrons energies are 5, 10 and 18 MeV, and at the Laboratoire d'Optique Appliquée (LOA), Palaiseau, France, with laser-plasma accelerated electrons from 40 to 180 MeV are described. Using simulations, the responses of the IPs in the energy range [0.1 - 1000] MeV are computed. The origin of the signal in the IPs is discussed.

2.1 The response functions for IPs to 5, 10 and 18 MeV electrons at the ELSA facility

2.1.1 The experimental setup

The first of our calibration experiments was performed at the laser electron accelerator ELSA, which is installed at CEA DIF, Bruyères-le-Châtel, France. The ELSA accelerator consists of a 144 MHz photoinjector utilizing a Nd:YAG laser system which provides pulses with an energy of 1 J and a duration of 30 ps (FWHM) at the central wavelength of 532 nm (see Fig. 2.1). The pulses of the driving laser are interacting with a K_2CsSb photocathode with a diameter of 6 mm. Acceleration cavities producing electron bunches with the energy of 2 MeV within the injector, maximum charge of 15 nC (measured at four separate locations along the beam propagation) and a spacing between bunches of 69 ns (repetition rate of 14.4 MHz). It is possible to generate longer macro-bunches with a maximum duration of 150 μs by merging up to 2000 consecutive micro-bunches. These long macro-bunches can be produced with the repetition rate of 10 Hz. The electrons are then accelerated by three 433 MHz RF cavities (RF1, 2 and 3 in Fig. 2.1) of the linear accelerator stage to an energy between 5 and 18 MeV with the exit electron bunch diameter of 1 mm [58].

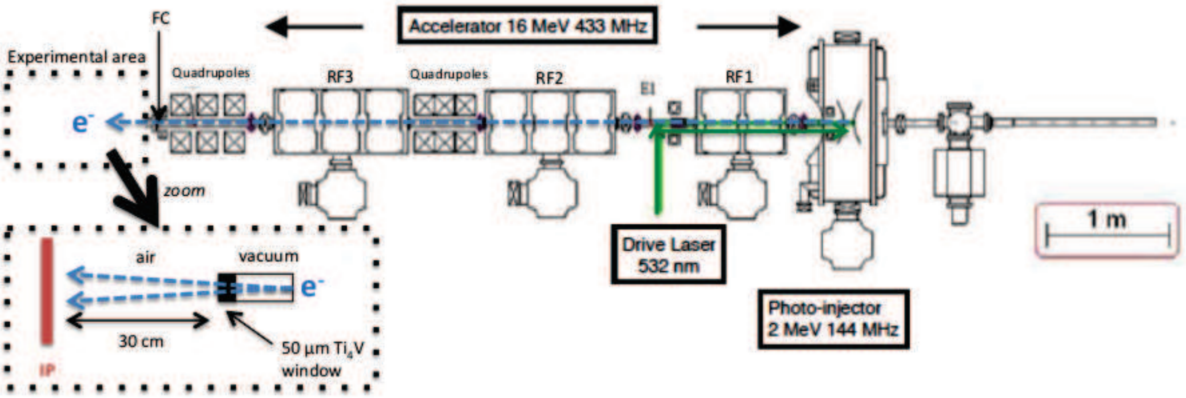

Figure 2.1: ELSA facility. The lower part shows the experimental setup for our experiment.

Our IP detectors were at the distance of 30 cm from the end of the linear accelerator. The tube of the linear accelerator ends with a 50 μm thick Ti_4V window. Due to a large divergence of the electron beam after the exit window, the signal on the IP was spread into a circle with a radius of 1.3 cm (see Fig. 2.2). The size was calculated from the Gaussian function fit as 3σ width. The stopping power for 5 MeV electrons through the Ti_4V window is 7.2 MeV/cm. Tab. 2.1 shows the deposited energy for electrons 5, 10 and 18 MeV through Ti_4V window. The energy loss on the Ti_4V window can be neglected. All electrons measured by the Faraday cup located downstream of the last set of quadrupoles irradiated our detector, which was roughly 5 cm wide in both transverse directions.

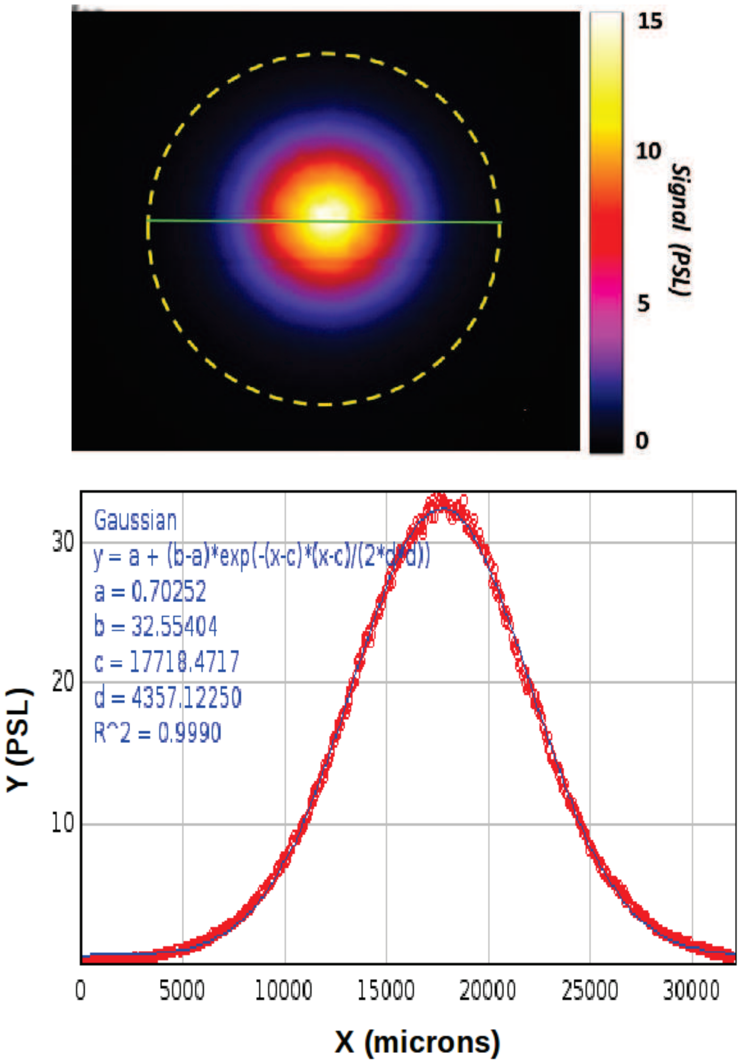

Figure 2.2: The signal detected on an IP

The charge of the electron bunch should not exceed 10 pC in order to avoid saturation of the scanner read-out of the IP signal. Due to the amplified-spontaneous emission of the driving laser and resulting continuous electron noise, the electron bunch charge measurements were inaccurate for such charges of the electron bunches. For this reason we were not able to run in single micro-bunch mode but rather in multiple-bunch mode. As was demonstrated by J.-P Nègre and Zeil et al. [26, 66], MS and SR IP responses are linear up to 60 pC for electron bunches

	5 MeV	10 MeV	18 MeV
Deposited energy MeV	0.036	0.043	0.054

Table 2.1: The deposited energy of electrons through the Ti_4V window at the end of the beam pipe.

with a few picosecond durations and overall densities up to 10^{12} cm^{-2}. Moreover, a Wratten filter with the calibrated transmission of 1/434 was installed in front of the scanner phototube to prevent the saturation of the read-out signal. The transmission factor of the Wratten filter was measured in a dedicated experiment of J.-P Nègre and Tanimoto et al. [26, 67] and checked during one of our experiments performed later (see Chap.3).

The uncertainties of the measurement are:

- 2 % from the filter transmission;
- less than 5% related to the charge measurement.

The X-rays (Bremsstrahlung) produced from the interaction of electrons with the Ti_4V window must, in principle, contribute to the signal detected on our IPs. In order to determine the contribution of this effect, a measurement using a magnetic dipole placed at the exit of the beam pipe and in front of our IP was performed. All electrons were bent by the magnetic field and this allowed the identification of the X-ray contribution on the IP by separating the two (see Fig. 2.3). The integration of this identified signal provides a contribution from the Bremsstrahlung photons produced by the electrons in the beam pipe exit window of less than 1% of the total signal on the IP. It is therefore neglected. The magnetic dipole was thus not used during shots dedicated to the IP calibration. The noise caused by the natural radioactive background and cosmic rays was measured and could be neglected due to a low value of about 0.35 PSL/mm^2 (i.e. 10^{-3} PSL/px).

2.1.2 The response calibration of single IPs

The first step of the experiment is the calibration of single IPs. The response of IPs is the average number of PSL per incident particle corrected for the fading effect (see the introduction). The PSL signal is selected from the area defined

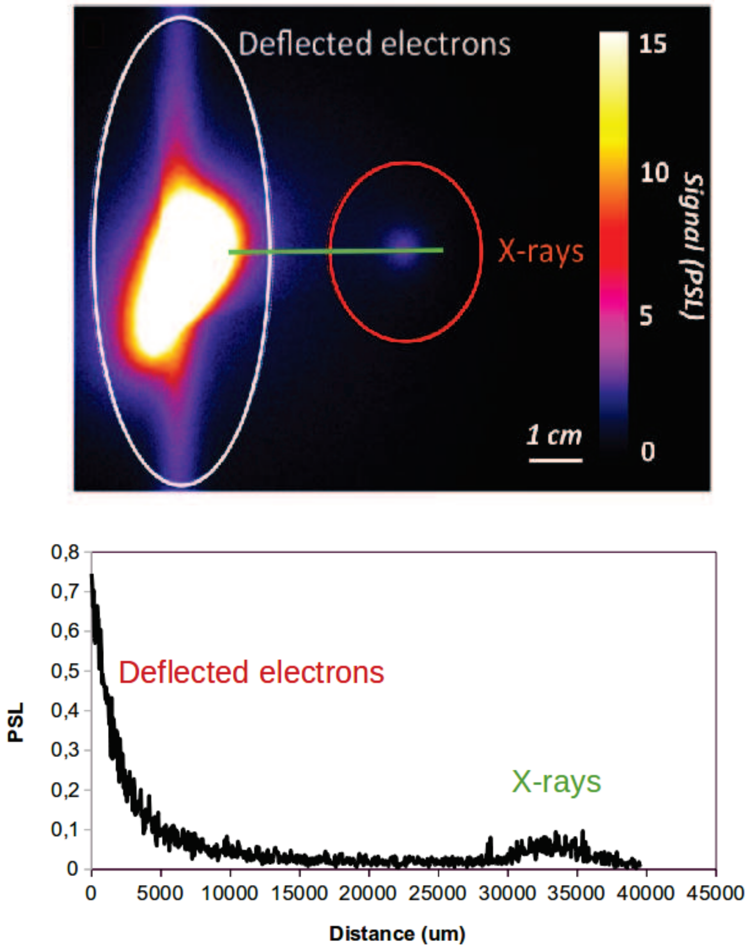

Figure 2.3: (a) The signal detected in the IP placed behind a dipole magnet installed at the exit of the beam pipe. The small spot corresponds to the X-rays signal and the big spot to the electrons signal. (b) the PSL values as a function of the distance of a horizontal profile of the IP.

by a dashed circle in the IP scanned image (see Fig. 2.2). A value of the RMS (d=4357 μm in this figure) was obtained from the Gaussian function which fits the signal very well. This width is a convenient choice when edges of normally distributed data must be specified as it contains 99.7% of all values. We therefore integrated the signal in a radius of 1.3 cm (= 3 RMS).

Each measurement is repeated five times providing therefore the relative uncertainty of the measurement. Moreover, these measurements were performed with different samples of each IP type. The relative uncertainty we obtain is, at the level of the beam charge measurement, ensures we have a good homogeneity of the IP responses.

The response of each type of IP is the mean of the five measurements. The relative deviation between each measurement is 5%. Tab. 2.2 and Fig. 2.4 present the response of MS, SR, TR, MP and ND IPs, using 5, 10 and 18 MeV electrons. The response function values for IPs are almost constant when the electron energy increases from 5 to 18 MeV. Looking at Tab. 2.2, we note that the IP sensitivities increase from ND to TR to SR, MP and MS.

As detailed in Tab. 2.3, we consider four sources of errors. The error in the charge measurement is included in the relative uncertainty. We add quadratically the related uncertainties on the fading correction and the uncertainty on the Wratten filter transmission to a total error of 12%. We underlined here that this error holds for our scanner. Anyway, in order to take into account the dependence of the IP responses on the read-out (scanner, temperature etc ...) we took a conservative 20% error on the measurements, as show e.g. in Tab.2.2. Our results on SR IPs are in agreement with the existing data as shown in Fig. 2.4.

E(MeV)	MS	SR	TR	MP	ND
5	22.0 ± 4.4	5.9 ± 1.2	4.5 ± 0.9	14.7 ± 2.9	4.2 ± 0.8
10	22.5 ± 5.0	6 ± 1.2	4.6 ± 1.0	15.5 ± 3.1	4.3 ± 0.5
18	25.5 ± 5.1	6.6 ± 1.3	5.1 ± 1	16.2 ± 3.2	4.7 ± 0.5

Table 2.2: The IPs responses in mPSL/e^-.

As described in the introduction, two methods are used to calculate the sensitivities α in the following. The first method is Hidding et al. [25] model. We assumed that the response of the IP is proportional to the deposited energy in the sensitive layer of the IP. The α values were determined for each type of IP separately as the mean of five measurements for all energies.

The calculated values of the sensitivity coefficients α are shown in Tab. 2.4:

The second method is Bonnet. [29] model which takes into account the absorption of the scanner and the PSL photons. We should mention that the stopping power is almost constant in the active layer of IP between 5 and 18 MeV electrons

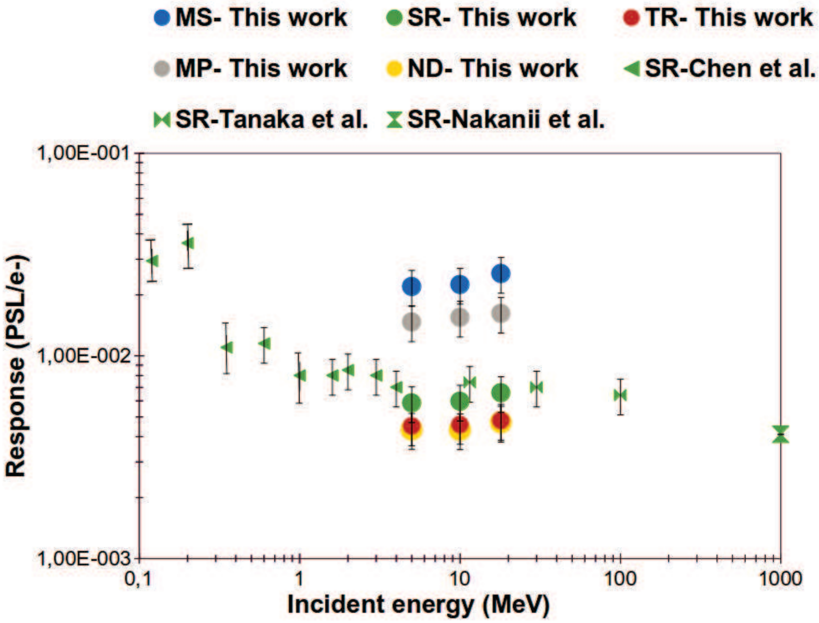

Figure 2.4: The measured electron response functions for the MS, SR, TR, ND and MP IP.

Error sources	Error values
Relative uncertainty	5%
Fading correction	10%
Charge measurement	5%
Wratten filter transmission	2%
Total error	12%

Table 2.3: Error bars. The error on the charge measurement is a contribution of the relative deviation.

α in (10^{-4}) PSL/keV	MS	SR	TR
Our work	5.2 ± 1.04	1.4 ± 0.28	2.80 ± 0.60

Table 2.4: The α values using the Hidding et al. model [25].

α in (10^{-4}) PSL/keV	MS	SR	TR
Our work	6.8 ± 1.3	2.2± 0.5	4.7 ± 0.9
T. Bonnet et al. [28]	6.95 ± 1.6	3.33 ± 0.8	4.85 ± 1.35

Table 2.5: The α values using Bonnet et al. model.

(See the introduction, Fig. 1.21 is almost constant), except for the last micrometers where we can see the contribution of the backscattered particles from the support layer. The increase due to this contribution is small. The integration is done analytically and the estimation of α with our data needs the use of the absorption length parameter L determined in [28].

The α values of the sensitivity coefficient were determined for each type of IP separately and the calculated values of the sensitivity coefficients α are shown in Tab.2.5. From this table, we can see the agreement between our values and the literature. The largest difference being 1.03 σ for SR IP.

Using the sensitivities α we determined from our data along with GEANT4 calculations and the absorption length L of the model of Bonnet et al., we have calculated the response functions of five types of IPs (MS, SR, TR, MP and ND) in the range [0.1-1000] MeV as shown in Fig. 2.5. From this figure we see the agreement between Hidding et al. and Bonnet et al. models [25, 29] for energies above 1 MeV and small differences for energies below 1 MeV. The small differences are directly connected to the non-flat energy loss profiles of low-energy electron, as shown in Fig. 1.20. Such a difference will increase towards lower kinetic-energy values, for which the electron range in the active layer, and in the protection layer for SR and MS IP, begins to be of the order or smaller than the thicknesses of these layers. For example, as computed with the NIST/ESTAR data base [50], the range of 0.1 MeV electrons in the active layer of an MS IP is approximately 80 μm, i.e. smaller than the active layer thickness (115 μm).

We also see that our simulations show a good agreement with the experimental data of Chen et al. [22], and the responses of IPs above 1 MeV are constant. The IP MS is more sensitive and the response is larger than for IP SR and TR. The signal in the MS IP is higher than in the SR IP even though they have the same thickness of the phosphoric film. This difference may be due to a different atomic composition of the phosphoric layer. Therefore, we may conclude that the atomic composition of the sensitive layer of MS IP is more efficient than the atomic composition of the sensitive layer of SR IP. We see also that the signal of TR IP is lower than the signal of MS IP. This difference may be related to the active layer thickness difference between TR IP on one hand and SR and MS on the other hand.

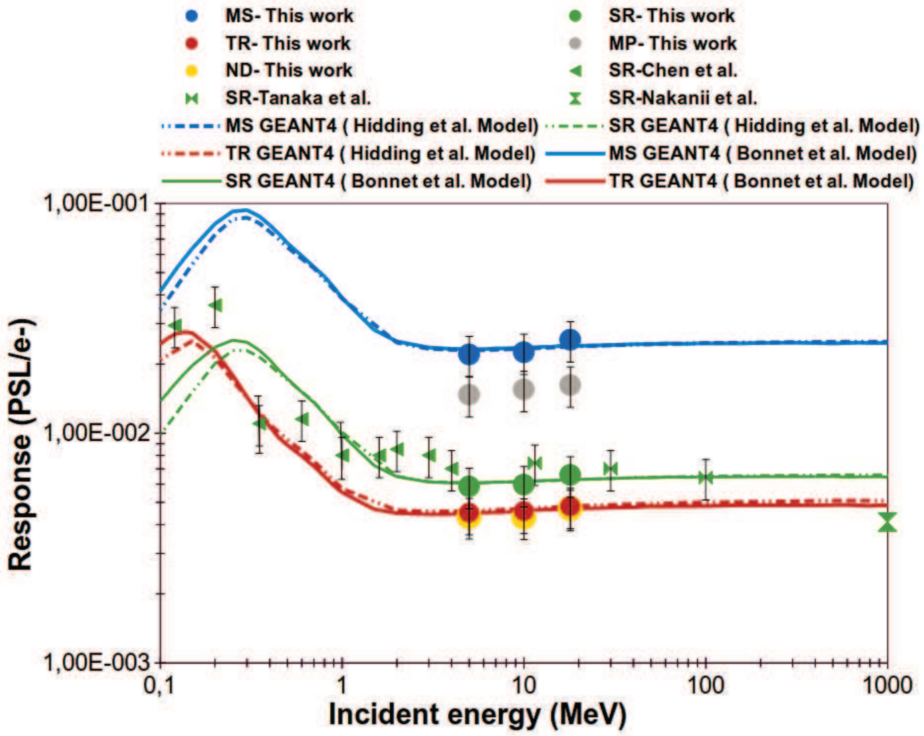

Figure 2.5: The response function for five types of IPs using two models that I described in this section, and comparison with the simulation GEANT4 and with the litterature.

2.1.3 Measurement of the relative sensitivities of different IPs with respect to the MS IP

In order to complete our measurement of the absolute IP responses and to eliminate the systematic uncertainties coming from the charge measurement or from the scanning process, we installed in the beam a setup consisting of an MS IP used as a reference detector and a detector composed of stripes of various IPs (MS-ND-TR-MP-SR) (see Fig. 2.6). With GEANT4 we checked that the energy losses of the electrons in both detectors are not influenced by the presence of the other in the beam. We did four identical measurements of this type. The ratios obtained from the measurement of sensitivities of different IPs are given in Tab. 2.6. Since this measurement allows to get rid of the main sources of uncertainty leaving just the uncertainty on the ratio of the fading corrections, we estimated the experimental errors of these ratios to be a few percent. We compared to these values the ratios of the sensitivities determined previously multiplied by the ratios of energy losses computed with GEANT4 (Eq. (2.1)).

$$R = \frac{\Delta E_{MS}.\alpha_{MS}}{\Delta E_{SR}.\alpha_{SR}} \tag{2.1}$$

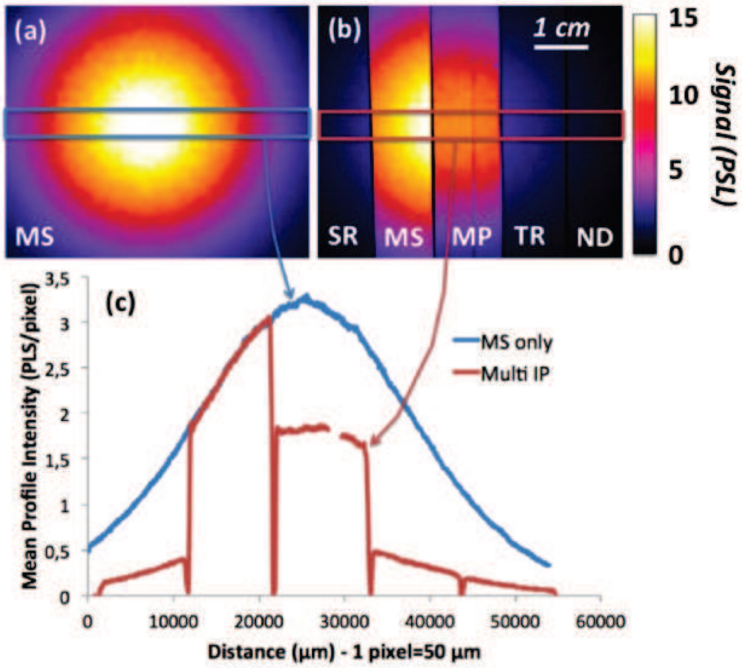

Figure 2.6: Recorded signal of the IP MS and a stripes made by various types of IPs.

E(MeV)		SR/MS	TR/MS	MP/MS	ND/MS
5	rel.	0.27 ± 0.03	0.2 ± 0.02	0.66 ± 0.07	0.19 ± 0.02
	sim.	0.26 ± 0.07	0.21 ± 0.06	X	X
10	rel.	0.28 ± 0.03	0.2 ± 0.02	0.63 ± 0.06	0.19 ± 0.02
	sim.	0.26 ± 0.07	0.21 ± 0.06	X	X
18	rel.	0.25 ± 0.03	0.19 ± 0.02	0.61 ± 0.06	0.18 ± 0.02
	sim.	0.26 ± 0.07	0.21 ± 0.06	X	X

Table 2.6: Ratio between the stripes made by various types of IPs and the MS IP.

2.1.4 Influence of the incident angle

SESAME and SEPAGE spectrometers will measure the electron and proton energy spectra at PETAL. In these two diagnostics, the incident angles of the particles impinging on the IP with respect to the IP normal will be as high as 80°. In our experiment at ELSA, an IP MS was rotated at angles between 0 to 45° with respect to the beam axis. The maximum angle was limited in this experiment because the profile of the electron beam became larger than the area of the detector when the angle exceeded 45°. The purpose of this measurement is to see the detection response of the IPs as a function of the angle. 10 MeV is the electron energy used for this measurement. As we can see from Fig. 2.7, the sensitivity increases when the angle increases very slightly in our experiment. GEANT4 simulations are in a good agreement with the experimental data. Note that each type of measurement was repeated 3 times to make results statistically more accurate. The curve is fitted by $1/\cos(\theta)$ as in Tanaka et al. [27], which corresponds exactly to the increased path length with the oblique incidence effect through the IP active area. We should note in Fig.2.7 that $1/\cos(\theta)$ law describes the GEANT4 simulations rather well up to 50° for 5 MeV electrons and approximately 60° for 10 and 18 MeV electrons. The divergence between the $1/\cos(\theta)$ law and the GEANT4 predictions come from the contributions of secondary particles. Notice that in this energy range, the electron range in the active layer material can be estimated to be larger than 1 cm, i.e. much more important than the active layer thickness [50]. Therefore, the dependence of the IP response on the electron energy can be neglected here.

The errors in the angles are 4% and are given by the positioning accuracy of the IP. The errors on the responses of IP correspond to the total error.

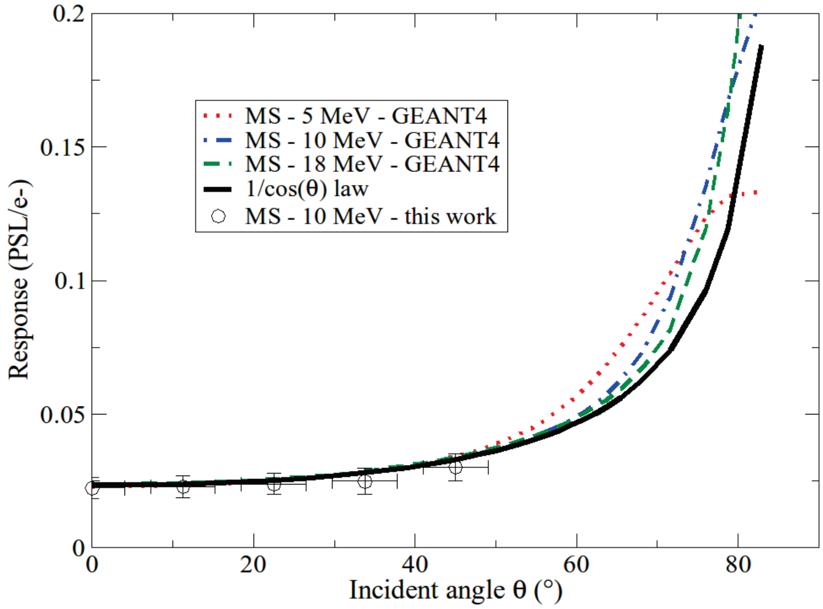

Figure 2.7: The response of IP signal in function of the incident angle.

2.1.5 Influence of tungsten plates placed around the IP-MS

As explained in the introduction, the IPs used in SEPAGE and SESAME will have to be shielded against high-energy primary and secondary photons produced by the interaction of PETAL with its target. For this purpose, high Z-material with various thicknesses placed behind or/and in front of the IP will be used. Moreover, in these diagnostics, for electrons, IPs will be placed in front of an aluminum support of 2 mm thickness, and installed in a tight mechanical structure. As for the ion and proton detectors, they will be placed in front of a 5 mm tungsten shielding plate. The presence of these mechanical parts may modify the IP response. The influence of the support on the IP signals must thus be well known in order to determine the particle spectra and to allow good detection conditions in the IP.

To study such an influence we measured IP responses inside stacks of IPs and high-Z plates.

In our experiment, various tungsten plates with a thickness between 1 and 5 mm, are placed behind an MS IP. The three energies (5 MeV, 10 MeV and 18 MeV) were used for such a study. As we can see from Fig. 2.8 the signal increases by 60% up to 2 mm of tungsten for electrons of 5 MeV. Above 2 mm of tungsten the signal does not vary, for all energies. In order to compare the experimental data with the simulation, the electron sensitivity of a single IP MS is used and shown in Tab. 2.4. We see that the simulation results are in good agreement with the experimental data. For 18 MeV the signal increases by 10-20% and 25-30% for 10 MeV electrons. The relative error on the response functions is 5%. We conclude that the increase of the signal depends strongly on the electron energy and 1 mm of tungsten layer is enough to make it independent of the material behind the IP. This will improve also the signal to noise ratio of our detectors, which is important especially during the PETAL laser energy ramp up at the beginning of operations.

A simulation to determine the origin of the signal in MS IP with tungsten behind was done. Fig. 2.9 shows the results for electrons of 5, 10 and 18 MeV.

The ratios Q(I) defined in Eqs.(2.2) and (2.3) are used in Fig. 2.9. By definition, Q(I) is only sensitive to the relative uncertainty of the measurement, i.e. independent of the absolute efficiency of the reference detector. I is the index of the measurement.

For the simulation :

$$\mathrm{Q(I)} = \frac{\mathrm{Edep(MS(I))}}{\mathrm{Edep(MS(0))}} \tag{2.2}$$

For the experimental data:

$$\mathrm{Q(I)} = \frac{\mathrm{R(MS(I))}}{\mathrm{R(MS(0))}} \tag{2.3}$$

The three curves depict contributions in the electron energy loss inside the active layer of the MS IP : 1) primary particles (orange); 2) primary particles + secondary particles (yellow); 3) primary particles + secondary particles + photons (green). It must be underlined that with our simulation the reference detectors response (R(MS(0))) is computed with all the contributions taken into account.

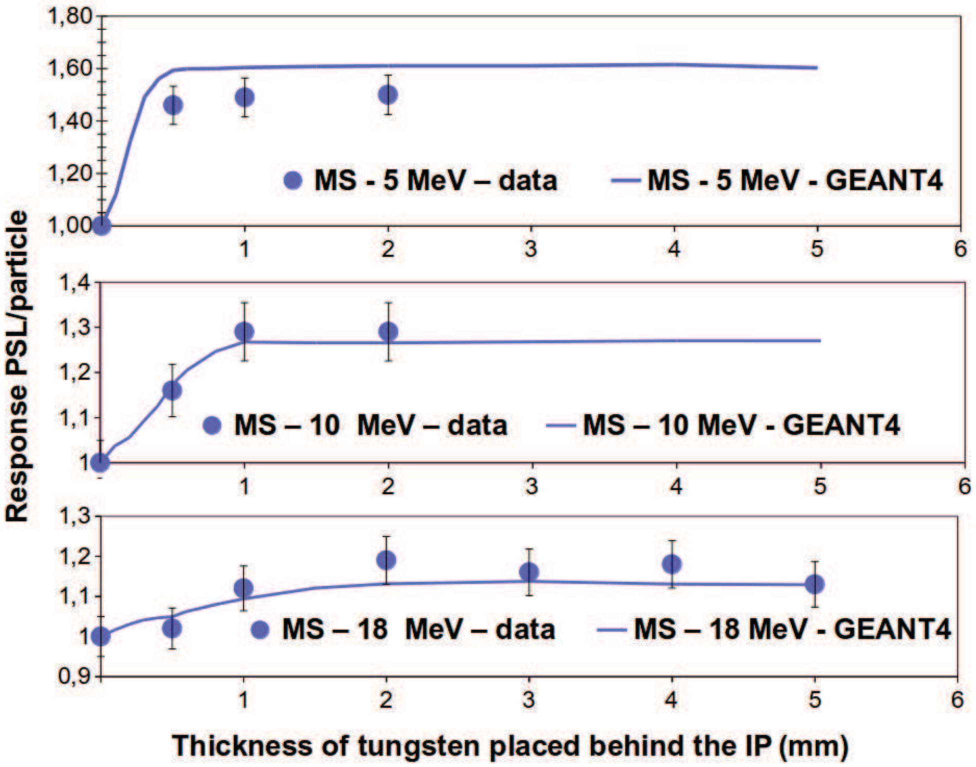

Figure 2.8: The response of IP signal as a function of the thickness of tungsten plates placed behind the IP.

The yellow curve is from 50% to 100% higher than the orange curve. The green curve is higher by a few percent than the yellow curve. This means that the additional amount of the signal comes from the interaction of secondary photons with the IP active layer which produce low-energy electrons that stop inside the IP active layer and increase the total amount of signal.

The last part of the experiment is the measurement of stacks composed of multiple MS IPs and tungsten layers. i.e. with IPs shielded with tungsten in the back and in the front. We must underline that inside SEPAGE the high-energy photon background will impinge on the detectors both from the front i.e. where the charge particles come from the back. Therefore, shielding IPs in the front may also be necessary.

Two types of stacks were chosen as a mock-up detection system in SEPAGE and SESAME for electrons below 20 MeV. One of the stacks, for the low-energy

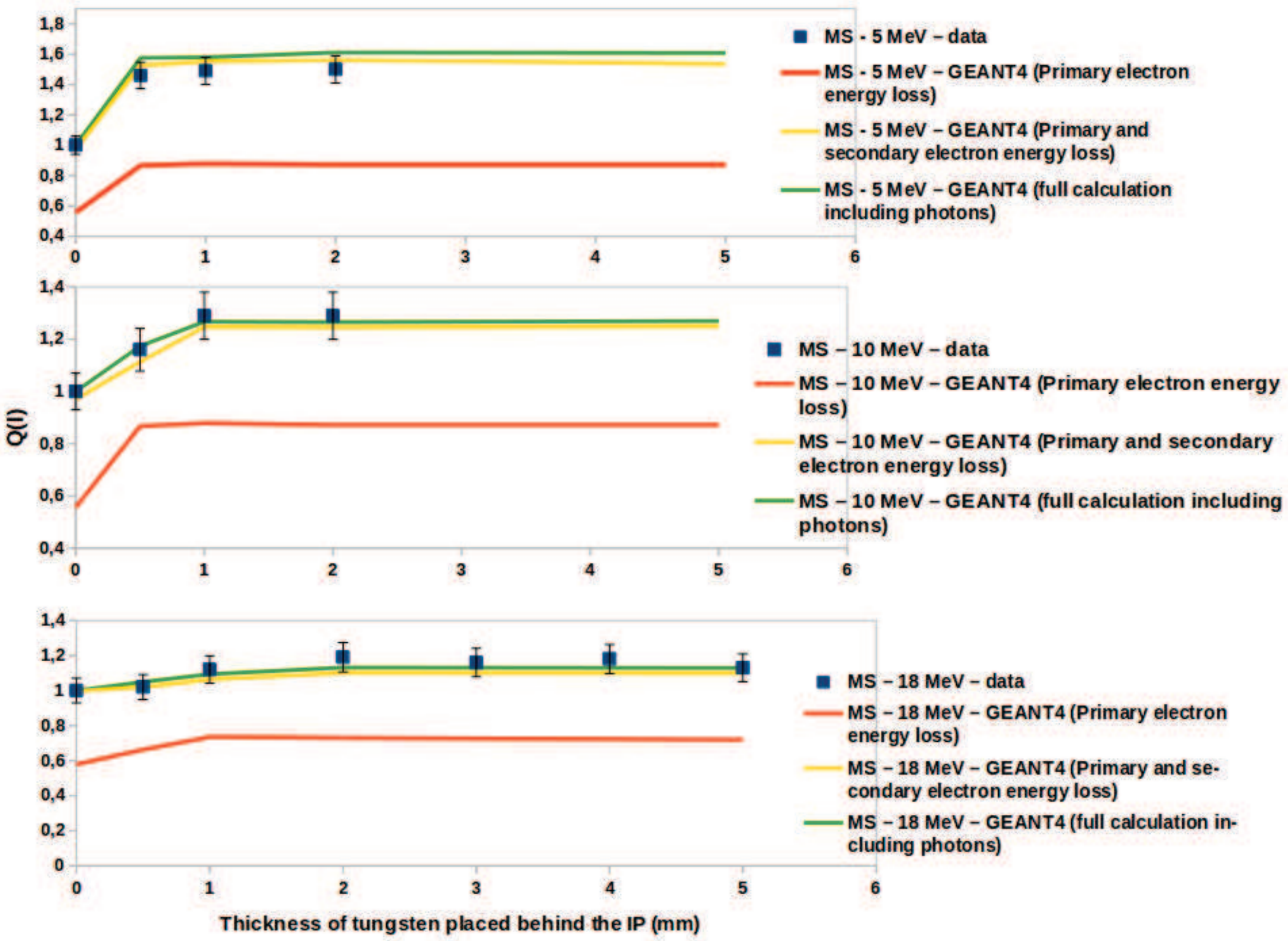

Figure 2.9: Q(I) as a function of the thickness of tungsten filter.

channel in SEPAGE is composed of TR IP+tungsten (0.1 mm)+MS IP+tungsten (2 mm). As mentioned before the TR IP is not covered by a protective layer. The reason for using a TR-IP as a first layer is to detect very low-energy particles. Note that the low-energy channel in SEPAGE covers the energy range of [0.1 - 20 MeV]. The other mock-up, for the high-energy channel is composed of tungsten (0.1 mm)+MS+tungsten (0.1 mm)+MS+tungsten (2 mm). In order to slow down the particles, tungsten with high Z-material is placed in front (see Fig. 2.10). The presence of tungsten in the stack is needed in order to add backscattering effect to the signal detected in IP, and thus increase the signal quantity in a defined manner. The used value for the sensitivities are that for single IPs.

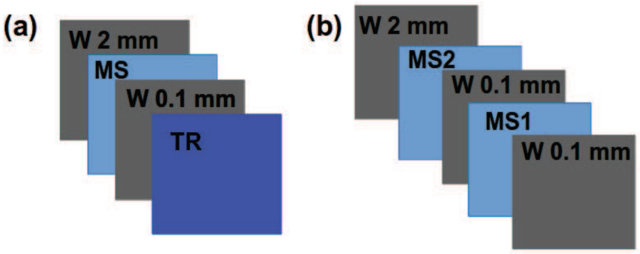

Figure 2.10: The compositions of two stacks tested at ELSA. (a) is the stack L.E to detect low-energy particles and (b) is the stack H.E to detect high-energy particles.

Figures 2.11 and 2.12 show the obtained experimental results and the comparison with GEANT4 simulations using the model of Hidding et al. [25]. Note that in the energy range used at ELSA, both models of Hidding et al. and Bonnet et al. are equivalent essentially because of the constant energy loss profile of the electrons in the active layer of the IPs as previously described. In each figure the responses of the IPs in the stacks are compared with that of a single IP. As shown in Fig. 2.11, the response of the IPs in the stack is increased by approximately 50% at 5 MeV for the MS type and 30% for the TR IP. This increase is reduced for the two other points, at 10 and 18 MeV. For the high-energy stack we see from Fig. 2.12, that the response of IP MS2 within the stack increases by a factor of 2.53 at 5 MeV, 2 at 10 MeV and 1.5 at 18 MeV.
Comparing these results to what we found in the previous section with tungsten behind IP, we conclude that contributions from tungsten in front of the IP is important.

The signal of the IPs in the stack is larger than the signal of a single IP (see Figs. 2.11, 2.12). Simulations were used to determine the physical origin of the increase of signal on the IP for both stacks (low and high-energy). We see from Figs. 2.13, 2.14, 2.15 and 2.16 where the quantity Q(I) defined above is used, the contributions in the electron energy loss inside the active layer of the MS IP. The primary and secondary electron energy loss curve is higher (by 60% and 80%) than

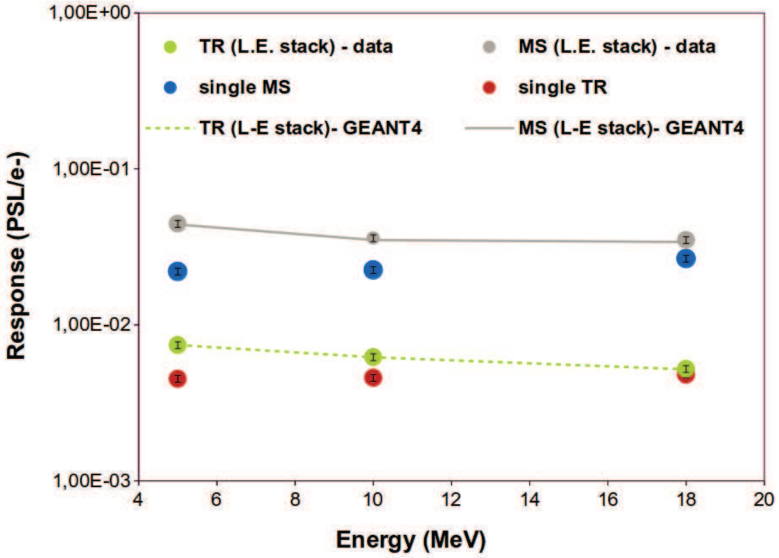

Figure 2.11: The response of MS and TR IPs of the "low−energy" stack, compared to the GEANT4 simulation.

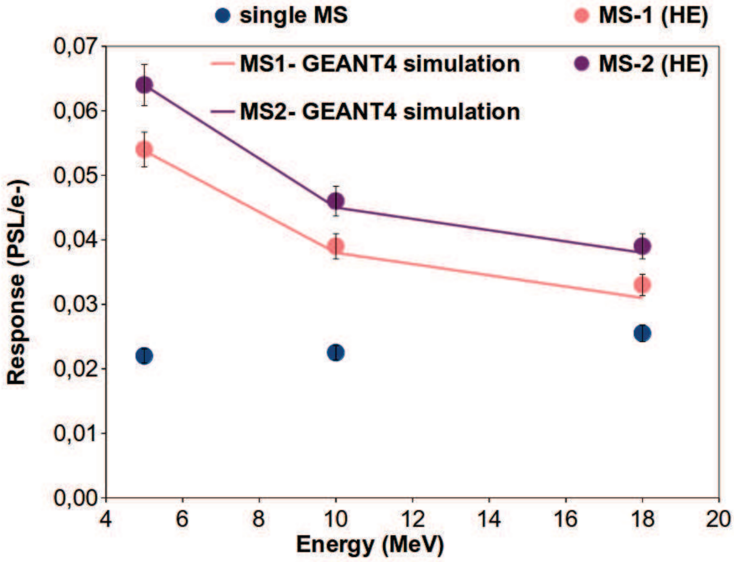

Figure 2.12: The response of MS IP for the "high−energy" stack and the comparison with the simulation GEANT4.

the primary electron energy loss curve, The full calculation curve is higher by a few percent than the primary and secondary electron energy loss curve, which means that the additional amount of the signal comes essentially from the interaction of secondary electrons with the IP active layer which produce low-energy electrons and gammas absorbed inside the active layer that increase the amount of signal. As mentioned above, in these stacks, the main additional contribution to the IP signal comes from the tungsten in front of the IPs.

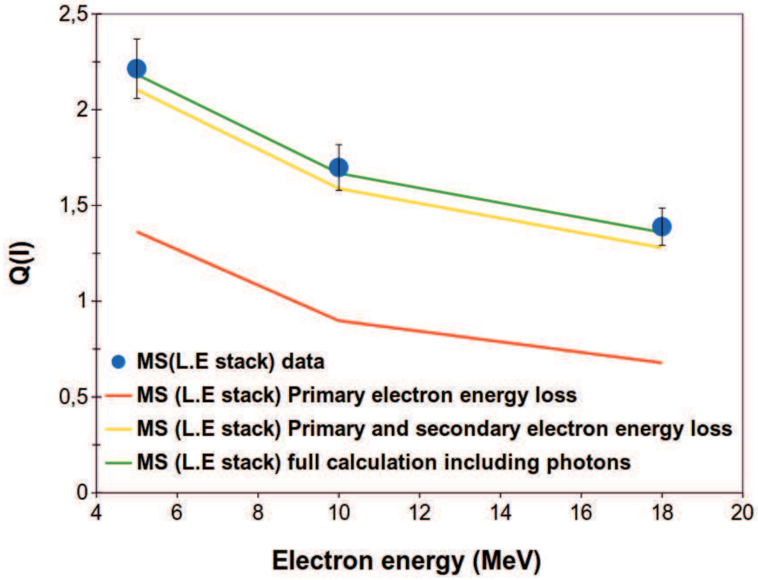

Figure 2.13: The ratios Q(I) for the MS IP in the "low−energy" stack (see text and Fig. 2.11 for the definition of this stack).

2.2 The response functions of IPs to electrons in the 40-180 MeV range at LOA facility

The IPs were calibrated using an electron laser-plasma source at the Laboratoire d'Optique Appliquée (LOA), Palaiseau, France for electrons in the hundreds MeV range. The setup consists of the electron source, a magnetic spectrometer and a Lanex screen as the reference detector to measure the electron beam energy

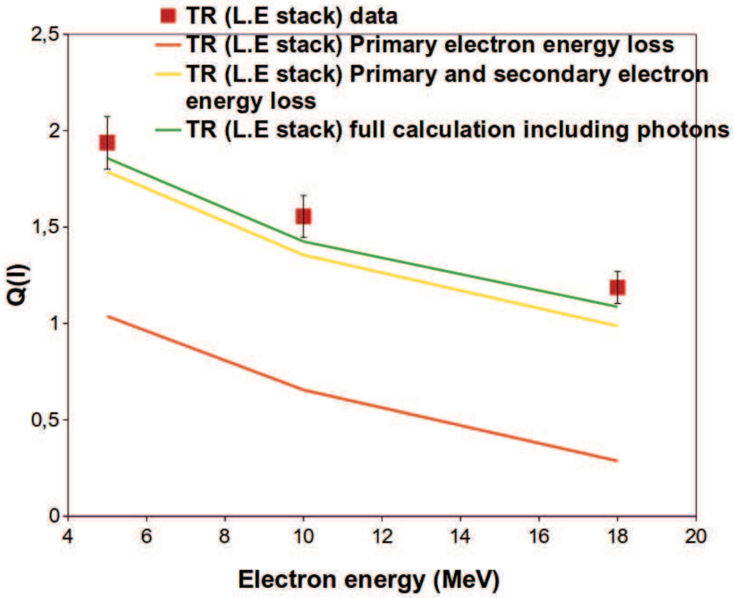

Figure 2.14: The ratios Q(I) for the TR IP in the "low−energy" stack (see text and Fig. 2.11 for the definition of this stack).

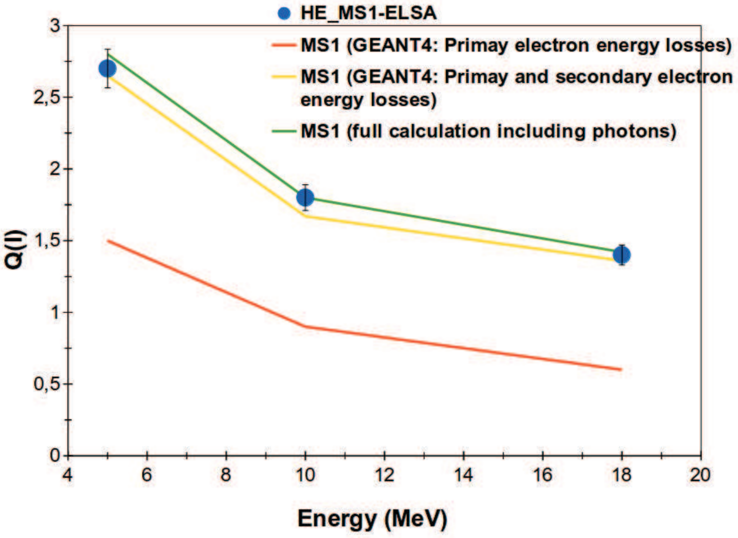

Figure 2.15: The ratios Q(I) for the MS1 IP in the "high−energy" stack (see text and Fig. 2.12 for the definition of this stack).

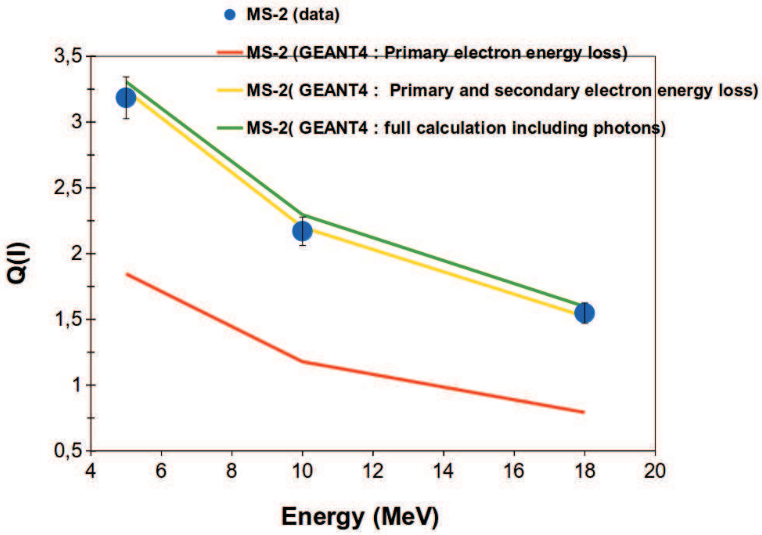

Figure 2.16: The ratios Q(I) for the MS2 IP in the ”high−energy" stack (see text and Fig. 2.12 for the definition of this stack).

spectrum and charge.

2.2.1 Experimental setup

The laser-plasma electron accelerator located in the “Salle Jaune” at LOA is a high-energy electron source. It is described in some details in S. Corde et al. [71]. It is an evolution from a setup first used by A. Rousse et al. [61]. The laser source provides pulses with a duration of 30 fs, a maximum energy of 2 J after compression and a maximum repetition rate of 1 Hz. The central wavelength of the laser is about 800 nm. The interaction of the short-pulse laser of 60 TW with an underdense plasma occurs in a helium gas jet target. The electron density reached in this setup is of the order of 10^{19} cm^{-3}.

The laser pulse was focused on a helium gas jet target produced by a supersonic Laval nozzle with a typical backing pressure of a few bars. The gas in this regime is quickly ionized by the rising edge of the laser pulse, and underdense plasma, which the laser pulse can propagate through, is created. The laser pulse pushes electrons within the plasma out of regions with high laser intensity by the ponderomotive force (ions can be considered motionless due to their high mass) and a moving plasma wave called "wakefield" is created. When electrons are injected into the accelerating phase of this plasma wave, they can be effectively accelerated. A typical accelerating length of hundreds of micrometers is achieved in the millimeter-scale plasma [75]. This way, electrons can be accelerated to energies of up to a few hundreds of MeV during the experiments.

This accelerator generates electron bunches up to hundreds of MeV with a tens-of-femtosecond duration, a divergence below 5 mrad and a charge up to 100 nC.

The calibration process of our detectors requires an independent measurement of the charge and energy of electron beams. A magnetic spectrometer consisting of a dipole magnet system to disperse electrons based on their energy was used in the experiment. The electrons behind the magnet were detected by a Lanex screen and a CCD camera. From the absolute calibration of this diagnostic system, we were able to obtain the electron beam charge necessary for our purpose. The main advantage of the setup was the possibility to insert imaging plates into the system between the magnet and Lanex screen without noticeably perturbing the measurement on the Lanex screen. We computed with GEANT4 simulations that electrons in the energy range covered by our experiment were hardly affected by our thin detectors and that the Lanex screen was far enough from our detectors not to influence them. Therefore, it was a suitable method of diagnostics for our needs. This can also confirmed directly during the experiment by comparing the images obtained on the IPs with those on the Lanex screen (see Fig. 2.20 below.)

Our setup of the electron diagnostics allowing the IP calibration was installed outside the interaction vacuum chamber. The dipole magnet and the position of the Lanex screen with respect to the magnet define the energy range for which the spectrometer can be used. In addition, the wall of the vacuum chamber provides an extra shielding of the electron diagnostics from the radiation of the laser-created plasma in the target area. The angular scattering as well as the energy losses of the generated relativistic electrons in the vacuum window and in the air outside the chamber were small and can thus be neglected. Moreover, due to the electron energy measurement setup being placed outside the chamber and the fact that the IPs were placed behind the electron spectrometer, the vacuum chamber with the laser-plasma accelerator inside can be considered (for the purpose of the

	50 MeV	100 MeV	150 MeV
Deposited energy MeV	1.45	2.24	10.69

Table 2.7: The deposited energy of electrons in the 1 cm vacuum glass window of the setup.

IP calibration) as a black box providing the relativistic electron beams, because all properties of the electron beams are measured outside the vacuum chamber. Another advantage is to save time on switching IPs, installing stacks of IPs and high-Z filters, and minimizing the fading of the IP signals as well as optimizing the time efficiency of the experiment.

The dipole magnet consisted of two plane magnets, between which electrons are passing through the gap of length $L_{mag} = 100$ mm, width $l_{mag} = 100$ mm and height $h_{mag} = 10$ mm (see Fig. 2.17). The dipole magnetic field was measured to be $B = 1.1$ T in the gap and 0 outside. The fringe field zone was measured to be sufficiently small to neglect its effect on the electron transport. A magnetic field of this kind hence provided conditions to derive analytical formulas for electron trajectories through the setup.

The electrons accelerated by the laser wakefield acceleration were propagating through a glass window of 1 cm thickness. The average energy loss of the electrons in this window was in the order of a few MeV. The energy losses of the electrons in the vacuum window is shown in Tab. 2.7. Its effect on the energy spectra does not have to be taken into account in our experiment since the electron beams were characterized by the magnetic spectrometer downstream.

The electrons were entering the magnet system (See Fig. 2.17), which was at the distance $D_{JM} = 800$ mm from the electron source. One of the edges of the Lanex screen was placed on the magnet axis at a distance $D_{ML} = 160$ mm. The Lanex screen was positioned at the angle $\theta_{Lanex} = 48°$ with respect to the direction orthogonal to the laser axis and the length of the screen in the dispersive plane of the system was $L_{Lanex} = 170$ mm. By introducing a coordinate system (x,y) with the origin $O_{xy} = (0, 0)$ at the intersection of the electron trajectory with the front edge of the magnet (the x-axis following the laser axis, see Fig. 2.17), it

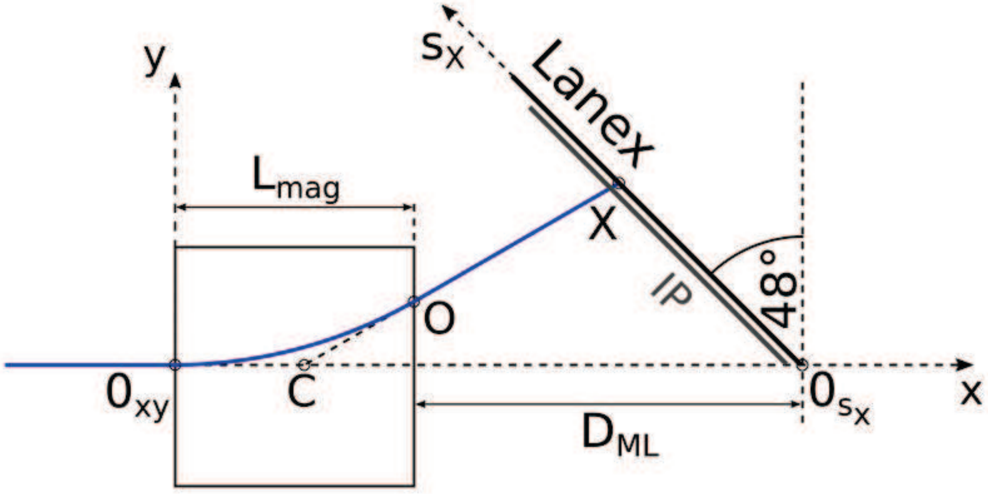

Figure 2.17: The setup of the spectrometer and the definition of the parameters.

can be written for the coordinates of electrons at the magnet exit:

$$(\mathrm{x}_0, \mathrm{y}_0) = (\mathrm{L}_{\mathrm{mag}}, \mathrm{R} - \sqrt{\mathrm{R}^2 - \mathrm{L}_{\mathrm{mag}}^2}) \tag{2.4}$$

where R is the electron trajectory radius in the constant magnetic field B:

$$\mathrm{R} = \frac{\beta\gamma \mathrm{m_e c}}{\mathrm{eB}} \tag{2.5}$$

In this formula, $\beta = \mathrm{v/c}$ is the electron velocity normalized to the speed of light c, $\gamma = 1/\sqrt{1-\beta^2}$ is the relativistic Lorentz factor, $\mathrm{m_e}$ is the electron mass and e is the electron charge. The coordinates of the intersection of two straight electron trajectories before entering and after exiting the magnet can be written as:

$$(\mathrm{x_c}, \mathrm{y_c}) = (\frac{\mathrm{x}_0^2 + \mathrm{y}_0^2}{2\mathrm{x}_0}, 0) \tag{2.6}$$

Another point to consider is the intersection of the straight trajectory of electrons after exiting the magnet and the Lanex screen. We can write its coordinates as:

$$(\mathrm{x_X}, \mathrm{y_X}) = \left(\mathrm{L_{mag}} + \mathrm{D_{ML}} - \mathrm{y_x}\tan(\theta_{\mathrm{Lanex}}), \frac{\mathrm{y}_0(\mathrm{L_{mag}} + \mathrm{D_{ML}} - \mathrm{x_c})}{\mathrm{x}_0 - \mathrm{x_c} + \mathrm{y}_0\tan(\theta_{\mathrm{Lanex}})}\right). \tag{2.7}$$

We also introduce the electron dispersion defined as $\mathrm{s_X} = \mathrm{y_X}/\cos(\theta_{\mathrm{Lanex}})$. It represents the distance from the point $\mathrm{O_{s_X}}$ on the experimental axis. The dispersion curve $\mathrm{s_X} = \mathrm{f(E)}$ obtained using the parameters given above is shown in Fig. 2.18.

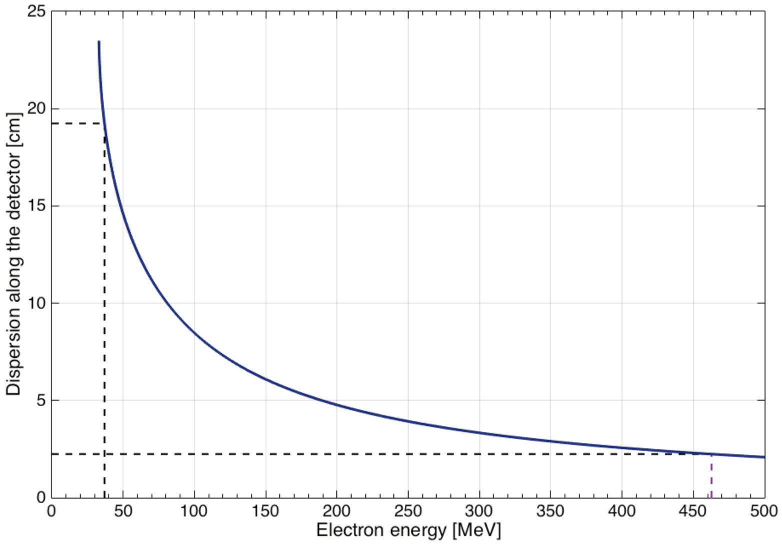

Figure 2.18: The dispersion along the Lanex screen (cm) with respect to the electron energy (MeV). The active zone of Lanex from 0 to 17 cm and the energy range covered by the Lanex screen is from 36.9 to 462.7 MeV.

All formulas given above do not take into account the divergence of the electron beams. Our setup, however, allows measuring the divergence in the non-dispersive dimension using the signal on the imaging plates and on the Lanex screen. This total divergence comes from the convolution of the electron beam divergence at the laser-target interaction point and of multiple scattering of the electrons in the glass vacuum window. An average spatial spreadth of 7 mm (FWHM) on the Lanex screen (as can be seen in Fig. 2.20) was taken.

When taking into account the dispersion curve of Fig. 2.18 this spatial spreadth corresponds to an energy spreadth between 2 and 10 MeV in our energy range. This is of the order or lower than the energy bins of 10 MeV we took for the energy dependences of our detector responses.

The Lanex screen consists of a polyester support of 178 μm and a phosphoric layer of 84 μm which emits visible light (around 546 nm) when an ionizing particle

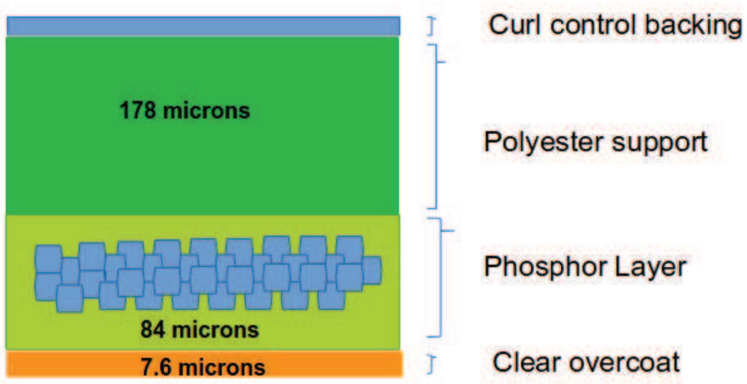

Figure 2.19: The Lanex screen composition and thicknesses.

such as an electron passes through. It is composed also of a support and a thin curl (see Fig. 2.19). We assume that the emitted energy is proportional to the energy deposited in this layer by the particles. This can be done as long as electron energies are above 1 MeV, where the energy deposited in the phosphoric layer of the Lanex screen becomes independent of the incident electron energy [33]. The fraction of the photons, which are emitted by the Lanex screen and which escape its back side, is then collected by the pixels of a camera and converted into a recorded signal based on the quantum efficiency of the CCD. Fig. 2.20 shows a recorded signal simultaneously on an IP and on a Lanex screen.

The comparison of the signal on the IP and the signal on the Lanex screen allows an absolute positioning of the IP with respect to the Lanex screen and to the magnet transport as long as the detector in front of it can be considered as "thin". This enables the electron energy calculation on the IP. We verified this method by comparing profiles of the signals obtained from imaging plates and from the Lanex screen in the same shot, as explained and quantitatively compared in Fig. 2.21. The signal shape is the same for both detector types, and therefore can be used to correct the position of the imaging plate.

There is a small difference in the compared signals in the Lanex screen and IP, which is caused by the thickness of the detectors and the non-perpendicular trajectories of the electrons. The error in the energy determination due to this

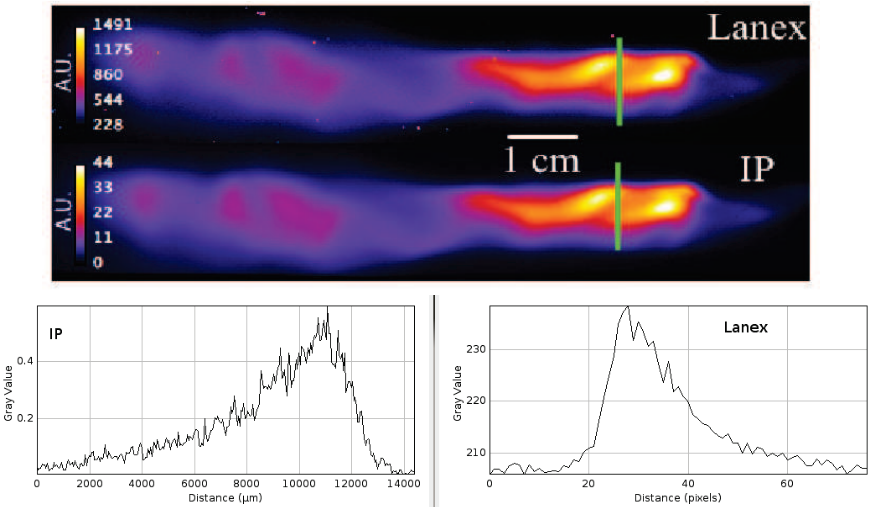

Figure 2.20: Comparison of the recorded signal on the Lanex screen with the signal on the IP.

effect is smaller than the error caused by the divergence of the electron beam, and can thus be neglected. The average energy loss of electrons is $\Delta\mathrm{E} \sim 160$ keV. Using the largest value of dispersion in our energy range of this setup, which corresponds to $\frac{\mathrm{dS}}{\mathrm{dE}} \sim$ 0.3 cm/MeV and thus δS— 120 μm, this corresponds to a maximal shift of 0.5 mm.

For selected energy interval (in our case the intervals are chosen to be the size of 10 MeV), both the charge from the Lanex screen and the PSL from the IP were calculated. PSL/e^- can then be determined for every energy interval.

2.2.2 Electron spectrum measurement

The spectrum and charge measurement with the Lanex screen requires a comprehensive amount of information about all parts of the experimental and diagnostic setup. These parameters were either measured in the laboratory [33] or can be calculated. The scintillator layer of Kodak Lanex Fine contains molecules of $\mathrm{Gd_2O_2S : Tb}$ with the density ρ(Lanex)=7.44 g/cm^3 and with the phosphoric surface loading $\mathrm{h_S}$=0.033 $\mathrm{g/cm^2}$. The number of photons $\mathrm{N_{cr}}$ created in the Lanex phosphoric layer at the central wavelength per incident electron can be calculated

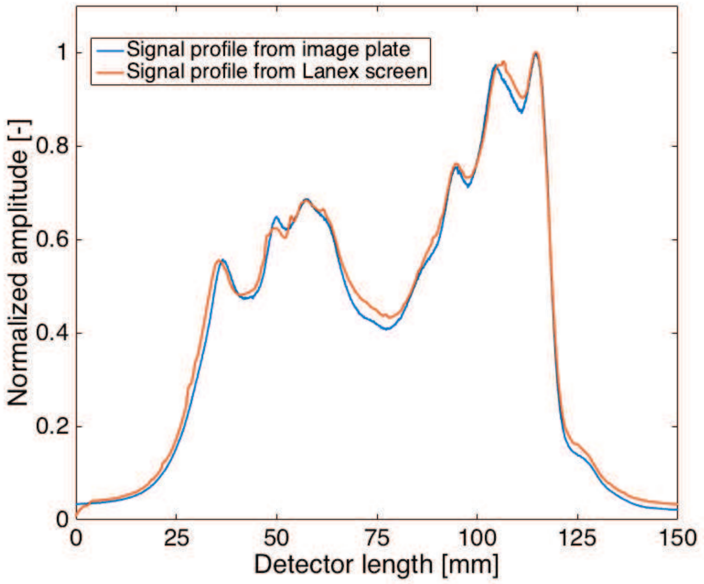

Figure 2.21: The comparison of the signal profile obtained from an imaging plate (blue) and the profile detected by the Lanex screen (red). The amplitude of the uncalibrated profile is normalized to unity in order to compare the shape of profiles. The relative position of profiles is changed based on the position of the maxima.

as:

$$\frac{\mathrm{N_{cr}}}{\mathrm{N_{el}}} = \frac{1}{\mathrm{E_{ph}}}\epsilon\frac{\mathrm{dE}}{\mathrm{dx}}\delta\mathrm{x} \tag{2.8}$$

where $\mathrm{E_{ph}}$=2.27 eV is the energy of photon with the wavelength of 546 nm (other wavelengths will be absorbed inside a bandpass filter in front of the CCD camera), ϵ is the fraction of the energy loss converted into phosphoric photons and dE/dx is the stopping power (combined together $\epsilon\mathrm{dE/dx} = 1.8 \pm 0.2$ MeV/cm represents the measured yield of electron kinetic energy that is transformed into visible light). Note that this yield is energy independent for electron energies above 1 MeV (as is stated above). Furthermore, $\delta = \mathrm{h_S}/\rho_{\mathrm{Lanex}}.cos(\theta_\perp)$ is the equivalent thickness of $\mathrm{Gd_2O_2S}$, $\theta_\perp = \theta_{\mathrm{Lanex}} - \theta_{\mathrm{e}}$ is the angle between the electron trajectory and the normal to the Lanex screen, and the angle of the electron trajectory relative to the x-axis is $\theta_{\mathrm{e}} = \mathrm{atan}(\mathrm{y_X}/(\mathrm{x_X} - \mathrm{x_C}))$. the formula of the number of photons collected by a single pixel of the CCD camera per photon created in the Lanex screen is:

$$\frac{\mathrm{dN_{coll}}}{\mathrm{dN_{cr}}} = \zeta \mathrm{g}(\theta_{\mathrm{CCD}})\mathrm{q_l q_w q_f}\delta\Omega \tag{2.9}$$

where $\zeta = 22\%$ is the transmission output factor of photons, $\mathrm{g}(\theta_{\mathrm{CCD}}) = \cos(\theta_{\mathrm{CCD}})/\pi$ is the angular distribution of photons escaping the Lanex screen [73] where θ_{CCD} is the angle between the CCD camera and normal to the LANEX screen, $\mathrm{q_l} = 0.95$, $\mathrm{q_w} = 0.95$ and $\mathrm{q_f} = 0.36$ are transmission factors of the camera lens, the camera window and the bandpass filter, respectively, and $\delta\Omega = 0.002$ sr is the solid angle of collection (given by the area of the camera lens and the distance of this lens from the Lanex screen). In order to detect phosphoric photons we used a 16-bit CCD camera Andor DV-420. This camera has a quantum efficiency QE = 26.5% at 546 nm and -20°C, and r=7 electrons are needed to create one count. Therefore, the CCD yield is:

$$\frac{\mathrm{dN_{cts}}}{\mathrm{dN_{coll}}} = \frac{\mathrm{QE}}{\mathrm{r}} \tag{2.10}$$

The formulas presented above, allow to derive the relationship between the number of electrons that reached the Lanex screen and the CCD signal:

$$\frac{\mathrm{dN_{el}}}{\mathrm{dE}}(\mathrm{E_0}) = \frac{\frac{\mathrm{Cts(E_0)}}{\delta \mathrm{s_{pix}}}\frac{\mathrm{ds_x}}{\mathrm{dE}}}{\frac{\mathrm{dN_{cr}}}{\mathrm{dN_{el}}}\frac{\mathrm{dN_{coll}}}{\mathrm{dN_{cr}}}\frac{\mathrm{dN_{cts}}}{\mathrm{dN_{coll}}}} \tag{2.11}$$

where $\mathrm{Cts(E_0)}$ is the integrated number of CCD counts corresponding to a given energy E_0, $\mathrm{ds_x/dE}$ is the differentiation of the dispersion with respect to the energy E, and $\delta\mathrm{s_{pix}} = 0.257$ mm is the pixel size projected on the Lanex screen. By substituting all parameters and formulas mentioned above into Eq. (2.11), the spectrometer system can be absolutely calibrated and electron spectra (the number of electrons per MeV with respect to their energy) for the laser-plasma electron accelerator are obtained. An example of a measured electron spectrum is shown in Fig. 2.22.

In order to prevent the alterance of the signal in the CCD camera by incoming electrons, a silver mirror with a reflection coefficient of 97% was placed between the CCD and the Lanex screen.

The reflection coefficient is taken into account in the electron charge calcula-

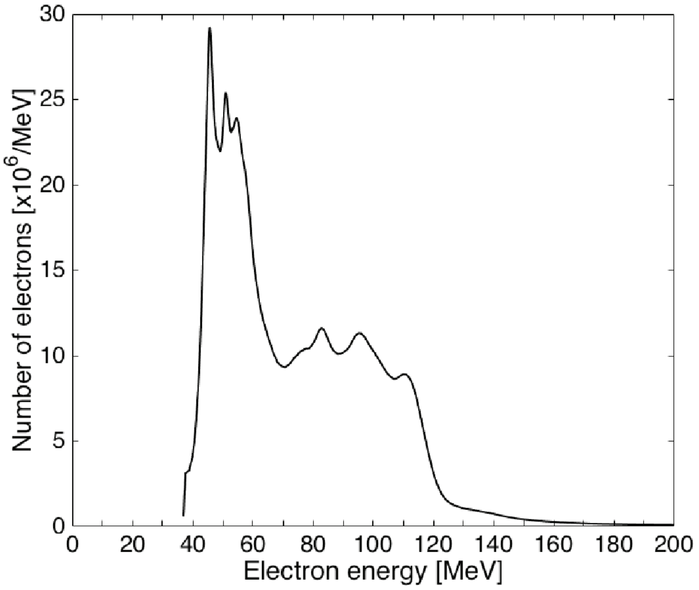

Figure 2.22: An electron energy spectrum obtained after deconvolution of the Lanex screen images. The amplitude of the spectra was determined using the parameters mentioned in the text.

tions in the rest of our study done at LOA facility.

The camera was shielded by 11 cm of lead brick, to protect it from X-rays. A small amount of X-rays still reach the camera during the exposure. Hence, by using the background substraction and median filter of 4×4 px area around each pixel of the CCD camera, the influence of detected X-rays on the camera was determined and found to be negligible.

The steps from the generation of the signal on the Lanex screen until the collection on the CCD needs uncertainty in the determination of the electron charge. The uncertainties are:
1/ 1% is the transmission factor of the green bandpass filter
2/ 1% in the transmission factor of the camera lens
3/ 1% in the photon collection by the CCD

Information about the measurement uncertainties, transmission factor of the interference filter and of the window used in the characterization done by Glinec et al. [33] is missing. Hence, if we consider these uncertainties in the photon collection during our experiment, we obtain an error of 3% from the quantified uncertainties (linear sum). This is smaller than the relative uncertainties we estimated by repeating the IP response measurements several times during the experiment (between 5 and 7 times) [47]. As for the ELSA experiment, in particular to test the homogenity of the Imaging Plate responses.

2.2.3 Responses of Imaging Plates

Fig. 2.23 and Tab. 2.8 show the Imaging plate responses (in PSL/e^-) for three types of IPs in the energy range [40-180] MeV. For MS IP we have data above 120 MeV, for which we have sufficient signal. For each type of IP we corrected the measured responses for the effective thickness variation as a function of the detector position and therefore of the electron energy. We took into account that the electrons were passing through IP under various and non-zero angles with respect to the detector normal based on their energy (θ_{perp} from $-8°$ for E= 40 MeV to 37° for E= 180 MeV). Indeed, a multiplication factor $\cos(\theta_{\mathrm{perp}})$ for the normalization of the IP signal to the electron trajectory normal to the IP detection was introduced.

From Fig. 2.23, we can see that the IP MS is more sensitive and the PSL/e^- quantity is larger than for IP SR and TR. This confirms what was observed at lower energy with the ELSA electron facility.

We can conclude from the same figure that the IP response to electrons is almost constant when the energy of electrons is increased, and our experimental data are in agreement with our previous experiment at ELSA and Tanaka et al. [27], [46].

In order to estimate the relative errors, the measurements were repeated seven times for each type of IP. The relative standard deviations are 5% for MS, 7% for SR and 3% for TR. The absolute error bars are larger than the relative error and are discussed below.

We fitted these results with one sensitivity parameter α for each type of IP. We used both models of Bonnet et al. and Hidding et al. Using these values of the sensitivities we computed the PSL/e^- responses and the comparison with GEANT4 simulation between 0.1 and 1000 MeV is shown in Fig. 2.24. In this figure, using Bonnet et al. (solid lines) and Hidding et al. (dashed lines) models, we provide the absolute responses for the MS, SR and TR IP over [0.1-1000] MeV

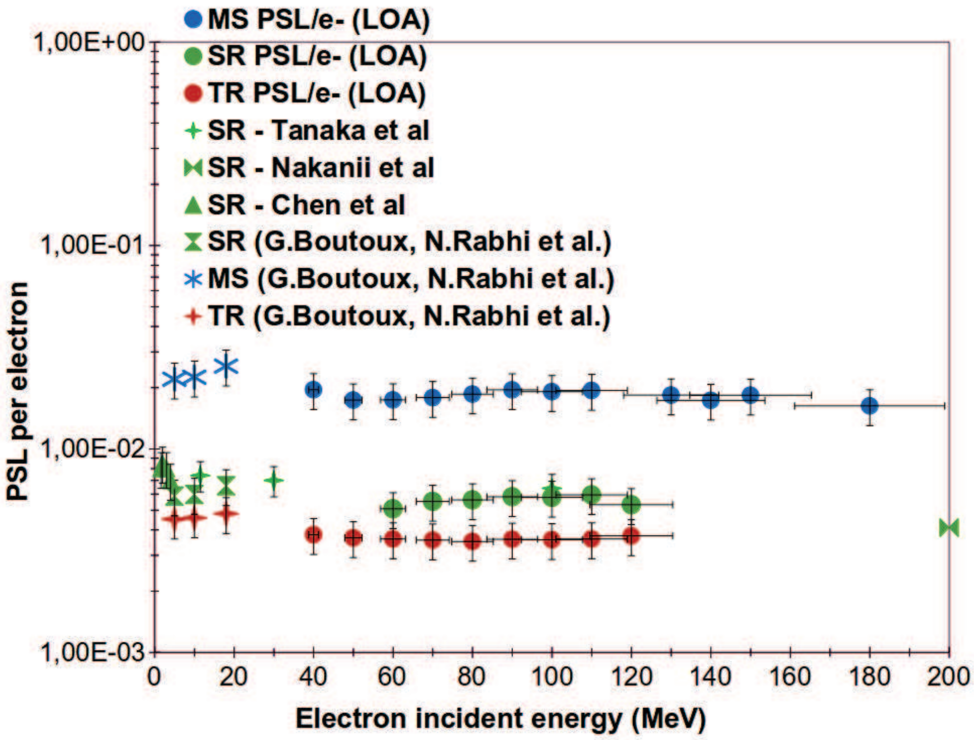

Figure 2.23: The responses for each type of IP as a function of the electron energy.

E(MeV)	MS (10^{-2}) PSL/e^-	SR (10^{-3}) PSL/e^-	TR (10^{-3}) PSL/e^-
70	1.9±0.4	5.8±1.2	3.7±0.7
80	2.0±0.4	6.1±1.2	3.8±0.8
90	2.1±0.4	6.5±1.3	4.0±0.8
110	2.2±0.4	6.9±1.3	4.1±0.8
120	2.3±0.4	6.2±1.2	4.4±0.9

Table 2.8: The responses of Imaging plates at different electron energies

energy range. Both models are close in the energy range above 1 MeV which is in fair agreement with our experimental data as well as the data from our previous experiment at ELSA and Chen et al. [22]. Below 1 MeV these two models diverge because the dE_p/dz profile is not constant inside the IP active layer.

As shown in Fig. 2.25, the stopping power in the active layer using high-energy electrons is constant except at the last micrometers of the layer, where additional

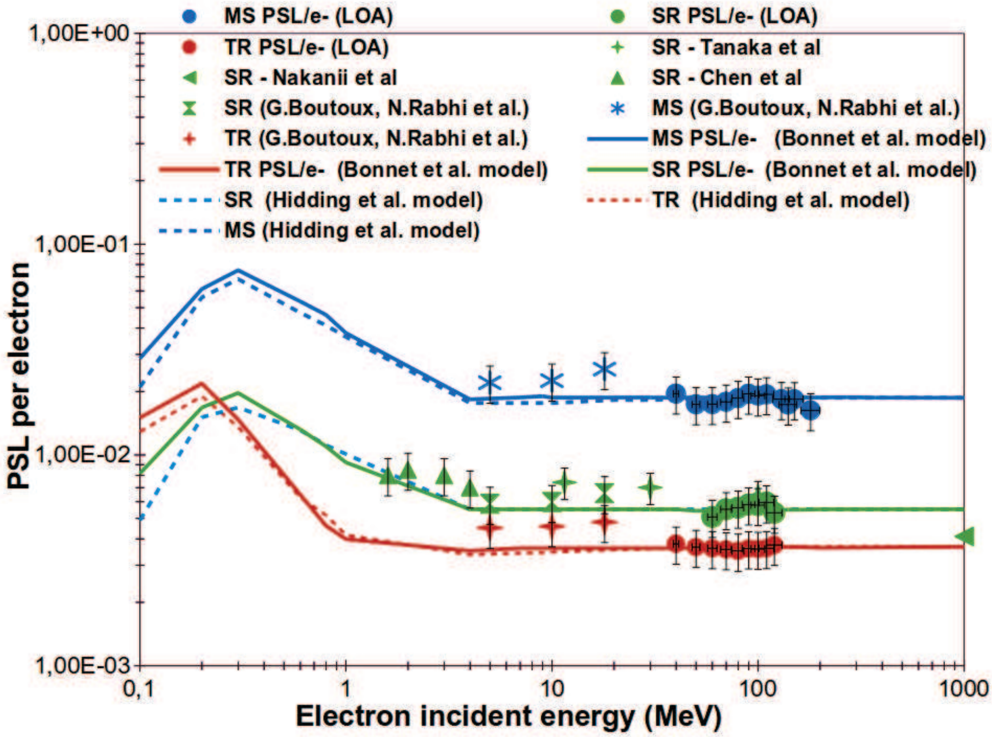

Figure 2.24: The response of IPs with respect to the incident electron energy.

contribution from the support layer can be seen, which can be taken out of the integral and the profile is integrated numerically. For this reason, both models are considered equivalent in our case. The sensitivities shown in Tab. 2.9 are calculated using the method of least squares and reproducing experimental points within the errors. The values show a good agreement with our results at lower energies.

2.2.4 Error estimation

In our experiment the fading time was 2 minutes with a few seconds uncertainties. The fading was 2 % for MS, 5 % for SR and 15 % for TR. Hence, the uncertainty for the fading correction is 7% of 2 %, 5 % and 15 % respectively and hence negligible. At the ELYSE facility the detection system composed of the Lanex screen and the CCD camera was calibrated by our collaborators of LOA [33]. The uncertainty on the absolute number of electrons given by the Integrating Current Transformers

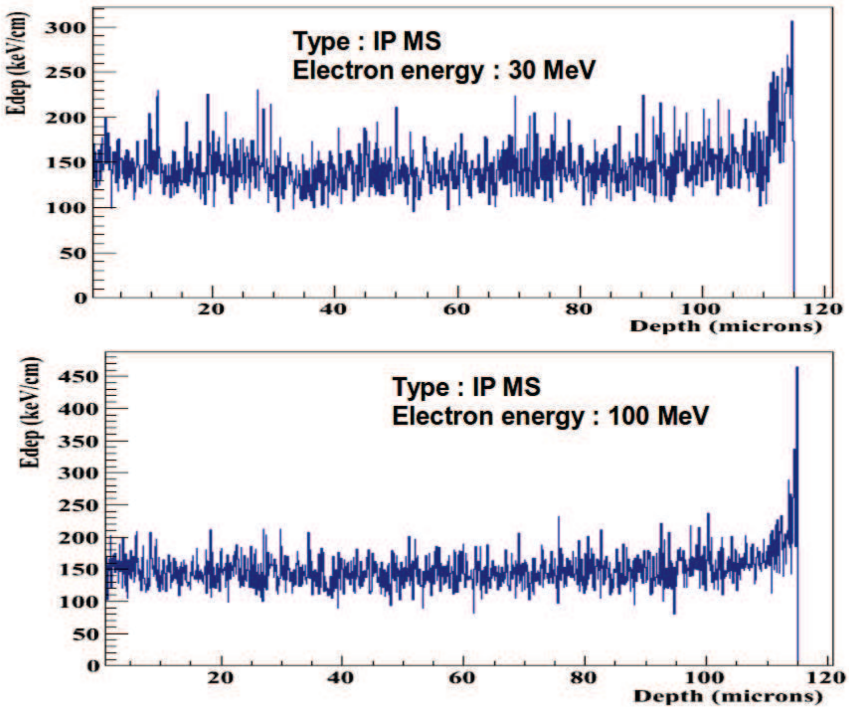

Figure 2.25: The stopping power of the IP MS for 30 and 100 MeV electrons along the thickness of the active layer.

(ICT) was determined to be around 50%. Anyway, the absolute uncertainty using the same type of measurement is estimated at only the 10% level in [74]. Due to the differences on the uncertainties between [33] and [74], we decided to estimate them from our own data sets. In this respect a comparison of our data with those of our experiment at ELSA [46] is interesting.

As shown in the second column of Tab. 2.10, the sensitivities from ELSA were multiplied with the average deposited energy of the obtained calculation from GEANT4 simulation. In the third column, we calculated the mean value for each type of IP. The fourth column contains the RMS of the different measurements in our experiment, as can be seen at the few percent level. We see an agreement between our data and the values obtained using the ELSA sensitivity values at the 3.6% level in average. From this table we see the errors are compatible with our previous experiment at the 20% level, well below the 50% incertainty of the

α in (10^-4) PSL/keV	Our results	Boutoux, Rabhi et al.
α_{MS}	5.0 ± 1.1	6.8 ± 1.3
α_{SR}	1.9 ± 1.3	2.2 ± 0.5
α_{TR}	3.5 ± 0.8	4.7 ± 0.9

Table 2.9: Sensitivities extracted from the data of LOA experiment (second column) and of the ELSA experiment (third column) using Bonnet et al. model.

ELYSE calibration.

Type	α (ELSA)*Edep (GEANT4) (10^{-2} PSL)	Mean (PSL/e-) (10^{-2})	RMS
MS	2.7± 0.54	2.1 ± 0.45	4%
SR	0.7± 0.13	0.6 ± 0.15	4%
TR	0.5± 0.1	0.4 ± 0.07	2.6%

Table 2.10: Comparison between this work and estimates using IP sensitivities obtained by our work at ELSA.

2.2.5 Influence of tungsten behind and in front of the Imaging Plates

We performed IP response measurements with tungsten plates positioned behind the IP. As done for the ELSA data, we define Q(I) as the ratio between the response function of an IP(I) in the stack and the signal of a single IP of the same type:

$$\mathrm{Q(I) = R(IP(I))/R(IP(0))} \tag{2.12}$$

I is the index of the experimental configuration. The error on Q(I) is only driven by the relative error on the readout of the IP responses and on the difference of fading times between the measurement of the simple IP of reference and the measurement of the IP in the stack. It is particular independent from the absolute calibration of the reference detector. We have taken this error 5%, corresponding to the fading uncertainty.

In Fig. 2.26, we can observe that the signal of the MS IP increases by 30% when 1 mm of tungsten is added for 70 ± 5 MeV electrons. The response is constant when more tungsten is added. This result confirms our work at ELSA [46]. We conclude therefore, that 1 mm of tungsten will be sufficient for the detectors of the PETAL+ – SESAME and SEPAGE to have the signal on IPs independent of the material close behind them.

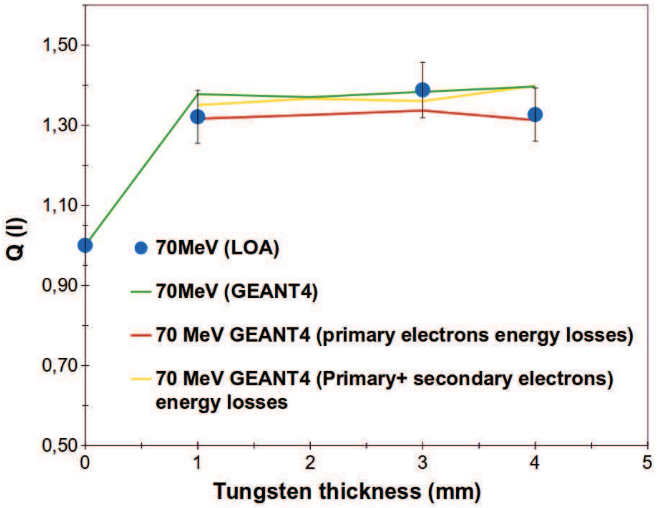

Figure 2.26: Effect of tungsten behind the IP with electron 70 MeV.

A stack shown in Fig. 2.27 was used in order to test the effect of tungsten shielding between and in front of the IP. This stack is composed of five MS IP and three tungsten plates of 1 mm thickness each.

The evolution of Q(I) with the electron energy is shown in Fig. 2.28, for $I = 1, \ldots, 5$. We notice that for all I and electron energies we have is Q(I)>1. Hence, the signal of the IPs in the stack is larger than the signal of a single IP. Moreover, this additional signal can be up to 100% of the single IP response.

Simulations were used to determine the physical origin of the increase of signal on the IP. We see from Fig. 2.29 the additional amount of signal in the IP for 100 ± 5 MeV electrons. The three curves of Fig. 2.29 depict the contributions to the electron energy loss defined above. The orange curve is higher by 50-80% than the blue curve, which means that the additional amount of the signal comes from the interaction of secondary photons with the IP active layer which produce photons

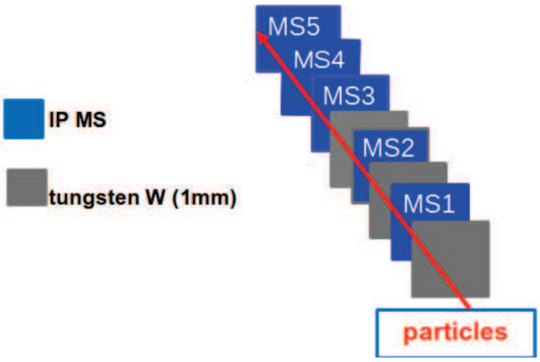

Figure 2.27: The configuration of stack that was used in the LOA experiment to study the influence of tungsten in front of and behind IPs (see text).

that increase the amount of signal. We underline here that because of the relatively constant behavior of Q(I), for a given I as a function of the electron energy, we have compared our data point with simulations computed with electrons with a single value of their kinetic energy, namely 100 MeV for Fig. 2.29.

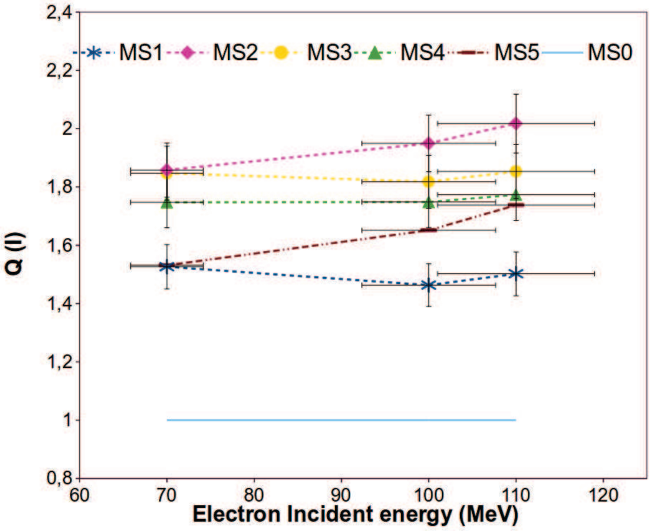

Figure 2.28: The ratio Q(I) for three electron energies (70, 100 and 110 MeV). The dashed lines are guidelines.

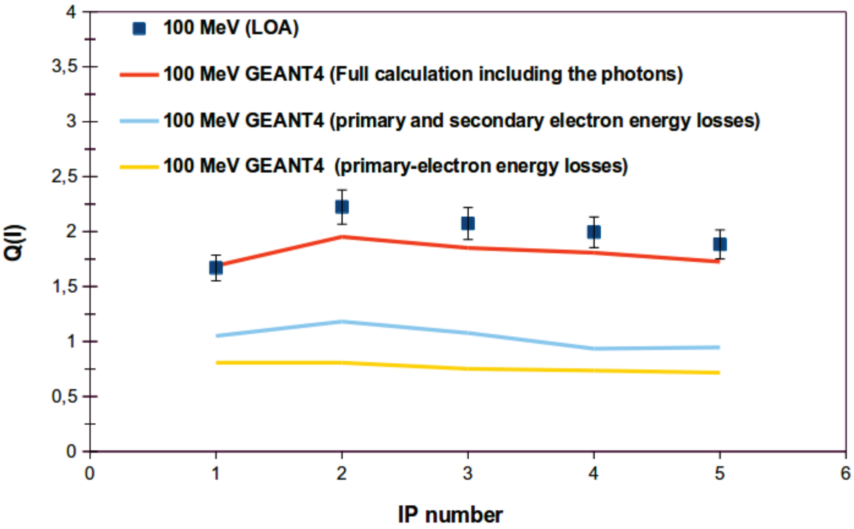

Figure 2.29: The ratio of Q(I) (see text) with respect to the IP index in the stack of Fig. 2.28. The solid lines show the calculation from GEANT4 simulation.

2.3 Summary of Chapter 2

Measurements from 5 to 180 MeV with electrons of IP response functions were performed.

1) Response functions of single IPs were interpreted in the energy range from 5 to 180 MeV using two models for the relationship between the response function of the IP and the average energy loss for electrons, as computed with GEANT4 in the active layers of the IPs. Both models are essentially equivalent in this energy range for electrons.

The ratios between the measured responses and the computed average energy losses provided with sensitivities, which we extracted for our two experiments independently and which provided to be in agreement, despite the differences in the energy range and in experimental methods. Using these determined sensitivities permitted us to compute the IP responses to electrons in the range 0.1 to 1000 MeV, in agreement with the existing data.

2) We have characterized the responses of IPs installed inside stacks where they alternate with layers of tungsten. The measurements and the analysis done with our simulation show that these responses are well explained, and therefore, that shielding of the IPs in the PETAL charged particle diagnostics can be foreseen which will keep the possibility to extract absolute particle spectra at the 20% level of error. The shielding material to be used for protecting IPs from the high-energy photons will not decrease the detection efficiency but rather increase it, whether it is placed in front of the IPs or behind them with respect to the electron trajectories. 1 mm of tungsten is sufficient to obtain IP responses independent from the material placed behind it with respect to the electron trajectories. We also observe that tungsten in front of the IP provides a larger increase of the IP sensitivity than tungsten installed behind. This will improve the efficiency to our detectors, which is important especially during, for example, the PETAL laser energy ramp up at the beginning of operations.

These results are well explained with our GEANT4 simulation. Therefore, GEANT4 seems to be well qualified to design passive detectors for Petawatt laser accelerated charge particles. In particular, we will use it to design our electron detectors for PETAL+ and to interpret future experiments.

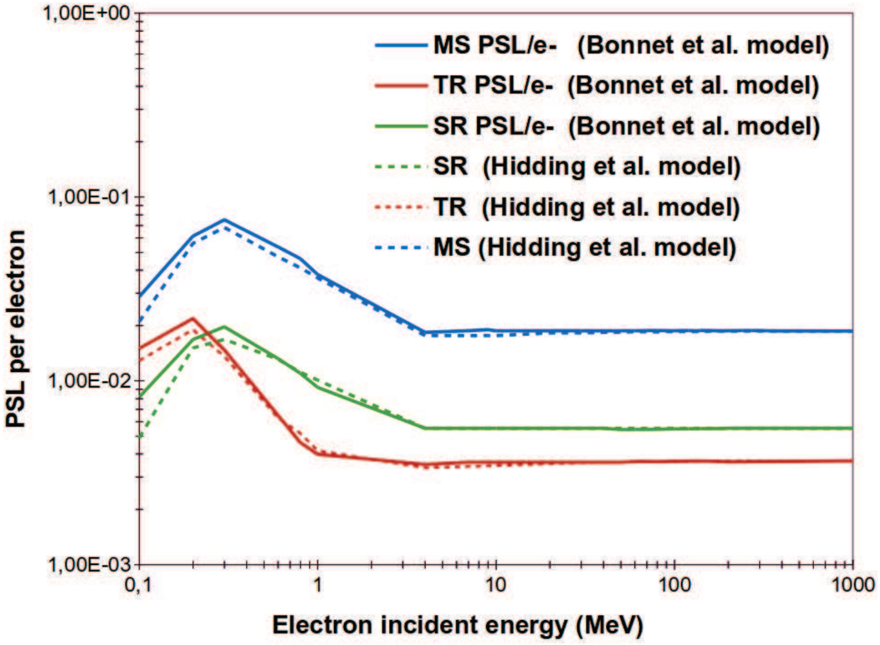

Figure 2.30: GEANT4 simulation for electron between 0.1-1000 MeV, using the IP sensitivities determined with LOA data.

Chapter 3

Response functions of imaging plates to 80 - 200 MeV protons

3.1 Introduction

Calibration data for high-energy protons were scarce at the time these studies were started. IP response measurements of MS, SR and TR IP were described in the literature [23, 24, 76]. Mancic et al. [76] determined the response of TR IP in the energy range [0.5-20 MeV] using laser accelerated protons. Choi et al. [23] measured the response function for TR IP for [0.4-1.6 MeV]. Freeman et al. measured the response function of TR IP between 0.6 and 3.4 MeV using a linear accelerator at SUNY Geneseo 1.7 MV tandem Pelletron accelerator. Bonnet et al. [42] [64] measured the response functions of three types of IPs (MS, SR and TR) at 0.9, 2.2, 2.9, and 3.2 MeV at the AIFIRA accelerator (see Fig. 1.13). As shown in Fig. 1.13, there are differences of one order of magnitude between Choi et al. data and the other data sets. Choi et al. explained this difference by the use of different scanner models which could change the response of the IP. Since we need data for IP responses on the range of energy of protons corresponding to PETAL acceleration, from 0.1 to 200 MeV we performed experiments to complete the existing literature.

An experiment using the proton accelerator at the Centre de Protonthérapie d'Orsay (CPO), France, was done to extend the study of calibration of MS, SR and TR IP for high-energy protons, to measure the response functions of IPs and stacks of IPs and filters. This is the scope of the present chapter. We completed these data with a measurement at the TANDEM of Orsay between 1 and 22 MeV. This is described in the following chapter.

3.2 Experimental setup

The experiment for IP calibration for protons was performed at the Centre de Protonthérapie d'Orsay (CPO). The proton beam is delivered by a synchrocyclotron accelerator. The energy of the protons generated by this system is 200 MeV. Using a graphite degrader, the energy can be lowered down to 73 MeV. The extracted current is 300 nA and the proton bunches are separated by 10-20 ns. With the help of a collimator made specifically for our experiment, we used a proton beam with a square of 3×3 cm. The IPs of 5×5 cm were placed at a distance of 5.5 cm from the beam exit (see Fig. 3.1).

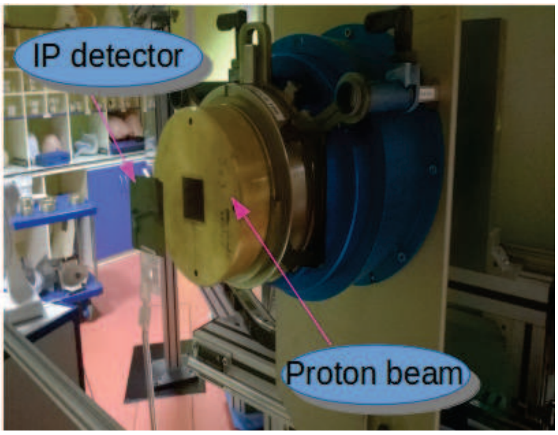

Figure 3.1: The experimental setup.

3.3 Data acquisition

The PSL values were extracted for each type of IP, and the fading correction is included. The energies of protons used to calibrate BAS-MS, BAS-SR and BAS-TR

IP are 80, 120, 160 and 200 MeV. The Wratten filter used in the ELSA experiment and provided by J-P.Nègre [26] was installed in our scanner in order to avoid the saturation of the IP signal readout. The PSL signal was selected over the area defined by the yellow dashed square as shown in Fig. 3.2.

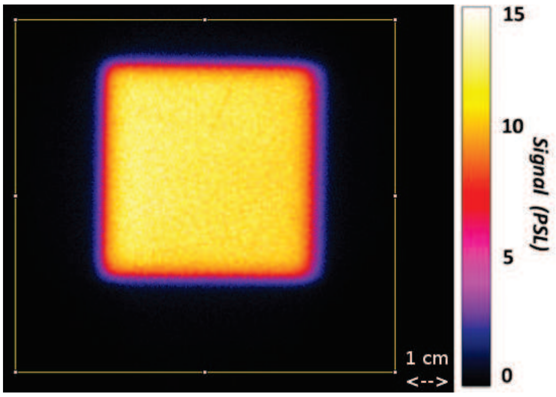

Figure 3.2: The signal detected in the IP.

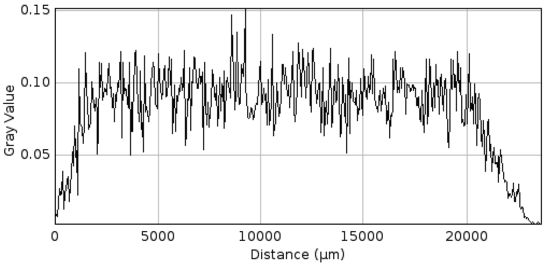

Figure 3.3: The PSL values as a function of the distance of a horizontal profile of the IP.

We performed the experiment in two steps. The first set of data was taken in July 2015 and the second set in February 2016. In the first experiment we measured systematically each type of IP along with composite detectors. In the second experiment we only used two energies (80 and 160 MeV) with a limited number of measurements.

The reason for the second measurement can be explained as follows. At the beginning of this first experiment, we made two measurements at low and nominal beam intensities to check the Wratten filter transmission. This experiment let us think we had the expected value, roughly 1/450 as given above (ELSA experiment). After the experiment, the whole analysis (as will be detailed below extracting response functions and sensitivities), using the obtained sensitivities along with our GEANT4 simulation of interaction of IP with protons was done. The response functions were computed, as for electrons, in the energy range from 80 to 200 MeV. The curves obtained in the energy range of the measurement of Bonnet et al. [42] were more than one order of magnitude different from the measured responses for the three types of IPs (MS, SR and TR) coherentely. Seeing this discrepancy it seemed to us that we may have had a normalization problem in our data set. This could be a reasonable hypothesis since we made only one measurement at low intensity in order to determine Wratten filter transmission. Hence, we decided to do another measurement, performed in February 2016 to check with a few data points this normalization issue. During this second experiment we did three determinations of the Wratten filter transmission. The three of them were at the level of 10% in agreement with what we determined at ELSA. Moreover, the extracted sensitivities from the measured IPs during the second experiment, in combination with GEANT4 simulation, IP responses were in agreement with those measured by Bonnet et al. [42]. In addition to this, we computed that the ratios of the IP responses in July 2015 and February 2016 exhibited a constant filter value of 21 (with 10% accuracy). Therefore, we decided to apply this normalization factor to all our data of July 2015. It seems like we have had a problem in the data acquisition of July 2015 which prevented us from measuring the real number of protons which were sent onto our detectors. This is still unexplained.

In February as a first check we measured the linearity of our measured response with the beam intensity. The result is shown in Fig. 3.4. We fitted the relationship with a linear function. As shown in this figure, the linear fit is extremely good. We did the entire experiment with 20 beam pulses for each IP radiation.

3.3.1 Experimental results of IP response functions

Fig. 3.5 shows the responses of single IPs as a function of the proton beam energies. There are three sources of errors in these measurements:

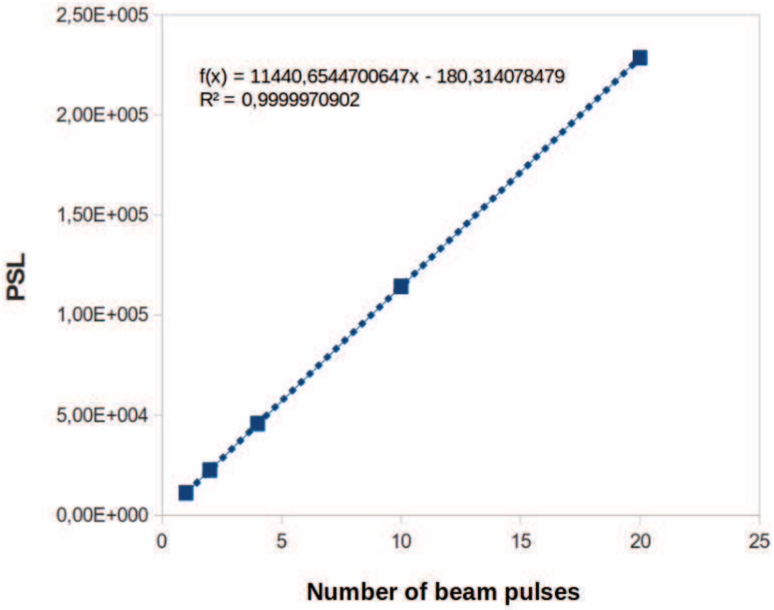

Figure 3.4: Linearity of the response of the experiment of February.

- 5% in the beam charge measurement
- 2% in the fading correction
- 2% in the Wratten filter transmission

This is quadratic total of 6%.

3.4 IP sensitivities

We computed the IP sensitivities α (PSL/keV), i.e. the relationship between the average IP response and the average proton energy loss computed wih GEANT4 using the two models described in the introduction. Fig. 3.6 shows the stopping power profile of 80 MeV protons in the active layer of an IP MS. This profile is flat because the total energy loss of these protons in the IP is small with respect to their kinetic energy. This means that for this experiment, both models of Hidding et al. and Bonnet et al. are equivalent (see Appendix B).

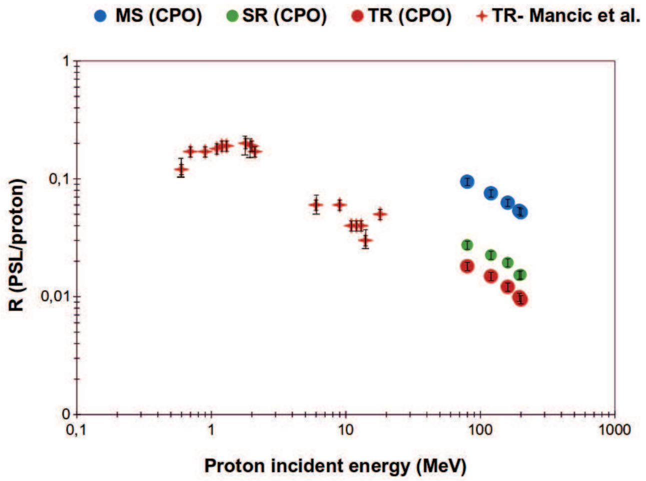

Figure 3.5: The response function R(E) in PSL/proton of MS, SR and TR measured at CPO for proton energy [80-200 MeV]. Our data are compared to those of Mancic et al. [76].

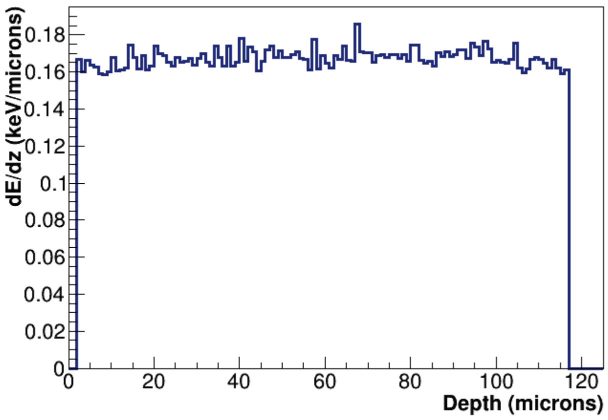

Figure 3.6: The mean deposited energy by protons of 80 MeV in function of the depth in the MS IP. The mean deposited energy is calculated using 10000 of incident particles.

The sensitivities obtained from our measured response functions, using the model of T. Bonnet et al. are given in (Tab. 3.1) and compared to those of [42]. Note that we used to compute them the attenuation lengths fitted by T. Bonnet et al.

The good agreement between our sensitivities and those of [42], within the error bars, must be underlined since they were determined:

- At rather different kinetic energies with very different energy-loss profiles

- Using two different experimental methods, individual proton counting in a reference detector in [42], direct irradiation with beam current measurement in our case.

Such an agreement is a strong point for the calibration of our detectors on the whole range of proton kinetic energies covered by the diagnostics of PETAL. These sensitivities seem applicable in this entire range, i.e. in particular in the energy range between both data sets.

Using GEANT4 and T. Bonnet et al. model, we have computed the MS, SR and TR-IP responses to protons in the energy range between 0.1 and 1000 MeV (see Fig. 3.7).

	α in (10^{-4}) PSL/keV	Bonnet et al.
α_{MS}	4.9 ± 1.5	3.03 ± 0.07
α_{SR}	1.82 ± 0.4	1.44 ± 0.05
α_{TR}	1.32 ± 0.2	1.55 ± 0.12

Table 3.1: sensitivities for each type of IP using Bonnet et al. model [29].

The results of these two models are compared with the literature in Fig. 3.7. Mancic et al. [76] and Choi et al. [23] used protons accelerated by laser that are continuously distributed in energy. To measure the responses of IPs, the proton numbers used by Choi et al. are obtained by Thomson parabola and the scanner they used is Fuji BAS-5000. For Mancic et al., the proton numbers were obtained by a radiochromic films (RCF) and a magnetic spectrometer associated to IPs detector and CR39 detectors. The scanner that they used was Fuji BAS-1800II.

The data of Choi et al. are higher than the other data and higher than the curve computed with GEANT4 using our IP sensitivities. Our GEANT4 simulations and our IP sensitivities are in a good agreement with the data of Bonnet et al. [42]. For the proton energy around 10 MeV, the difference between the measurement of Mancic et al. [76] and our experiment is at the 30% level.

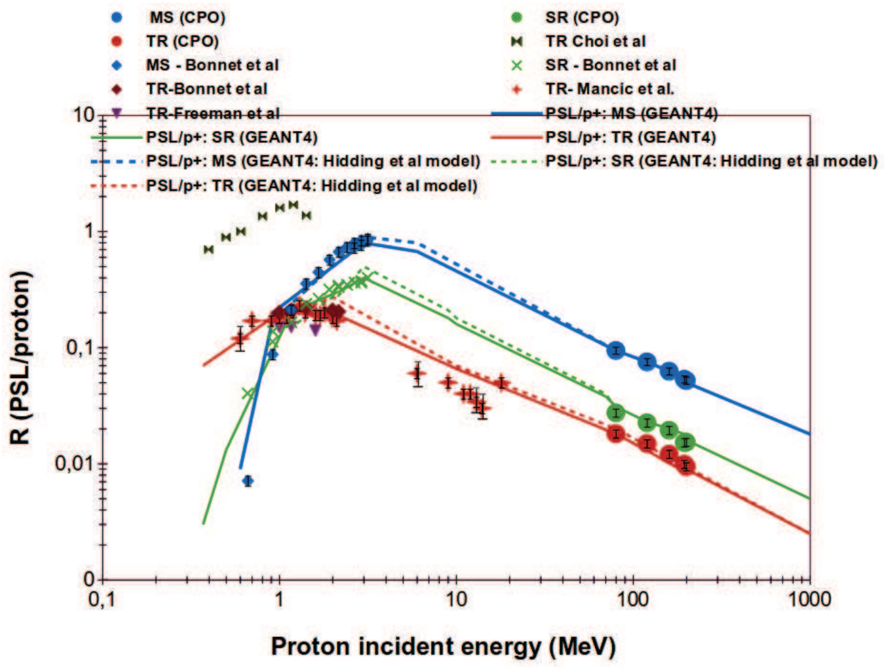

Figure 3.7: The response function R(E) of MS, SR and TR measured at CPO for proton energy [80-200 MeV] using Hidding et al. model (dashed lines) and Bonnet et al. model (full lines) and the comparison with the literature.

3.5 Sensitivity measurement for a multidetector MS-ND-TR-MP-SR and a single IP

As was done with electrons during ELSA experiment, a measurement with a multidetector IP was performed. A single IP MS was used as reference to determine the relative sensitivities of the different IP types. We checked with GEANT4 the energy losses of the active layer of IPs are not influenced by the presence of the others. As mentioned in Chap. 2, this type of measurement allows to keep only the relative error bars of the experiment, getting rid of the charge determination incertainty as well as of the readout absolute calibration.

We can see from Fig. 3.8 that the signals of MS IP are comparable for both detectors. Tab. 3.2 shows the ratio of an IP MS over the stripes detector. We can see from this table the good agreement between the simulation and the experimental data.

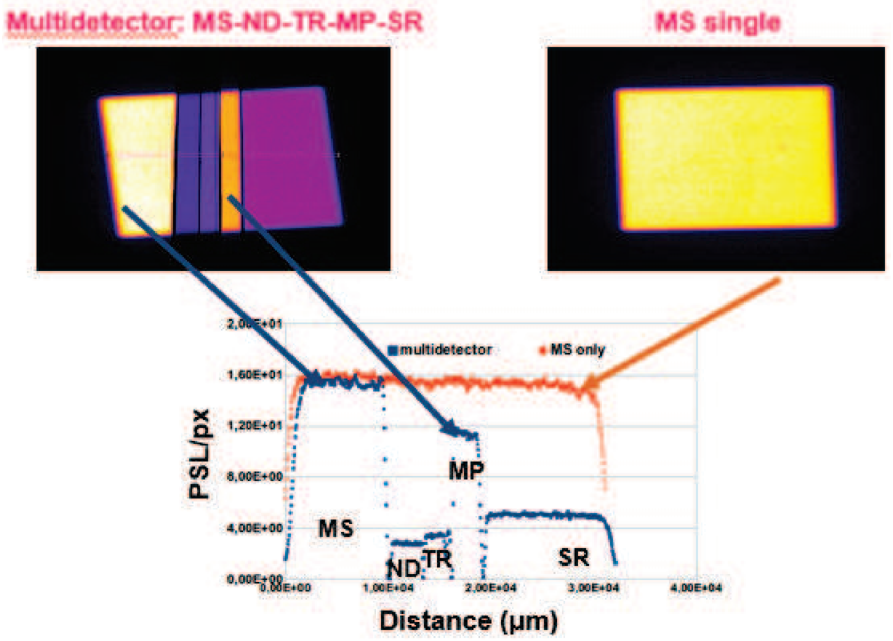

Figure 3.8: The recorded signal detected in the IP and in the multidetector.

E[MeV]		SR/MS	TR/MS	MP/MS	ND/MS
80	relative	0.25±0.09	0.18± 0.05	0.61± 0.04	0.17± 0.03
	simul.	0.26±0.1	0.21±0.06	x	x
100	relative	0.25±0.09	0.18 ± 0.05	0.59± 0.05	0.18± 0.02
	simul.	0.26±0.1	0.21±0.06	x	x
120	relative	0.22 ± 0.08	0.17±0.04	0.57± 0.03	0.17± 0.03
	simul.	0.26 ± 0.1	0.21±0.06	x	x

Table 3.2: Ratios of the measured signal of the stripes over an MS IP.

Note that considered ratios between the simulation results for various IP types in Tab. 3.2 are ratios between the mean energies deposited in the sensitive layer as calculated by GEANT4 and the sensitivities.

3.6 Imaging plate responses with tungsten layers

Figs. 3.9 and 3.10 show the response of MS IP with tungsten of different thicknesses behind the detector when 80 MeV protons are used. It can be seen from these figures that the response to protons is constant, which is not the case of the electron data. This test is important to understand how 5 mm of tungsten behind the detectors in SEPAGE will affect the detected signal. The conclusion is that the signal of protons does not significantly differ because of this tungsten layer.

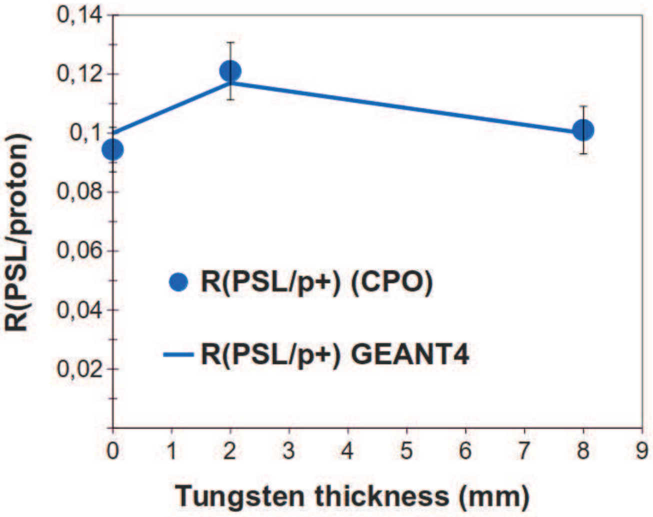

Figure 3.9: The influence of tungsten behind the MS IP.

3.7 Response function of IP stacks

In this section, the influence of the layers of high-Z materials on the response of IP to protons is studied. The experimental data and the simulation are compared.

A stack composed of 2 SR IPs in front, 11 MS IP and filters of lead and tungsten was used with protons of 200 MeV (see Fig. 3.11). Between each pair of the first five IPs, a thickness of 10.4 mm was installed. Plates of tungsten with smaller thicknesses, between 0.1 and 1 mm, was put between each pair of the remaining IPs in the stack. The purpose of this stack was to find the deposited

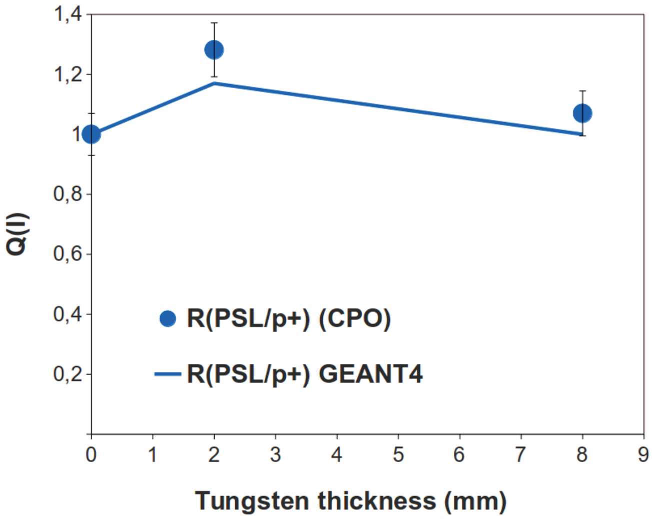

Figure 3.10: The plot of Q(I) (see text) with respect to the tungsten thickness and the comparison with the tungsten thickness.

energy distribution in the IPs for high-energy loss of the protons. The thick layers of lead were intended to slow down protons to the Bragg peak.

Fig. 3.12 and 3.13 show that we have sampled in this composite detectors, the full energy loss of 160 and 200 MeV protons, on the principle of hadronic calorimeter technique used in high energy physics (nucleon or particle physics). This means in particular that all the protons impinging on these detectors were fully stopped inside. Such detector are hence, in the principle, a test bench of the IP response functions over the whole range from 200 down to 0 MeV. Therefore, the comparison with the GEANT4 simulation provides a strong test bench of the models linking the IP responses to the average energy losses.

3.8 GEANT4 simulation

As we did for the electron measurement, the quantity Q (I) was used in order to compare our simulations with our data:

For the experiment:

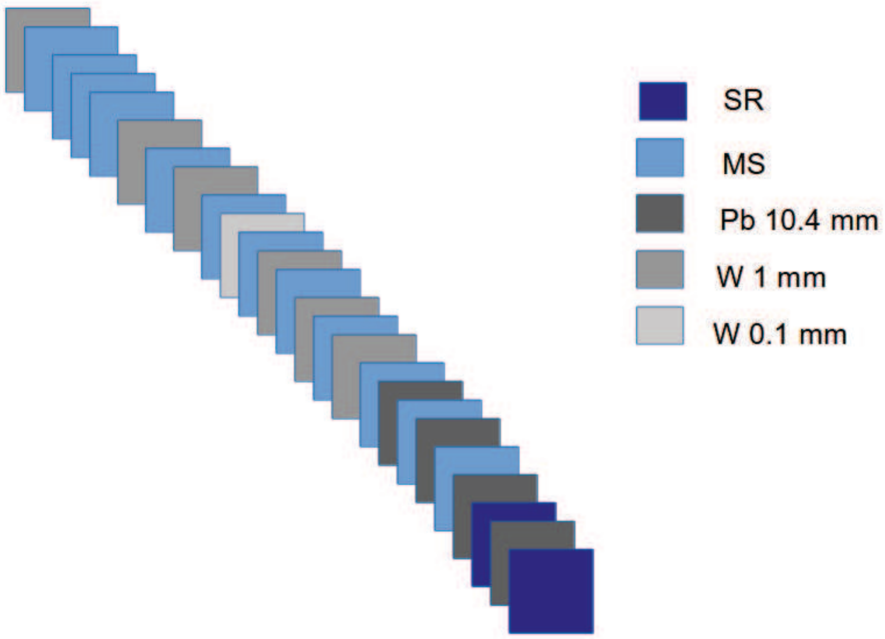

Figure 3.11: The stack used in CPO experiment using 200 MeV protons.

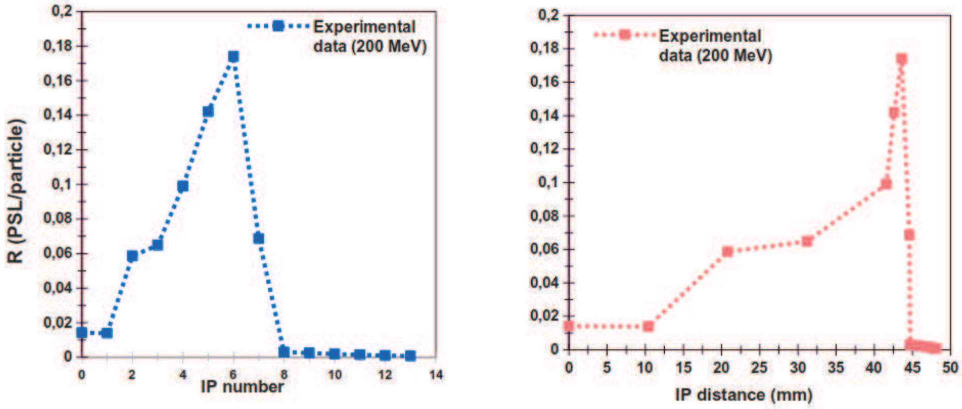

Figure 3.12: The signal from the stack for 200 MeV protons as a function of the IP index (left) and the distance of the IP from the first one (right).

$$Q(I) = \frac{R(MS(I))}{R(MS(0))} \tag{3.1}$$

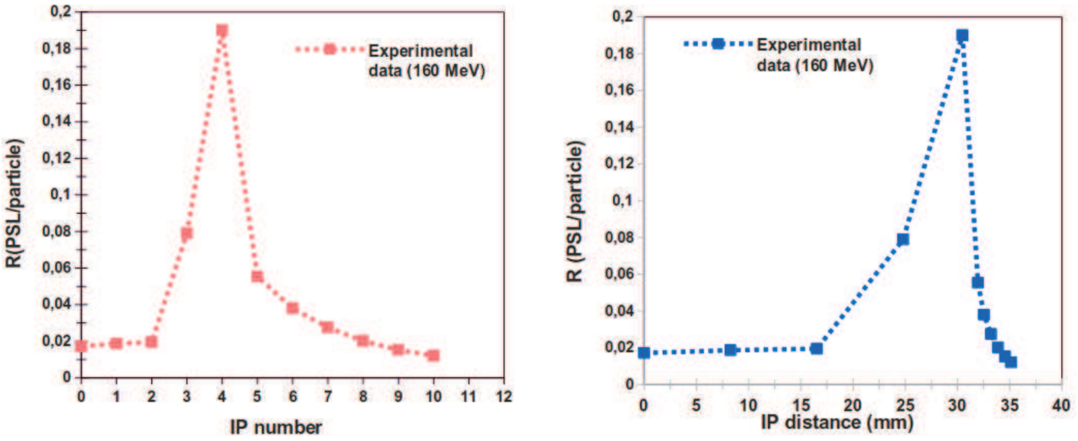

Figure 3.13: The signal from the stack for 160 MeV protons as a function of the IP index (left) and the IP distance from the first one (right).

For GEANT4 simulations:

$$Q(I) = \frac{\text{Edep}(\text{MS}(I))}{\text{Edep}(\text{MS}(0))} \tag{3.2}$$

Fig. 3.14 shows that for protons of 160 and 200 MeV the origin of signal comes directly from the incident proton (without intermediate secondary particles). The three curves overlap entirely, which means that all signal is created by primary particles only.

As shown in Fig. 3.14, the protons are absorbed along their path through the detector. Protons of higher energy propagated through all IPs and deposited their energy in each of them until the last IP where they lose 0.021 MeV of their energy for the stack of 160 MeV protons. In the first IP SR the deposited energy is about 0.107 MeV. The same conclusion is valid for the stack used for the energy of 200 MeV, where the deposited energy in the first IP is 0.091 MeV and in the last IP is 0.32 MeV.

We observe a really good agreement between our data points and our calculations, using single IP sensitivities. In itself, such a measurement validates the value of the RMS sensitivity on the whole range of proton energy for the PETAL diagnostics.

3.9 Summary of Chapter 3

- Measurement from 80 to 200 MeV with protons of IP response functions was done.

- Response functions of single IP were interpretated in the wide range of energy using two models for the relationship between the response function of the IP, and the average energy loss for protons, as computed with GEANT4 with the active layers of the IPs. Both models are essentialy equivalent in this energy range for protons. The obtained results were compared with the Monte Carlo simulations in GEANT4 with the focus on providing a complete set of information about response functions of MS, SR and TR IP to protons from 0.1 MeV to 1 GeV, which is the energy range relevant to the PETAL operation. A simple coefficient determined from the data quantifies this relationship, giving the purpose to the model and the possibility to use our simulation for the design of the PETAL+ diagnostic detector, to be installed for the first shots.

- We have characterized the responses of IPs installed inside stacks where they alternate with layers of tungsten and lead. The measurement and the analysis done using our simulation show that these responses are well explained and thus, that sufficient shielding of the IPs in the PETAL charged particle diagnostics can be prepared which will keep the possibility to extract absolute particle spectra at the 7% level of error. The shielding material to be used for protecting IPs from the high-energy photons will not decrease the detection efficiency but rather increase it with respect to the proton trajectories.

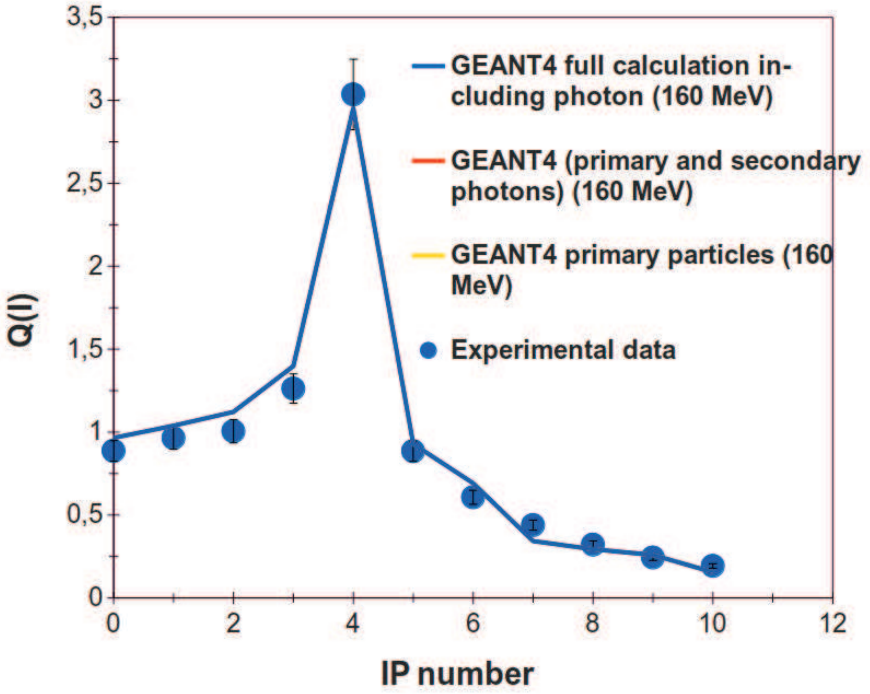

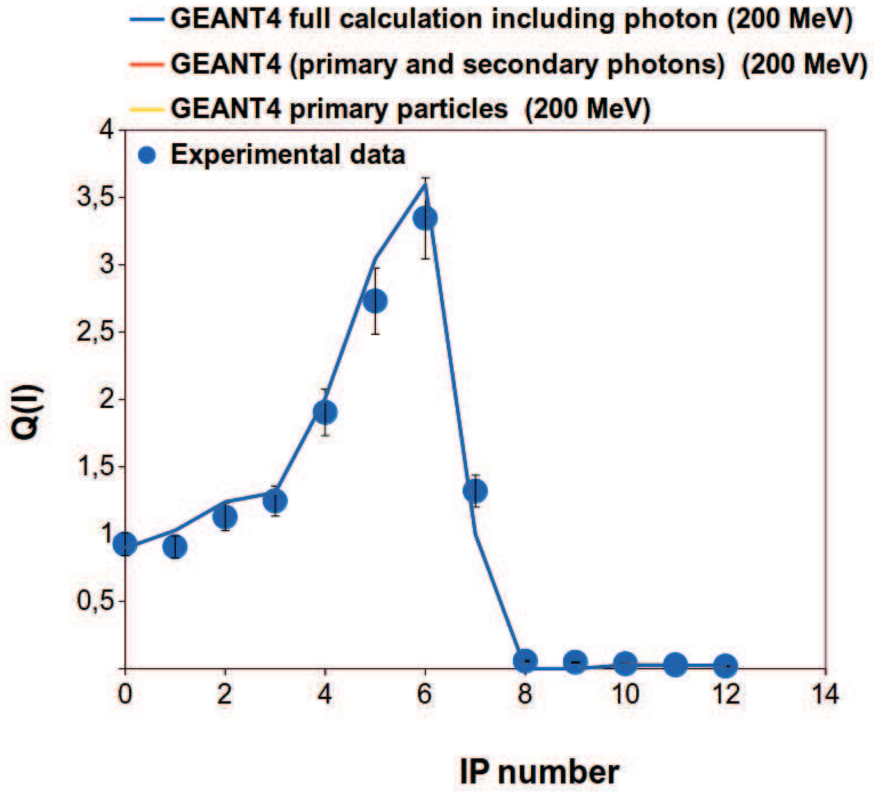

Figure 3.14: The GEANT4 simulations for the stacks using protons of 160 and 200 MeV.

Chapter 4

Calibration of the particle transport and detectors of the low-energy Thomson parabola of the PETAL+/SEPAGE diagnostic

The aim of the experiment performed at the Tandem accelerator of Orsay in February 2016 was:

- The calibration of IP to protons between 1 and 22 MeV,

- The calibration of the electrostatic and magnetic transport of protons and ions in the Thomson parabola of the low-energy channel of the SEPAGE diagnostics PTBE ”Parabole Thomson Basse Energie” (see Appendix.A).

4.1 Experimental geometries

In the Tandem experiment we connected a chamber of 800 mm diameter and 222 mm height to the exit of the beam. In this chamber, a support containing the targets and a Faraday cup was installed. A demonstrator of the “low-energy channel“ Thomson Parabola for SEPAGE was tested during the experiment. This demonstrator was composed of a front collimator, Thomson Parabola and a Micro-Channel Plate (MCP) to detect the particles that passed through the electric and magnetic fields.

The geometry of the experiment was changed during the experiment because no signal was detected in the MCP when the beam was scattered at the angle of 30°. This could not be anticipated because the MCP detection efficiency was totally unknown to us. It was thus necessary to install the Thomson parabola at 0° with respect to the incident beam to increase the particle flux on the detector and perfom the transport calibration.

The first geometry shown in Fig. 4.1 was based on Rutherford scattering. A semi-conductor detector was used as a reference to count the number of scattered protons per incident beam particle.

The Thomson Parabola was placed at 30° with respect to the incoming beam direction. This angle was chosen because it was the only one offering two windows in the target chamber on both sides of the beam. We took advantage of the second window at the same angle to install the reference detector to count the number of particles entering the Thomson Parabola (see below). This detector will be described in the next section.

In this geometry we used only the proton beam, with an energy from 1 to 22 MeV.

The beam was directed onto three types of target:

- 100 μm tungsten
- 1 μm tantalum
- 0.8 μm aluminum

In the second geometry, the PTBE was installed at 0° with respect to the beam direction in order to provide enough particles to the detector. In this geometry, the targets were used to:

- Scatter the incoming beam in order to reduce sufficiently the beam intensity on the PTBE detector. The beam intensity could not be changed in the accelerator by more than roughly a factor 10 with respect to the nominal value.

- Produce average energy losses in order to scan the energy spectrum of the PTBE to test the electric and magnetic transport.

The PTBE is composed of a dipole magnet of 0.05 T and electrodes of $\pm$ 12.5 kV (see Fig. 4.2), parallel to each other, generating an electric field parallel to the magnetic field. The length of the electrodes is 40 mm and that of the magnet is 104 mm. The collimator was placed at the entrance of the spectrometer in order to obtain a point-like and monodirectional source before the analysis provided by the electric and magnetic fields.

An MCP and a CCD camera were installed at the bottom of the chamber containing the Thomson Parabola (TP) to detect the proton and ion spot on the MCP (see Fig. 4.1).

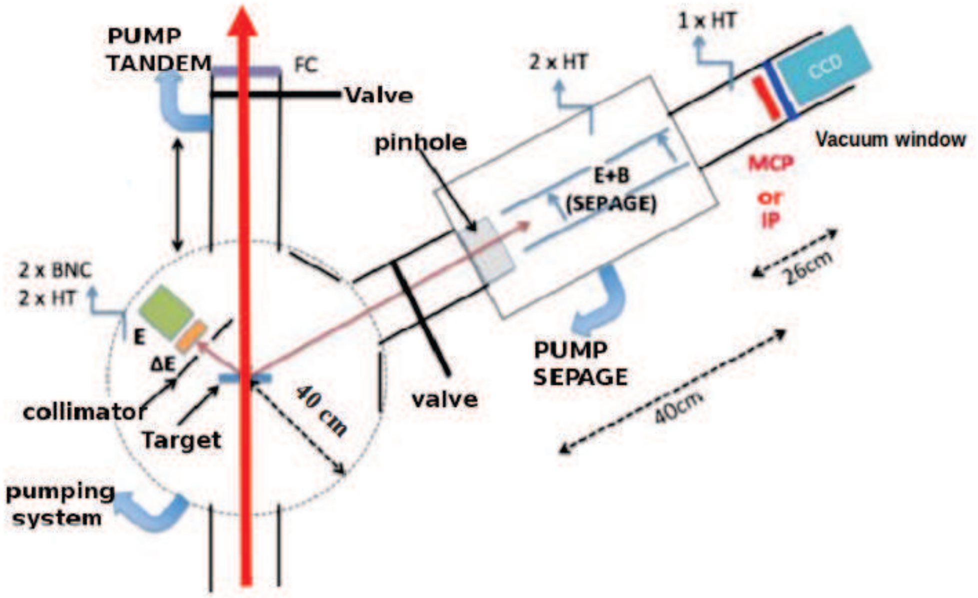

Figure 4.1: The experimental setup [81].The E ΔE detectors and the axis of the Thomson Parabola are at the same angle (30°) with respect to the incoming beam direction.

4.2 The semi-conductor detector and the data acquisition

The detector laboratory of the Institute de physique nucleaire (IPN) of Orsay built especially for our experiment a semi−conductor telescope composed of two detectors:

1/ A detector called "ΔE" of pure silicon, 200 μm thick to let heavy ions (C, O)

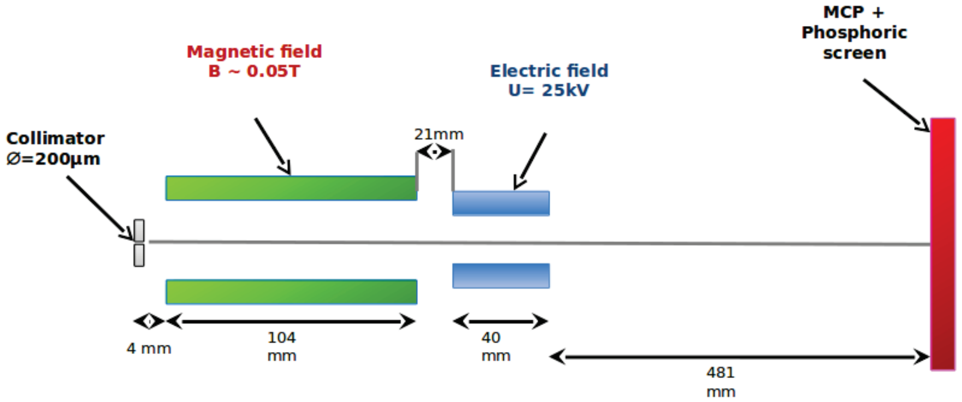

Figure 4.2: SEPAGE low-energy Thomson Parabola.

at the highest energies available at ALTO/TANDEM pass through. (84 MeV for $^{12}C^{6+}$ ions)
2/ A detector called "E" of silicon lithium of 3 mm thick, to stop the ions and protons. Protons up to 22 MeV (The maximum energy used in our experiment) are stopped inside this detector.

The principle of such a detector works as follows. When an ionizing particle goes through a semi-conductor as Si, it creates electron−hole pairs proportionally to the energy it loses inside. The advantage of Si is that the average electron−hole pair creation potential is rather low, around 4 eV, as compared to those of, e.g. gases used in nuclear physics detectors wich are at the level of 20 to 30 eV. This means in particular that the statistics of electron−hole pairs is rather high in Si (or SiLi). Biasing the Si or SiLi detectors with a potential permits to collect the electrons of the conduction band. The electron charge collected is then amplified in a charge preamplifier and put in shape with the time constant of the preamplifier. Subsequently, this signal is once more amplified by an amplifier, shaped and coded. The information collected for each event is therefore proportional to:
- The energy lost by the particle inside the ΔE detector;
- The energy lost inside the E detector, which is for our experiment, the total remaining kinetic energy of the particle downstream of the ΔE layer.

The combination of both pieces of information permits the identification of the particle which was selected.

Note that the signal coming from the ΔE detector is splitted after the preamplifier. One part goes to the amplifier level and the coding, the other part is being sent to a fast amplifier, whose output signal is compared with a level in a constant fraction descriminator (CFD in Fig. 4.3), to provide the trigger of the data acquisition.

The data acquisition of this detector during our experiment was based on the GANIL (Grand Accélérateur National d'ions lourds, Caen, France) [78] framework. During the experiment, we kept the repetition rate below 100 events per second to ensure the dead time of the data acquisition was negligible.

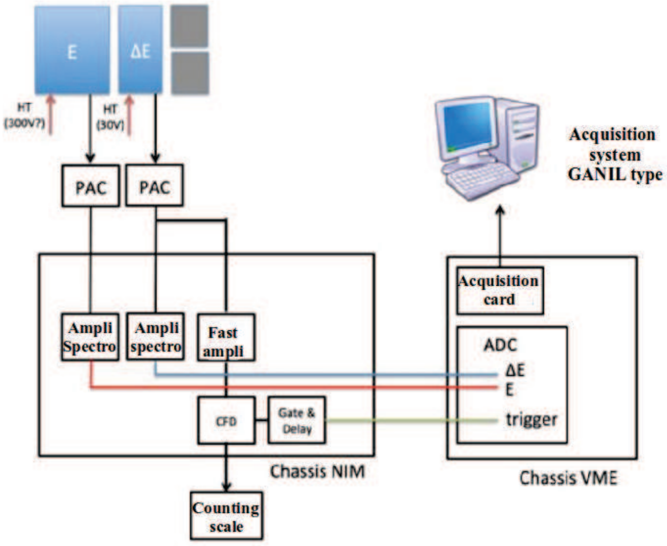

Figure 4.3: The schematic of the $\Delta E - E$ with the electronic and the acquisition system.

4.3 Rutherford scattering

The formula to calculate the number of protons that enter the TP:

$$\frac{\mathrm{N}}{\mathrm{N}_0} = \mathrm{nL}\frac{\mathrm{d}\sigma}{\mathrm{d}\Omega}\Delta\Omega \tag{4.1}$$

- N: number of particles detected by the detector
- N_0: number of incident particles hitting the target
- n: atomic density (cm^{-3})
- L: thickness of the target (cm)
- $\frac{\mathrm{d}\sigma}{\mathrm{d}\Omega}$: Rutherford cross section (cm^2)
- $\Delta\Omega$: solid angle

Rutherford cross section [80]:

$$\frac{\mathrm{d}\sigma}{\mathrm{d}\Omega} = \left(\frac{\mathrm{Z}\mathrm{Z}_\mathrm{A}\mathrm{e}^2}{16\pi\varepsilon_0\mathrm{E}}\right)^2 \frac{1}{\sin^4\frac{\theta}{2}} \tag{4.2}$$

- Z : atomic number of the particle (proton Z = 1)
- Z_A: atomic number of the target
- e: elementary charge ($1.602.10^{-19}$ C)
- E: particle energy
- θ: scattering angle from the beam axis

Solid angle:

$$\Delta\Omega = \frac{\Delta \mathrm{S}}{\mathrm{R}^2} \tag{4.3}$$

- ΔS area of the collimator
- R distance from the target to the collimator

Atomic density

$$\mathrm{n} = \frac{\rho.\mathrm{N_A}}{\mathrm{M_n}} \tag{4.4}$$

- ρ mass density of the target in g.cm^{-3}
- $\mathrm{M_n}$ atomic mass in g.mol^{-1}
- $\mathrm{N_A}$ Avogadro constant in mol^{-1}

Using the equations of this section and $\theta = 30°$ with the distance between the target and the collimator of 70 cm, with a beam of 1 μA on the tungsten target of 100 μm and protons 20 MeV, we obtained 8 protons per second entering the collimator. Using the tantalum target and 5 MeV protons, we had 125 protons per second. The kinematics of Rutherford scattering is given in Appendix C.

4.3.1 Scattered proton identification

For each measurement we collected data with the ΔE-E telescope. The identification of Rutherford scattered protons was performed using 2D histograms such as shown in Fig. 4.4. In this figure we only selected the proton spot to calculate the IP responses.

4.4 Responses of Imaging Plates

The IP responses were measured for each type of Imaging Plates in the energy range available at the Tandem. The energies of the protons that enter the TP used to calibrate BAS-MS, BAS-SR and BAS-TR IP are 1.53, 5.6, 11.5 and 19.3 MeV. They were computed by taking into account the energy losses in the scattering targets both with GEANT4 and with SRIM [72]. The scanner used for the read-out of the signal detected on the IPs was described in the introduction (see section 1.5.1). As an example, the PSL signal of 15 MeV protons was selected over the area defined by the yellow dashed line as shown in Fig. 4.5. The measurements at other proton kinetic values gave similar signal shape.

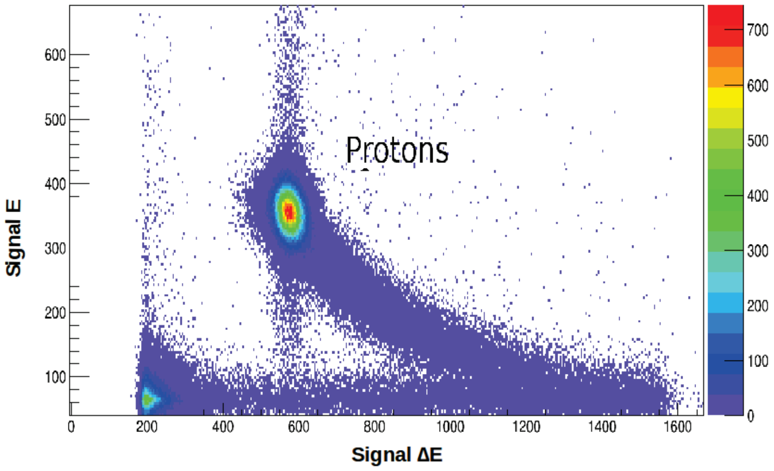

Figure 4.4: 2-D histograms showing the charged-particles in our reference detector. On the x−axis: the coded signal from the ΔE detector; On the y−axis: the coded signal from E detector. Each point corresponds to a particle.

The shape of the detected signal on the IP maybe commented as follows. In Fig. 4.5 the vertical axis corresponds to the electric deviation. Of course, the measurements with IP were done without electrostatic field in the Thomson parabola.

The horizontal axis of Fig. 4.5 is the magnetic dispersion, with the highest momenta on the left and the lowest on the right. Therefore, the signal shape can be decomposed into:

- A central and ovale spot corresponding to the particles which went directly through the pinhole of Thomson Parabola.
- A tail, towards lower momenta, corresponding to particles which partially crossed material inside the pinhole, whose shape and edges are not perfect as was measured with a microscope. The shape of the signal is hence defined by the collimator at the entrance of the detector.

The fading corrections were taken into account. The fading time in our experiment is 20 minutes with few seconds uncertainty.

The results in Fig. 4.6 show the responses of single IPs as function of the proton incident energy. These results at the lower energies are basically in agreement with Bonnet et al. [42] data. We confirm that our measurements disagree with that of Choi et al. [23]. It may be interesting to investigate whether or not this is related

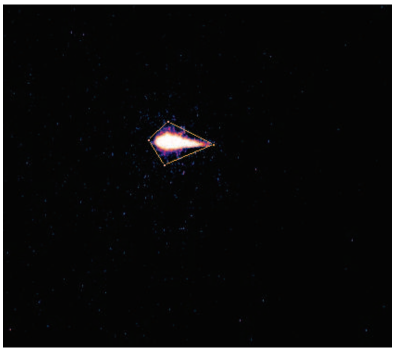

Figure 4.5: The signal detected in the IP for 15 MeV proton.

to the use of different scanners in the readout process of the IP as was suggested by Choi et al. [23]. The error in the number of protons detected on the IP is between 3-5%, including the statistical uncertainty.

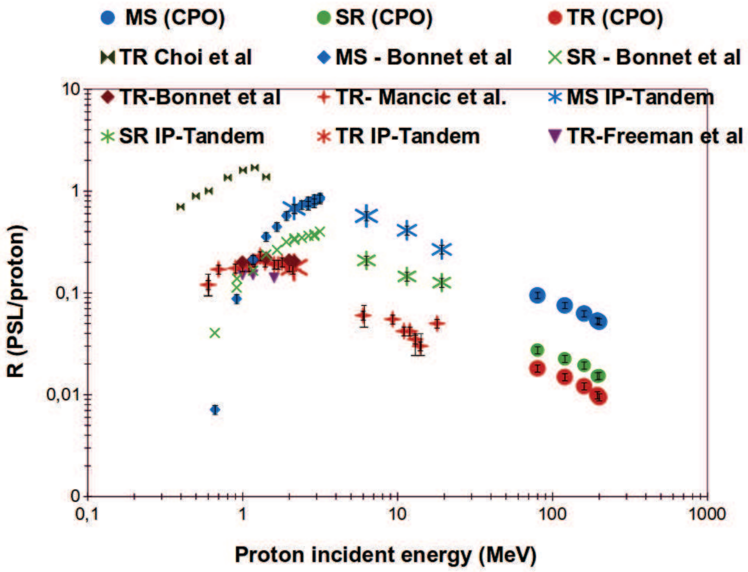

Figure 4.6: The IP responses and comparison with the existing data.

4.4.1 IP sensitivities

As for our experiment with high-energy protons at CPO, the imaging plates sensitivities were extracted from the measured response functions using the model of T.Bonnet et al. [42] [64] and given in Tab. 4.1. We see that these three sets of data agree well within the error bars, confirming therefore an agreement with [42] [64] and, consequently, a disagreement with the data of Choi et al. [23]. We have used these sensitivities to compute the IP responses for protons in the range of energy between 0.1 and 1000 MeV (Fig. 4.7). We confirm the agreement with T. Bonnet et al, the disagreement with Choi et al. data with TR-IP over the whole range of their measurements and in the corresponding energy range, a 30% difference between our calculation and the measurement of Mancic et al. [76] for TR IP around 10 MeV protons.

Both models are close in the energy range above 3 MeV and equivalent above 30 MeV. Below 3 MeV Bonnet et al. model describes the data. In this energy range both models diverge because the term dE_p/dz is dependent on the IP active layer depth. We confirm our measurement with CPO. Around 10 MeV we confirm 30% difference with Mancic et al. [76].

The unicity of the sensitivities, determined for each type of IP for protons over the energy range of our measurement confirm the close relationship between the PSL response of imaging plates and the proton energy losses in the active layer of IP, with a linear coefficient which is constant over the whole PETAL energy range. This gives credence to the models of B. Hidding et al. and of T. Bonnet et al. Moreover, we should stress here that the sensitivities determined for MS and SR are the same for electrons and protons, at least they are comparable within error bars. This is all the more remarkable as we have seen that the contributions to the energy losses of these two types of particles are very differernt when decomposed into primary particle energy losses and secondary and high-order particle energy losses.

In this respect, the difference of sensitivity found for TR-IP between electrons and protons should be underlined and would need additional investigations, beyond the scope of the present work.

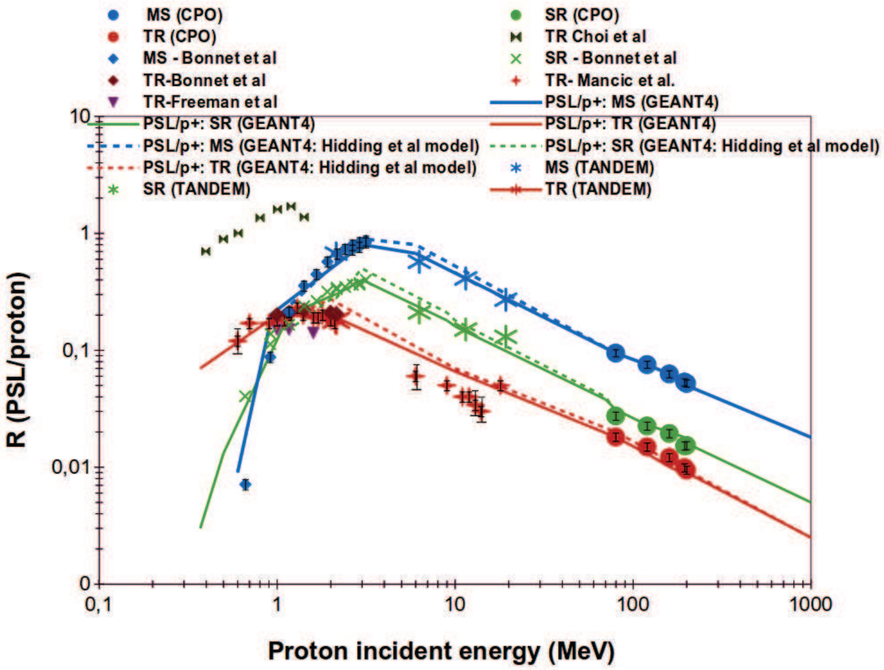

Figure 4.7: Response function of MS, SR, and TR IP and comparison with the literature. The dashed lines are the modeled responses of Hidding et al. [25]. The full lines are the modeled responses using Bonnet et al. [42] model.

4.5 Influence of the incident angle

As mentioned in the introduction, the protons and electrons will impinge on the IP detectors in SESAME and SEPAGE at various angles with respect to the surface normal. Therefore, in order to know the response of the IPs as a function of the angle, we rotated an MS IP for the proton energy of 11.5 MeV up to 75°. Using the setup with the Thomson Parabola made it possible to measure the IP response up to such a large angle with respect to the IP surface normal because the collimator of the Thomson Parabola was defining indeed a quasi-point like and monodirectional source of particles which produced rather small signal spots on the detectors, contrary to our measurement at ELSA, where the largest angle we could use was 45°.

The ratio Q(I) as a function of the IP angle with respect to the incident particle direction is shown in Fig. 4.8.

	α in (10^{-4}) PSL/keV	CPO	Bonnet et al.
α_{MS}	4.31 ± 1.5	4.9 ± 1.5	3.63 ± 0.17
α_{SR}	1.87 ± 0.65	1.82 ± 0.65	2.47 ± 0.07
α_{TR}	1.56 ± 0.09	1.32 ± 0.4	2.02 ± 0.07

Table 4.1: Sensitivities for each type of IP using Bonnet et al. model.

We see in this figure an increase of the IP response with increasing angle, which can be interestood as an increase in the effective thickness traversed by the protons when their incoming direction angle with respect to the IP normal gets larger. The comparison with the $1/\cos(\theta)$ curve in the same figure permits to see this geometrical effect, if it permits to scale the ratio Q(I) up to 45° does not reproduce the point at 75°.

We compare our data points with our GEANT4 simulation, which reproduces very well the experiment up to 75°. This means in particular that the average energy loss of the protons inside the IP active layer explains alone the IP response variation with the angle. We know, indeed, that with protons, we have a very small contributions of secondary particles to the average loss.

The analysis of the evolution of the proton average energy loss inside the MS active layer must be made as follows. According to the NIST/PSTAR data base, even at 75°, where the $1/\cos(\theta)$ factor is about 4, the energy loss of 11.5 MeV protons is small, a fraction of MeV. Following the same idea, we can estimate an average energy loss of the protons inside the MS active layer of around 3.3 MeV. Multiplied by the MS sensitivity, this should correspond to a response of 1.7 PSL, i.e. since the energy losses are not large with respect to the proton kinetic energy, we find roughly the geometrical factor $1/\cos(\theta)$. Given what is said above, we can conclude that this IP MS response increase lower than the geometrical increase of the average active layer thickness can only be related to multiple scattering inside both the protection layer and the active layer. Such an effect, well taken into account by GEANT4 reduces the average length of the proton tracks inside the active layer.

The same angular dependence measurement was done with the 8 MeV beam impinging on the 100 μm tungsten target. In this case, as computed with SRIM, the energy lost by the protons is of the order of their kinetic energy. This means that for this measurement, the estimate of the average kinetic energy of the protons entering the Thomson Parabola is sensitive to the target thickness which is not garanteed by Goodfellow to better than ± 15% with a distribution around an average value not provided by the company.

With 100 μm, SRIM calculations lead to an average kinetic energy of 1.5 MeV ±0.2 MeV on the Thomson Parabola detector.

The data points, displayed as IP responses are shown as a function of the incident angle in Fig. 4.9. We see in particular that the responses decrease with increasing angles. In this figure we compare our measurement with two GEANT4 calculations, corresponding to two values of the incoming proton energy: 1.35 and 1.5 MeV. We see a much better agreement of the curve at 1.35 MeV with the data than the curve at 1.5 MeV.

From such a result we conclude again a good description of our measurement with GEANT4. Anyway, because of the observed dependence of the GEANT4 prediction on the proton kinetic energy, we have also here to underline that a special care will have to be brought to the ray-tracing calculations inside the magnetic field maps in SEPAGE and SESAME, in order to have an unambigious relationship between the positions measured on the detectors and the particle energies. This seems to be a prerequisite to GEANT4 calculations necessary for the data analysis in both diagnostics.

4.6 MCP results

Using the geometry at 0° with respect to the incoming beam direction, we have detected particles (protons and carbon ions) in the MCP placed behind the Thomson Parabola (see Fig.4.1). The aim of the present analysis is to determine the magnetic and electric field integrals, which these particles are sensitive to.

We used different targets and different beam energies for each type of particles. Unfortunately, during the data analysis a beam pointing instability was observed (with the accuracy we were aiming at, i.e. at few 100 μm). Therefore, to determine the field integrals, we decided to use calibration of different measurements at the same beam and particle energies, as detailed below.

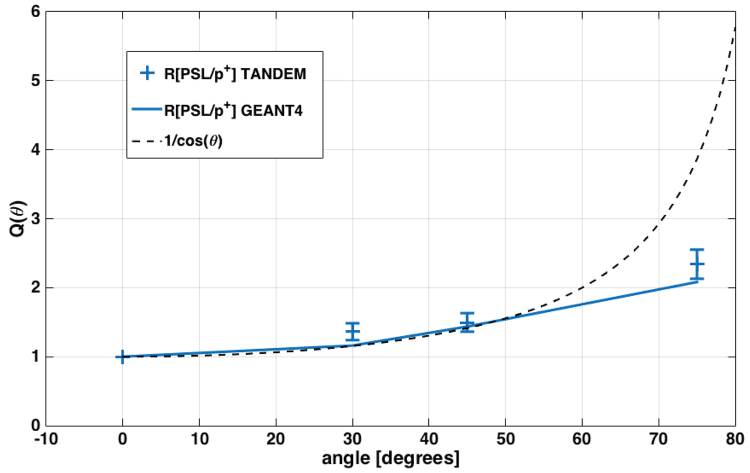

Figure 4.8: Dependence of the response function ratio Q(I) on the angle of the incoming protons with respect to the normal of an MS IP (11.5 MeV kinetic energy).

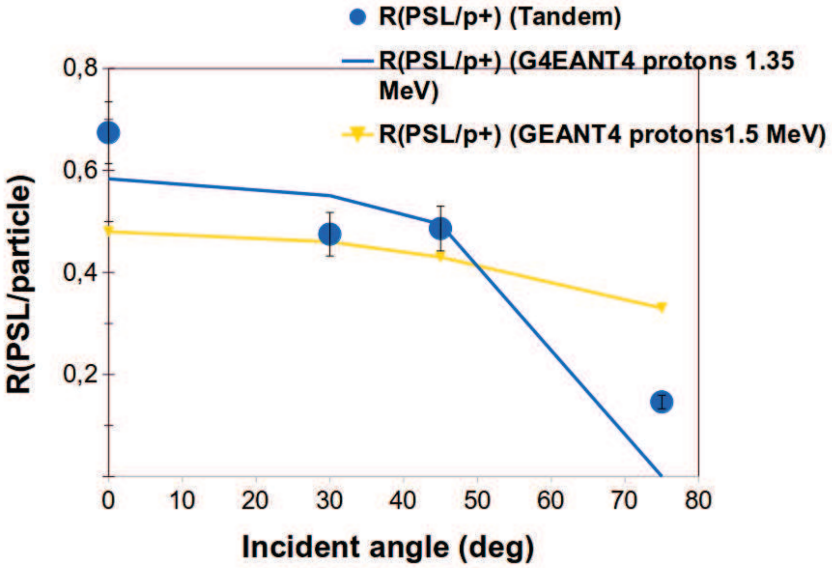

Figure 4.9: The signal in the IP MS for protons 1.35 MeV in function of the angle.

The analysis starts with the determination of the electric field integral. For this we use the proton measurement at two field values (0 and 1.25 MV/m), which were performed with the thin targets (either aluminum or tantalum), where the average proton energy losses are small, and thus, giving measurements independent of possible errors in the determination of the target thickness.

The list of the measurements used in the analysis and discussion below is shown in Tab. 4.2.

4.6.1 Discussion

In order to calculate the electrostatic deviations we use the formula calculated in Appendix A (see eq.A.11)

$$\Delta_\mathrm{x} = \frac{\mathrm{qEL_E}}{4\mathrm{T_0}}(\mathrm{L_E} + 2\mathrm{L_D}), \tag{4.5}$$

where:

Δ_x is the electric deviation on the detector
q is the charge
E is the electric field
$\mathrm{L_E}$ is the length of the electrodes
$\mathrm{T_0}$ is the kinetic energy
$\mathrm{L_D}$ is the distance from the exit of the electrodes and the IP

The aim here is to determine the product $\mathrm{EL_E}$, called the field integral. Practically, speaking, $\mathrm{L_E}$ is fixed to the physical length of the electrodes. This means that we estimate in our data analysis the "equivalent" constant elecrostatic field E, which is afterwards compared to its value between the plane electrodes of the Thomson Parabola.

The values of the deviations are taken as the average of the histograms shown e.g. in Fig.4.10 and followings. These histograms present the MCP position distribution from the MCP recorded signal.

The method goes as described here:

For each measurement, we compute the product $\Delta_\mathrm{x} \times \mathrm{T_0}$ according to Eq. 4.5, this provides estimates of

E_{beam} [MeV]	Target	Thickness [μm]
22	Tantalum	1
	Tungsten	100
15	Tantalum	1
	Tungsten	100 7
	Aluminum	0.8
10	Tantalum	1
	Tungsten	100
	Aluminum	0.8
8	Tantalum	1
	Tungsten	100
	Aluminum	0.8
7.9	Tantalum	1
	Tungsten	100
	Aluminum	0.8
7.2	Tantalum	1
	Tungsten	100
	Aluminum	0.8
6	Tungsten	100
	Aluminum	0.8
5	Tantalum	1
	Aluminum	0.8
3	Tantalum	1
	Aluminum	0.8

Table 4.2: List of the measurements used to determine the electric and magnetic field integrals with the proton beam.

$\Delta_{\mathrm{x}} \times \mathrm{T}_0[\mathrm{MeV}] = \mathrm{qEL}_{\mathrm{E}} \times \mathrm{G}_{\mathrm{Geom}}$
with $\mathrm{G}_{\mathrm{Geom}} = \frac{1}{4}(\mathrm{L}_{\mathrm{E}} + 2\mathrm{L}_{\mathrm{D}})$

$\mathrm{G}_{\mathrm{Geom}}$ is a known geometrical factor. The average of the estimated products $\Delta_x \times T_0$ leads to:
$\mathrm{qEL}_{\mathrm{E}}.\mathrm{G}_{\mathrm{Geom}} \sim 16.6$ mm.MeV

Taking into account the width of the proton energy distribution as computed with SRIM on a 1 μm to a target of $\delta \mathrm{E} \sim 10^{-2}$ MeV. This provides a first error estimate on the factor above of $\sigma(\mathrm{qEl}_{\mathrm{E}}\mathrm{G}_{\mathrm{Geom}}) \sim$ 0.15 mm.MeV.
This leads to:
$\mathrm{qEL}_{\mathrm{E}} \sim 0.076$ MeV $\sigma(\mathrm{qEl}_{\mathrm{E}}) \sim 0.8$ keV

2) We use this value of the electrostatic field integral to determine the proton kinetic energies corresponding to measurements where the average energy loss of the protons in the beam target is not small, i.e. to low kinetic energies and momenta inside the Thomson Parabola. This choice is driven by the known fact that for a fixed spatial uncertainty σ_{x} of a measured magnetic deviation x, the error on the field integral is given by the ratio $\sigma_{\mathrm{x}}/\mathrm{x}$. Therefore maximizing x for a fixed σ_{x}, permits to reduce the error on the magnetic field integral. And usually, σ_{x} is not related to x but to the detector spatial resolution, usually constant over its whole detection surface.

3) For three beam kinetic energies we have:

E(beam)= 7.9 MeV	Al/Ta: $\mathrm{T}_0 \sim 7.9$ MeV; tungsten: $\mathrm{T}_0 \sim 1.9$ MeV;
E(beam)= 8 MeV	Al/Ta: $\mathrm{T}_0 \sim 8$ MeV; tungsten: $\mathrm{T}_0 \sim 2.2$ MeV;
E(beam)= 10 MeV	Al/Ta: $\mathrm{T}_0 \sim 10$ MeV; tungsten: $\mathrm{T}_0 \sim 5.56$ MeV;

Using the relationship:

$$\Delta_{\mathrm{y}} = \frac{\mathrm{qBL}_{\mathrm{B}}\mathrm{c}}{\mathrm{mc}^2\beta_0} \times \mathrm{H}_{\mathrm{Geom}} \tag{4.6}$$

where mc^2 is the proton rest energy, β_0 its reduced velocity ($\beta_0 = \frac{\mathrm{v}_0}{\mathrm{c}}$) and $\mathrm{H}_{\mathrm{Geom}}$

another known geometrical factor, we have, with reduced velocities β_0 labelled with the corresponding beam targets at a fixed value of the beam energy:

$$\Delta_y(W) - \Delta_y(Ta) = \frac{qBL_Bc}{mc^2} \times H_{Geom} \left(\frac{1}{\beta_0(W)} - \frac{1}{\beta_0(Ta)} \right) \tag{4.7}$$

Such a quantity is:

- independent of the origin, on the MCP detector, of the magnetic deviations (i.e. the point of zero deviation)

- independent of fluctuations in the position of the proton spots between different beam settings as shown in Tab. 4.3 for the position measured on the electrostatic deviation direction at zero electrostatic field and as examples in Fig. 4.11 for two beam energies (10 and 15 MeV).

The field integrals obtained for the three energies are:

E(beam)= 7.9 MeV $\Delta_y = -6.66$ mm $\Delta(\frac{1}{\beta_0}) = 8.91$ $I(B) = B.L_B = 4.3\,10^{-3}\,m.T$

E(beam)= 8 MeV $\Delta_y = -5.7$ mm $\Delta(\frac{1}{\beta_0}) = 6.59$ $I(B) = B.L_B = 5\,10^{-3}\,m.T$

E(beam)= 10 MeV $\Delta_y = -1.48$ mm $\Delta(\frac{1}{\beta_0}) = 2.42$ $I(B) = B.L_B = 4.4\,10^{-3}\,m.T$

4.6.2 The determination of uncertainties

In a Thomson parabola, as explained previously, the deviation provided by the electric field is given as:

$$x_D = \frac{qEL_E}{T_0} G_{Geom} \tag{4.8}$$

Where $E.L_E$ is the electric field integral (average field component times the electrodes length). T is the kinetic energy of the particle and $G_{Geom} = \frac{1}{4}(L_E + 2L_D)$ is a geometrical factor.

In our experiment we determined x_D as the difference between the average particle spot coordinate measured with a zero electric field (see Fig. 4.10 and 4.11) and the average spot coordinate measured with the full voltage on the electrodes (± 12.5 kV in our experiment). As explained above, we used three beam settings (E= 7.9, 8 and 10 MeV) to determine the field integral $I(E) = EL_E$, indicated

E_{proton} (MeV)	Target	<x> mm	RMS mm
3	Tantalum	35.89	0.74
	Aluminum	35.90	0.46
5	Tantalum	35.82	0.46
	Aluminum	35.82	0.46
7.2	Tantalum	35.70	0.43
	Aluminum	35.72	0.28
7.9	Tantalum	35.25	0.33
	Aluminum	35.31	1.05
	Tungsten	35.35	0.33
8	Tantalum	35.89	0.59
	Aluminum	35.89	0.59
	Tungsten	36	0.28
10	Tantalum	35.43	1.25
	Aluminum	35.41	1.91
	Tungsten	35.64	0.35
15	Tantalum	35.47	1.54
	Aluminum	35.35	1.72
	Tungsten	35.51	0.72
22	Tantalum	36.06	0.58
	Aluminum	36.13	0.49
	Tungsten	36.07	0.49

Table 4.3: List of the measurements used to determine the stability of the beam spot in the electric deviation direction for 0 V on the electrodes.

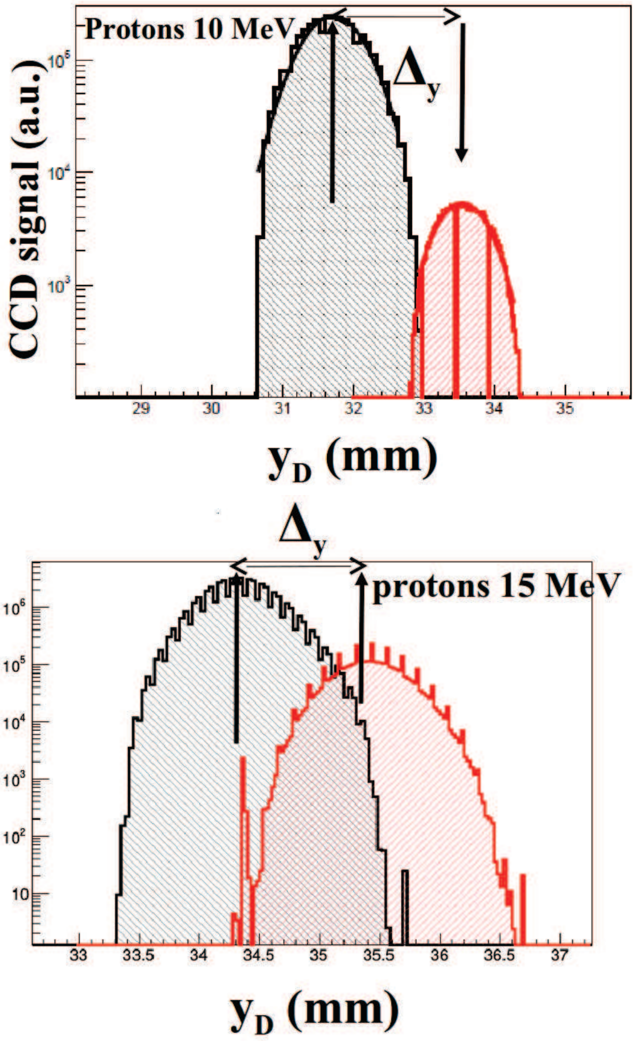

Figure 4.10: Δ_y obtained using protons of 10 and 15 MeV and two targets (aluminium and tantalum).

below with i, with the formula

$$I(E) = \frac{1}{N} \sum_i x_D(i) T_{0,i} \frac{1}{G_{Geom}} \tag{4.9}$$

In this formula, we have identified three sources of error, which can induce uncertainties on the fields integral I(E):

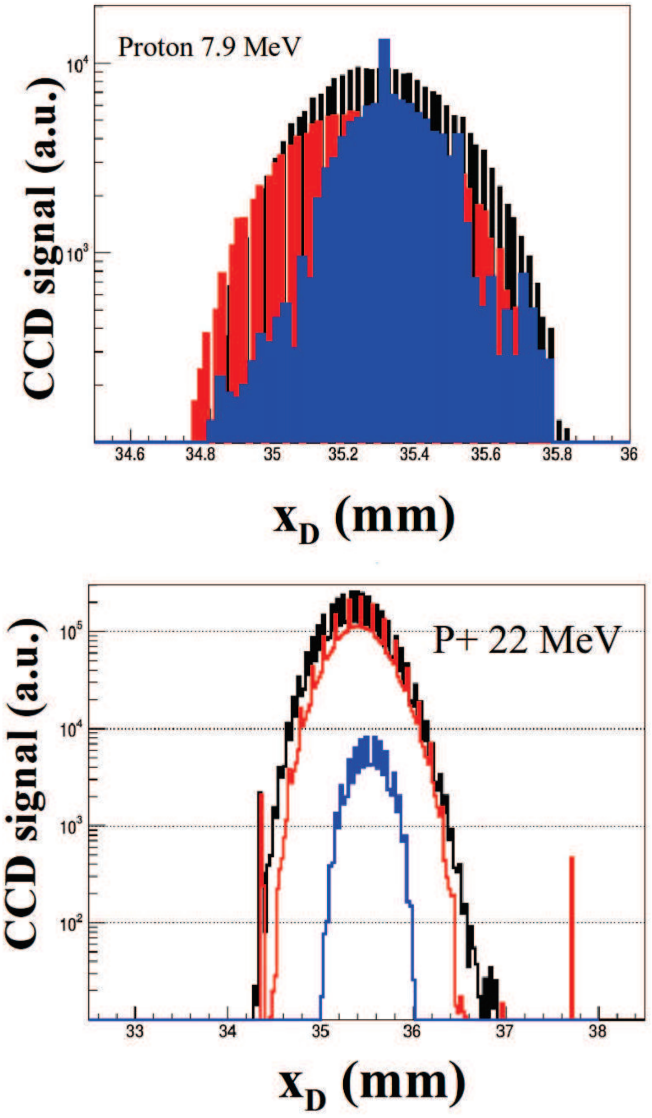

Figure 4.11: Proton distribution for the beam energy of 3 and 5 MeV on the electric field deviation axis for zero electric field.

1. error on the determination of the deviation x_D
2. error on the knowledge of the geometry of our setup (G_{Geom})
3. error on the estimate of the kinetic energy of each beam setting.

Since we work, to determine I(E) by comparing, for each setting, the beam spot average position with and without the electric field, we took as an uncertainty on $\mathrm{x_D}$ the variations we measured on the $\mathrm{y_D}$ coordinate from one detection to another for a determined beam setting (see Tab. 4.3). Such variations induce an uncertainty of 40 μm when computed with the positions given in Tab. 4.3.

The uncertainty on the estimate of the kinetic energy of protons coming into the Thomson Parabola is linked to:

- The uncertainty on the beam energy (estimated to 10^{-4} in $\frac{\delta \mathrm{p}}{\mathrm{p}}$), which is negligible
- The uncertainty on the tantalum target thickness, which can generate, via the proton stopping power, our error on the kinetic energy at the entrance of the SEPAGE PTBE.

We consider a typical uncertainty on the tantalum thickness (1 μm in our case) of 10%, namely 0.1 μm. Considering the average stopping power in tantalum of protons in the range 8-10 MeV, this provides an error of tantalum of:

$$\delta \mathrm{T_0} = \left\langle \frac{\mathrm{dE}}{\mathrm{dx}} \right\rangle .0.1\ \mu\mathrm{m} \tag{4.10}$$

That is to say: $\delta \mathrm{T_0} \sim 3.8.10^{-3}$ MeV.

Finally, the uncertainty on the geometrical factor G_{Geom} comes from a possible error on $\mathrm{L_D}$, which we estimate to be at most of 2 mm. This implies an error on $\mathrm{G_{Geom}}$ of $\delta \mathrm{G} = 1$ mm

Each of these three contributions corresponds to an error on I(E) given by:

$$\delta_{\mathrm{p}} \mathrm{I(E)} = \left| \frac{\partial \mathrm{I(E)}}{\partial \mathrm{p}} \right| \delta \mathrm{p} \tag{4.11}$$

Where $\mathrm{p} = \mathrm{x_D/T/G_{Geom}}$

For $\mathrm{p} = \mathrm{x_D}$, we have:

$$\delta_{\mathrm{x}} \mathrm{I(E)} = \delta \mathrm{x_D} \times \frac{1}{\mathrm{N.G_{Geom}}}.\sum\nolimits_{\mathrm{i}} \mathrm{T_i} \tag{4.12}$$

For $\mathrm{p} = \mathrm{T_{0,i}}$, we have:

$$\delta_{\mathrm{T}} \mathrm{I(E)} = \delta \mathrm{T_{0,i}} \times \frac{1}{\mathrm{N.G_{Geom}}}.\sum\nolimits_{\mathrm{i}} \mathrm{x_D(i)} \tag{4.13}$$

For $p = G_{Geom}$:

$$\delta_G I(E) = I(E) \times \frac{\delta G_{Geom}}{G_{Geom}} \tag{4.14}$$

Numerically, this translates into:

$\delta_x I(E) = 1.52.10^{-6}$

$\delta_T I(E) = 2.9.10^{-5}$

$\delta_G I(E) = 3.3.10^{-5}$

We have hence:

$\frac{\delta(I)}{I} = 4.10^{-3}$

The magnetic field integral is given by the expression:

$$I(B) = BL_B \tag{4.15}$$

where B is the average dipole field component and L_B is the magnet length. The magnetic field integral has been determined using two targets with three beam settings I=7.9, 8 and 10 MeV, respectively: → Either a thin target (Ta/Al)

→ A thicker target (tungsten of 100 μm)

Averaging on these three measurements and using the formulas developed above, we have:

$$I(B) = \frac{1}{N} \sum_i \frac{\Delta y_D(i)}{0.17} \times \left(\frac{1}{\beta_0}(W)_i - \frac{1}{\beta_0}(Ta/Al)_i \right)_i^{-1} \tag{4.16}$$

where $\Delta y_D(i) = y_D(W) - y_D(Ta/Al)$

1. $\beta_0(W)$ is the proton reduced velocity in the SEPAGE/PTBE with the 100 μm tungsten target in the beam.
2. $\beta_0(Ta/Al)$ is the proton reduced velocity with the thin (Ta/Al) target in the beam.

Using the formula above, we neglected the uncertainty from the geometry, which is even smaller in the case of I(B) than for I(E).

We have here also three sources of error:

→ on the position difference $\Delta y_D(i)$

→ on $\beta_0(\mathrm{W})$

→ on $\beta_0(\mathrm{Ta/Al})$

Since $\Delta \mathrm{y_D(i)} = \mathrm{y_D(W)_i} - \mathrm{y_D(Ta/Al)_i}$, we take as uncertainty on $\Delta \mathrm{y_D(i)}$ the quadratic sum of the uncertainties on both terms, which is taken as 40 μm as above for the electric field integral incertainty calculation. This leads to:

$\delta\Delta \mathrm{y_D(i)} \sim 60\ \mu\mathrm{m}$

The uncertainty on $\beta_0(\mathrm{Ta/Al})$ is also included and comes from the uncertainty on the target thickness. We must consider here 10% error in the tantalum thickness as well, leading to an error on the energy of:

$\delta \mathrm{T_0} \sim 4.10^{-3}$ MeV

This translates into an error on the term $\frac{1}{\beta_0}(\mathrm{Ta/Al})$ given by:

$$\delta(\frac{1}{\beta_0}(\mathrm{Ta/Al})) \sim \frac{1}{2\beta_0}(\mathrm{Ta/Al}) \times \frac{\delta \mathrm{T_0}}{\mathrm{T_0(Ta/Al)}} \tag{4.17}$$

i.e. $\delta(\frac{1}{\beta_0}(\mathrm{Ta/Al})) \sim 2.10^{-3}$

which we take as constant, $\frac{\delta \mathrm{T}}{\mathrm{T}}$ and $\frac{1}{\beta_0}$ being determined for $\mathrm{T_0} = 8$ MeV.

In the settings we use for the determination of I(B) the average loss of the protons inside the 100 μm tungsten target which is not small with respect to the beam energy. Therefore, to determine $\mathrm{T_{0,i}(W)}$, the corresponding energy (and hence $\beta_0(\mathrm{W})_\mathrm{i}$) we use the electric deflection. The error on $\mathrm{T_{0,i}(W)}$ for each setting i, is then given by the error on I(E) as:

$$\delta \mathrm{T_0(W)_i} = \mathrm{T_{0,i}(W)} \times \frac{\delta \mathrm{I(E)}}{\mathrm{I(E)}} \tag{4.18}$$

The relationship between $\mathrm{T_0}$ and I(E) being linear, averaging over the three settings this gives a small value of $\delta \mathrm{T(W)_i}$.

This can be translated into an uncertainty on $\frac{1}{\beta_0}(W)_i$ as:

$$\delta(\frac{1}{\beta_0}(\mathrm{W})) = \frac{1}{2\beta_0}(\mathrm{W}) \times \frac{\delta \mathrm{T_0(W)}}{\mathrm{T_0(W)}} \tag{4.19}$$

$$\delta(\frac{1}{\beta_0}(\mathrm{W})) = \frac{1}{2\beta_0}(\mathrm{W}) \times \frac{\delta \mathrm{I(E)}}{\mathrm{I(E)}} \tag{4.20}$$

As for the electric field integral, we obtain three uncertainties on I(B), which are:

$$\delta_{\mathrm{y}}\mathrm{I(B)} = \frac{1}{\mathrm{N}\times 0.17}\times\sum\nolimits_{\mathrm{i}}\left(\frac{1}{\beta_0}(\mathrm{W})_{\mathrm{i}} - \frac{1}{\beta_0}(\mathrm{Ta/Al})\right)^{-1}\times\delta\Delta \mathrm{y_D} \tag{4.21}$$

$$\delta_{\beta_0(\mathrm{Ta/Al})_{\mathrm{i}}}\mathrm{I(B)} = \frac{1}{\mathrm{N}\times 0.17}\times\sum\nolimits_{\mathrm{i}}\left(\frac{1}{\beta_0}(\mathrm{W})_{\mathrm{i}} - \frac{1}{\beta_0}(\mathrm{Ta/Al})\right)^{-2}\times\Delta \mathrm{y_D(i)}\times\delta(\frac{1}{\beta_0}(\mathrm{Ta})) \tag{4.22}$$

$$\delta_{\beta_0(\mathrm{W})_{\mathrm{i}}}\mathrm{I(B)} = \frac{1}{\mathrm{N}\times 0.17}\times\sum\nolimits_{\mathrm{i}}\left(\frac{1}{\beta_0}(\mathrm{W})_{\mathrm{i}} - \frac{1}{\beta_0}(\mathrm{Ta/Al})\right)^{-2}\times\Delta \mathrm{y_D}\times\delta\frac{1}{\beta_0}(\mathrm{W}) \tag{4.23}$$

If we add linearly the contribution of the beam settings to the error, we write:

$$\delta_{\beta_0}\mathrm{I(B)} = \frac{1}{\mathrm{N}\times 0.17}\sum\nolimits_{\mathrm{i}}\Delta \mathrm{y_D(i)}\left(\frac{1}{\beta_0}(\mathrm{W})_{\mathrm{i}} - \frac{1}{\beta_0}(\mathrm{Ta/Al})_{\mathrm{i}}\right)^{-2}\times(\delta\beta_0(\mathrm{W}) + \delta\beta_0(\mathrm{Ta/Al})) \tag{4.24}$$

This linear contribution of errors is of course, an overstimate of the error on I(B). Quadratically added, this leads to the formula:

$$\delta_{\beta_0}\mathrm{I(B)} = \frac{1}{\mathrm{N}\times 0.17}\left(\sum\nolimits_{\mathrm{i}}\Delta \mathrm{y_D(i)}^2\left(\frac{1}{\beta_0}(\mathrm{W})_{\mathrm{i}} - \frac{1}{\beta_0}(\mathrm{Ta/Al})_{\mathrm{i}}\right)^{-2}\right)^{\frac{1}{2}}\times\left(\delta\beta_0(\mathrm{W})^2 + \delta\beta_0(\mathrm{Ta/Al})^2\right)^{\frac{1}{2}} \tag{4.25}$$

Numerically we obtain:
$\delta_{\mathrm{y}}\mathrm{I(B)} = 8.27.10^{-6}$
$\delta_{\beta_0(\mathrm{Ta/Al})_{\mathrm{i}}}\mathrm{I(B)} = 1.6.10^{-4}$
$\delta_{\beta_0(\mathrm{W})_{\mathrm{i}}}\mathrm{I(B)} = 5.10^{-4}$

The quadratic error is: 5%

4.7 Summary of Chapter 4

In order to calibrate the IPs to protons of energies in the range of few MeV, the experiment at the Tandem proton accelerator was performed. The responses of single IPs to protons from 1 MeV to 22 MeV were measured and it was shown that the obtained results are coherent with what we measured in the CPO (see Chap.4) and with Bonnet et al. [42]. Moreover, the response of IPs as a function of the incident angle was measured and the obtained experimental data agree with GEANT4 simulations.

Using the proton beam, we determined the electric and magnetic field integrals. In this case, a micro-channel plate (MCP) detector was employed as the particle detector. The obtained integral of the electric field of the parabola was higher than the expected value by 50%. This is favorable for the diagnostic since it will provide a higher separation power between ion species, in particular between the proton and the $^{12}C^{6+}$ parabolas in the "low−energy" channel of SEPAGE, which was one of the specification points in the conceptual design of the project. The result of the integral of the magnetic field corresponds to the designed value within the error bars. Therefore, the Thomson parabola was analysed and calibrated and it can thus be used in the SEPAGE diagnostics.

Chapter 5

Conclusion and perspectives

This dissertation focuses on the study of passive detectors for charged particles of the PETAL diagnostics. These detectors will be used in SEPAGE (Spectrometre Électrons Protons A Grande Énergie) and SESAME (Spectrometre ElectronS A Moyenne Energie) diagnostics at LMJ/PETAL, aiming at measuring energy spectra of particles accelerated with PETAL (electrons, protons and ions). Therefore, passive detectors must be properly calibrated for these particles in the energy range from 0.1 to $\sim$ 200 MeV, for which these diagnostics were designed.

For this purpose, four experiments using four different sources of particles were performed and the obtained experimental data were carefully analyzed and interpreted. Our measurements were also compared with data from the literature. The TANDEM accelerator was used as a source of protons in the energy range between 1 MeV and 22 MeV. This experiment was also a benchmark test with protons and carbon ions of the charged particle transport in the demonstrator of the "low-energy channel" Thomson parabola of SEPAGE. The proton synchrocyclotron source at Centre de Protonthérapie d'Orsay (CPO) provided protons in the energy range from 80 MeV to 200 MeV. The electrons in the range from 5 MeV to 18 MeV accelerated by the linear accelerator (ELSA) were used. Lastly, the high-energy electrons generated by the laser wakefield accelerator at Laboratoire d'Optique Appliquée (Salle Jaune, LOA) were used in the energy range between 40 MeV and 180 MeV. This work is divided into different chapters according to these performed experiments. We have not only studied the responses of single

Imaging Plates (IP), which is the type of passive detectors chosen for the charged particle detection in SESAME and SEPAGE, but also composite detectors made of IPs and of layers of high-Z material, e.g. tungsten. The use of such composite detectors will be necessary in the PETAL diagnostics for two main reasons:

- To protect the detection signals from the high photon background in LMJ-PETAL related either directly to the laser shots or coming from the decay of the activated materials of the LMJ sphere, shortly after the shots.
- To have detector responses independent of the mechanics in the close environnement of the detector

Two models, which link these detector responses to particle average energy losses within the active layer of IP and which were taken from the literature, were studied for the interpretation of our measurements. Since the particle energy losses inside the IP active layers are not experimental observables, they need to be computed with simulations. To do this, we chose GEANT4 for reasons detailed in the manuscript.

Using GEANT4, we extracted from our measured detector responses sensitivities as, roughly, the ratio between the responses and the average particle energy losses. We have shown that these sensitivities are well-based concept since we found constant sensitivities for each type of particle and for each type of detector (MS, SR, TR IPs). These sensitivities combined with our GEANT4 calculations allowed us to compute the detector responses over the energy range from 0.1 to 1000 MeV, which describe most of existing data.

The comparison of the sensitivities determined for protons and electrons shows very similar values for MS and SR IP types, which gives credence to this concept. Anyway, the sensitivities of TR IPs happen to be different for electrons and protons, contrary to the other two types of IPs. This remains to be explained by further investigations.

We have pushed this concept a little further with measurements of the responses of detectors composed of IPs and layers of high-Z material. Our measurements showed global increase of the Imaging Plate responses in the presence of such layers, both in front of or behind the detectors with respect to the incoming particles direction. These increases are very well described by the evolution of the energy losses of the particles as computed with our GEANT4 simulations. Depending on the type of particle as well as the energy range of the particles, the contributions to these increases from the primary particle energy losses or from secondary or higher order particles coming from the particle-detector interactions are different but may be very substantial, more than half of the responses. Given that these secondary and higher order particles are in a much lower energy spectra than the primary particles (i.e. a few tens of keV), this good agreement between measurements and calculations probably means that the concept of IP sensitivity of the same values applies also to this energy range for protons and electrons. The comparison between experiments and simulations was also done for the measurement of the Bragg peak at 160 and 200 MeV protons in thick composite detectors. The good description of these two measurements by our simulation, in particular the location of the Bragg peak within our detector is particularly important since such a detector permits, in fact, to test the Imaging Plate responses over the whole energy range from 160 - 200 MeV down to 0 (the protons are stopped inside the detector). As such, this measurement provides a ultimate test bench of our particle - detector interaction model.

We have lead our detailed study of Imaging Plate responses to their dependence on the angle between the incoming particles and the direction orthogonal to the IP plane. The measurement was made possible by our setup at the TANDEM accelerator where we used the demonstrator of the low-energy channel Thomson parabola of SEPAGE. This setup provided monodirectional and thin particle beams impinging on the detector, which permitted to measure the detector response for angles of up to 75 degrees. These data are also well described by our calculations.

The test of the demonstrator provided the field integrals of the low-energy channel Thomson parabola of SEPAGE. We used proton and carbon ion beams but the results presented here concern only the proton measurement. The measured magnetic field integral corresponds to the specifications given to the industrial company which built it. The electric field integral was measured at a much higher value than the design (50% increase). This result needs to be explained. It may be related to the geometry of the electrostatic plates' edges, which generate an electric field rather far away on the particle axis.

The perspectives which may be built from this work are of four types. The first one is, of course, the application of our knowledge and experience to the building of the actual detectors to be put into the SESAME and SEPAGE diagnostics. For this, our optimization procedure should take into account the effect of high-Z material shielding on the detected signal (surface spreading) and compare the results to:

- the energy resolution of the diagnostics, as specified at the beginning of the project
- the level of constant background signal from the hard X-ray photons, mentioned in the introduction.

To do this, a first estimate of the level of this background on the detector has to be computed.

The second direction of investigation should be the calibration of Imaging Plates and composite detectors using low-energy electrons. The goal of such an experiment should be to cover the energy range below 1 MeV, where the two models we used in the present study differ notably. For this, a rather simple setup made of a ^{90}Sr/^{90}Y beta source combined with a small dipole magnet is sufficient.

A third study which would be interesting in the detailed understanding of the interaction of the charged particles with our composite detectors would be the study of the interaction of “high-energy” electrons (a few tens MeV) with thick detectors. We have indeed seen in our study that the contribution of secondary and higher-order particles in the detector responses to electrons is very important but we have not performed the measurement at LOA for very thick detectors as we did at CPO for $\sim$ 200 MeV protons.

The fourth perspective we can draw from our work would be the detection of single particles, such as neutrons, with Imaging Plates and composite detectors. Such particles may leave in IP as much as one PSL on a few pixels and should therefore be detected with a good efficiency.

Eventually, the experience gained with this systematic study could also be useful at many large and high-energy femtosecond lasers being developed around Europe to start particle detectors before having solved potential problems of laser-generated electromagnetic pulses in the readout electronics connected to the detection.

Appendix A

Principle of a Thomson Parabola

The advantages of the Thomson parabola [48] are its robustness, compactness and the fact that it is well known since the beginning of the 20^{th} century, and can function in an environment such as the LMJ sphere.

A Thomson parabola is composed of a dipole magnet and electrodes, parallel to each other, and generating an electric field parallel to the magnetic field. A collimator is placed at the entrance of the parabola to create a point-like source of quasi−monodirectional particles before the magnetic and electrostatic analyses.

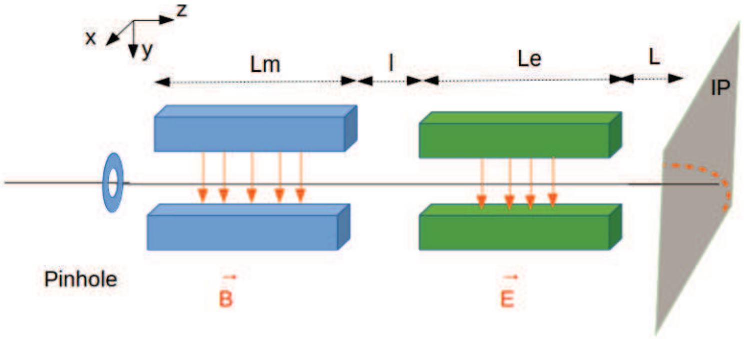

Figure A.1: The scheme of principle of a Thomson parabola. The ions are coming from the left through a pinhole before the magnetic and electrostatic deviations and impiging on the detector at the bottom right.

Fig. A.1 shows the principle of a Thomson parabola. The particles comes from the source through a pinhole. They travel afterwards in between the tips of a magnet, defining a dipole field and two electrodes, which create an electrostatic field parallel to the magnetic field and perpendicular to the main ion direction. The E−field is bending the particle trajectories in its direction, whereas the B−field is bending them perpendicularly to both its direction and the incoming−ion direction. The combination of these two bendings produces on the detector at the bottom of the device parabolic particle distributions, as illustrated in Fig. A.2 [59]. Each distribution defines an ion specie and a charge state as well as its energy/momentum distribution, provided that the detector efficiency as a function of the particle energy has been determined.

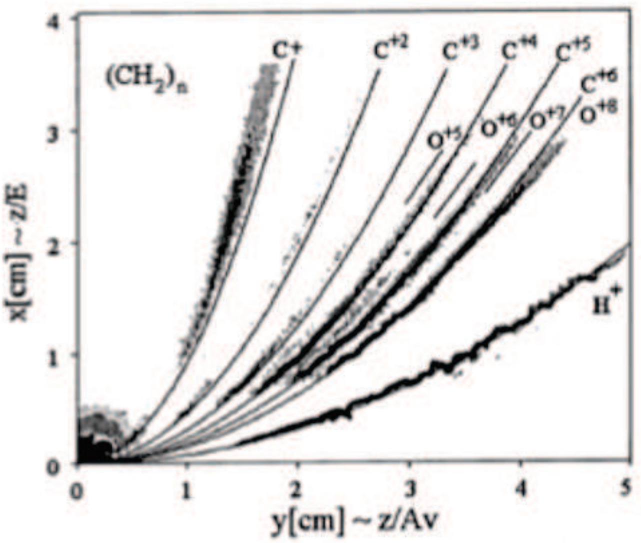

Figure A.2: Typical ion parabolas obtained with an ion−laser acceleration experiment [59]. The different ion species as well as the different charge states can be identified.

The magnetic deviation provides a measurement of the ratio p/q, where p is the particle momentum and q its charge. The electric deviation provides essentially the determination of q/m, identifying therefore the different types of ions.

In the following calculation we take $\overrightarrow{E}$ and $\overrightarrow{B}$ along the y-axis (we neglect the fringe-field distribution and consider only rectangular distributions):

$$\overrightarrow{B} = \begin{bmatrix} 0 \\ B \\ 0 \end{bmatrix} \; ; \; \overrightarrow{E} = \begin{bmatrix} 0 \\ E \\ 0 \end{bmatrix}$$

We restrict our calculations to the paraxial case where transverse deviations from the initial directions are small. In this approximation the velocity along z-axis is constant through the Thomson parabola.

The equation of motion is written for $0<\mathrm{z}<L_m$ (see Fig. A.1):

$$\mathrm{m}\frac{\mathrm{d}^2\mathrm{x}}{\mathrm{dt}^2} = -\mathrm{q}.\frac{\mathrm{dz}}{\mathrm{dt}}.\mathrm{B} \tag{A.1}$$

We take as initial conditions: $(\mathrm{x}_0, \mathrm{y}_0, \mathrm{z}_0) = \overrightarrow{0}$ and $(\mathrm{v}_{\mathrm{x}0}, \mathrm{v}_{\mathrm{y}0}, \mathrm{v}_{\mathrm{z}0}) = (0, 0, \mathrm{v}_0)$ at t=0.

We define ω_c as $\omega_\mathrm{c} = \mathrm{qB/m}$, the particle cyclotron frequency.

Eq.(1) can be integrated as, since dz/dt=v_0=constant:

$$\begin{cases} v_x = -v_0.(\omega_c t) \\ v_z = v_0 \end{cases}$$

And

$$\begin{cases} x = -v_0\omega_c.t^2/2 \\ z = v_0.t \end{cases}$$

At the end of the magnet the ion position is $(\mathrm{x}(\mathrm{t_m}), \mathrm{z}(\mathrm{t_m}))$, with:

$$\mathrm{x}(\mathrm{t_m}) = -\mathrm{v}_0.\omega_\mathrm{c}.\frac{\mathrm{t}_\mathrm{m}^2}{2} \tag{A.2}$$

$$\mathrm{z}(\mathrm{t_m}) = \mathrm{L_m} \tag{A.3}$$

$$\mathrm{t_m} = \frac{\mathrm{L_m}}{\mathrm{v}_0}. \tag{A.4}$$

Protons propagates then in the $\mathrm{d} = \mathrm{l} + \mathrm{L_e} + \mathrm{L}$ distance free of magnetic field of the detector:

$$\mathrm{x_D} = \mathrm{x(t_m)} + \frac{\mathrm{v_x(t_m)}}{\mathrm{v_z(t_m)}}.\mathrm{d} \tag{A.5}$$

$$\mathrm{x_D} = -\frac{\omega_\mathrm{c}.\mathrm{L_m}}{2.\mathrm{v_0}}(\mathrm{L_m} + 2\mathrm{d}) \tag{A.6}$$

For $\mathrm{L_m} + \mathrm{l} < \mathrm{z} < \mathrm{L_m} + \mathrm{l} + \mathrm{L_e}$:

$$\mathrm{m}\frac{\mathrm{d^2y}}{\mathrm{dt^2}} = \mathrm{q.E} \tag{A.7}$$

With the initial condition, this gives:

$$\mathrm{v_y} = \frac{\mathrm{q.E}}{\mathrm{m}}.\mathrm{t} \tag{A.8}$$

$$\mathrm{y} = \frac{\mathrm{q.E}}{\mathrm{m}}.\frac{\mathrm{t^2}}{2} \tag{A.9}$$

$\mathrm{t_e} = \mathrm{L_e}/\mathrm{v_0}$

In the paraxial approximation, the time it takes for the ions to traverse the space between electrodes is $\mathrm{t_E} = \mathrm{d_E}/\mathrm{v_0}$, which will imply the y position of the ion at $\mathrm{z} = \mathrm{L_e} + \mathrm{l} + \mathrm{L_m} + \mathrm{L}$ to be:

$$\mathrm{y_D} = \mathrm{y(t_E)} + \frac{\mathrm{v_y t_e}}{\mathrm{v_z(t_m)}}.\mathrm{L} \tag{A.10}$$

$$\mathrm{y_D} = \frac{\mathrm{q.E.L_e}}{2.\mathrm{m.v_0^2}}(\mathrm{L_e} + 2\mathrm{L}) \tag{A.11}$$

It is to be underlined here that the condition of small deviations does not apply to electrons, whose magnetic rigidity m/q is much smaller than that of ions.

In the case of SEPAGE and SESAME the electrons will be mostly detected in the side of the diagnostics, as mentioned above, in detectors parallel to the particle initial direction. This has also the particular consequence that the electrons will arrive on the detectors with possibly large angles with respect to the orthogonal to the entrance plane. We took this into account in our detector studies by measuring the detection response as a function of the particle angle with respect to the detection plane normal.

Moreover, we should mention here that the electrons in SEPAGE will be unaffected or mostly unsensitive to the electric fields of the SEPAGE Thomson Parabolas. This statement is explained by three features of the electron transport within SEPAGE.

- In the low-energy channel of SEPAGE, the low-energy electrons (below ~ 3 MeV) exit directly the dipole magnet on its side, ie. without passing through the electric field volume between the two electrostatic plates.

- Up to ~ 8 MeV, the electrons of the low-energy channel pass through only a part of this electric field.

- For the highest energy electrons, in both channels, which are relativistic, we must rewrite the equation of motion in the electric field with the introduction of the Lorentz factor γ as:

$$\gamma \mathrm{m} \frac{\mathrm{d}^2\mathrm{y}}{\mathrm{dt}^2} = \mathrm{qE} \tag{A.12}$$

given that in SEPAGE Thomson Parabola, the quantity $\mathrm{qEL_E}$, which is an energy is of the order of or below 0.1 MeV, it is negligible with respect to the electron energies considered here. We can thererfore solve the equation above with a Lorentz factor kept constant. This leads to:

$$\gamma \mathrm{m} \frac{\mathrm{dy}}{\mathrm{dt}} = \mathrm{qEt} \tag{A.13}$$

The electron considered here being highly relativistic (for 8 MeV electrons, $\gamma \sim 17$), their velocity is c and, at the exit of the electrostatic field region we have $\mathrm{t} = \frac{\mathrm{L_e}}{\mathrm{c}}$ and therefore

$$\frac{\mathrm{dy}}{\mathrm{dt}}(\mathrm{L_e}) = \frac{\mathrm{qEL_E}}{\gamma \mathrm{mc}} \tag{A.14}$$

and $\mathrm{y}(\mathrm{L_e}) = \frac{1}{2}\frac{\mathrm{qEL_e^2}}{\gamma \mathrm{mc}^2}$

Following the notation in the appendix we have:

$$\mathrm{y_D} = \frac{\mathrm{qEL_E}}{2\gamma \mathrm{mc}^2}(2\mathrm{L} + \mathrm{L_e}) \tag{A.15}$$

which can be written, with γ»1 and $\mathrm{E_e}$ the electron kinetic energy as:

$$\mathrm{y_D} = \frac{\mathrm{qEL_E}}{\mathrm{2E_c}}(\mathrm{2L} + \mathrm{L_e}) \tag{A.16}$$

For 8 MeV electrons in the low-energy channel of SEPAGE, this gives $\mathrm{y_D} \sim 4$ mm

These numbers have been checked by a ray tracing simulation of the electrons in the SEPAGE Thomson Parabolas using the software ZGOUBI developed at CEA-Saclay [79].

Appendix B

Model comparison for high-energy charged particles

In order to compare Hidding et al. [25] and Bonnet et al. [42] [64] models for high-energy charged particles, we will start with Bonnet et al. model that takes into account the depth dependence of the photon propagation inside the IP first layers:

$$\mathrm{R(E)} = \alpha \int_0^{\epsilon} \frac{\mathrm{dE}}{\mathrm{dz}}.\exp(-\frac{\mathrm{z}}{\mathrm{L}})\,\mathrm{dz} \tag{B.1}$$

In this equation, z is the depth in the phosphoric film of thickness ϵ, L is the absorption length of the PSL photons, dE/dz is the deposited energy profile and α is the IP sensitivity (in PSL per energy loss unit).

For high-energy particles, $\frac{\mathrm{dE}}{\mathrm{dz}}(\mathrm{z}) = \mathrm{cte}$, i.e.:

$$\mathrm{R(E)} = \alpha \frac{\mathrm{dE}}{\mathrm{dz}} \int_0^{\epsilon} \exp(-\frac{\mathrm{z}}{\mathrm{L}})\,\mathrm{dz} \tag{B.2}$$

$$\mathrm{R(E)} = \alpha \frac{\mathrm{dE}}{\mathrm{dz}}.\mathrm{L} \int_0^{\epsilon/\mathrm{L}} \exp(-\mathrm{u})\,\mathrm{du} \tag{B.3}$$

$$R(E) = \alpha\frac{dE}{dz}.L[1-\exp(-\frac{\epsilon}{L})] \qquad (B.4)$$

In our study of the interaction of charged-particles with imaging plates, we may indeed define as high-energy particles those for which the stopping power dE/dz is constant through IPs.

$$R(E) = \alpha\frac{dE}{dz}.\epsilon.\frac{L}{\epsilon}(1-\exp(-\frac{\epsilon}{L})) \qquad (B.5)$$

with $\epsilon.dE/dz = \Delta E$, the particle energy loss in the IP active layer.

We obtain:

$$R(E) = \alpha\frac{L}{\epsilon}(1-\exp(-\frac{\epsilon}{L})).\Delta E \qquad (B.6)$$

Equalizing this formula with that of Hodding et al.:

$$R(E) = \alpha_{\mathrm{Hidding}}.\Delta E \qquad (B.7)$$

leads to:

$\alpha_{\mathrm{Hidding}} = \alpha_{\mathrm{Bonnet}}.\frac{L_{\mathrm{Bonnet}}}{\epsilon}(1-\exp(-\frac{\epsilon}{L_{\mathrm{Bonnet}}}))$

Appendix C

The kinematics of the proton/ion Rutherford scattering

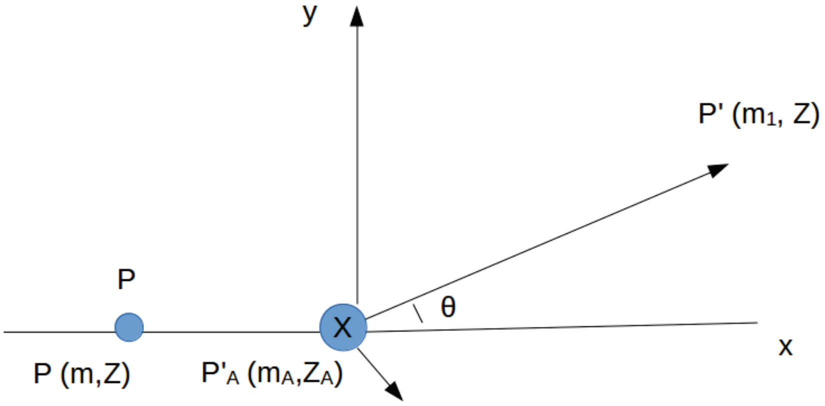

Figure C.1: The kinematics of the proton/ion Rutherford scattering.

In order to calculate the kinetic energy of scattered protons we use the conservation of energy and momentum in the scattering of the proton by the ion (of masses m, m_A and charges Z and Z_A):

$$\begin{cases} p = p'cos\theta + p'_A cos\theta_A & (1) \\ 0 = p'sin\theta + p'_A sin\theta_A & (2) \end{cases}$$

The kinematical variables are defined in Fig.C.1.

Giving:

$$(\mathrm{p} - \mathrm{p}'\mathrm{cos}\theta)^2 + \mathrm{p}'^2\mathrm{sin}^2\theta = \mathrm{p}'^2_\mathrm{A} \tag{C.1}$$

The energy conservation can be written as:

$$\mathrm{E} = \mathrm{E}' + \mathrm{E}'_\mathrm{A} \tag{C.2}$$

with $\mathrm{E} = \mathrm{p}^2/2\mathrm{m}$

$\mathrm{E}' = \mathrm{p}'^2/2\mathrm{m}$

$\mathrm{E}'_\mathrm{A} = \mathrm{p}'^2_\mathrm{A}/2\mathrm{m}_\mathrm{A}$ (non-relativistic kinematics)

$$\begin{cases} \frac{p^2}{2m} = \frac{p'^2}{2m} + \frac{p'^2_A}{2m_A} & (5) \\ p'^2_A = \frac{m_A}{m}(p^2 - p'^2) & (6) \end{cases}$$

(eq.C.1) and (6):

$$(\mathrm{p} - \mathrm{p}'\mathrm{cos}\theta)^2 + \mathrm{p}'^2\mathrm{sin}^2\theta = \frac{\mathrm{m}_\mathrm{A}}{\mathrm{m}}(\mathrm{p}^2 - \mathrm{p}'^2) \tag{C.3}$$

$$(1 + \frac{\mathrm{m}_\mathrm{A}}{\mathrm{m}})\mathrm{p}'^2 - 2\mathrm{p}\mathrm{p}'\mathrm{cos}\theta + \mathrm{p}^2(1 - \frac{\mathrm{m}_\mathrm{A}}{\mathrm{m}}) = 0 \tag{C.4}$$

After solving the quadratic equation we obtain:

$$\mathrm{p}' = \frac{\mathrm{p.cos}\theta}{(1 + \frac{\mathrm{m}_\mathrm{A}}{\mathrm{m}})} \pm \frac{\mathrm{p}}{(1 + \frac{\mathrm{m}_\mathrm{A}}{\mathrm{m}})}\sqrt{(\frac{\mathrm{m}_\mathrm{A}}{\mathrm{m}})^2 - \mathrm{sin}^2\theta} \tag{C.5}$$

For $\frac{\mathrm{m}_\mathrm{A}}{\mathrm{m}} = 1$, the solution with the substraction of the second term leads to p'=0 $\forall$ θ, which is not physical.

The only solution is, therefore:

$$\mathrm{p}' = \frac{\mathrm{p.cos}\theta}{(1+\frac{\mathrm{m_A}}{\mathrm{m}})} + \frac{\mathrm{p}}{(1+\frac{\mathrm{m_A}}{\mathrm{m}})}\sqrt{(\frac{\mathrm{m_A}}{\mathrm{m}})^2 - \sin^2\theta} \tag{C.6}$$

Numerical application in our case:

E'=0.98 E for proton-tungsten and proton-aluminum.

Appendix D

Résumé

PETAL (PETawatt Aquitaine Laser) est un laser positionné dans la sphère du laser MégaJoule LMJ à Bordeaux. Il complète les lasers nanosecondes de LMJ en délivrant des faisceaux picosecondes au sub picosecondes, à une intensité qui pourra atteindre 10^{20} W/cm^2 et permettra d'accélérer les particules (électrons, protons, ions) principalement selon le mécanisme TNSA (Target Normal Sheath Acceleration). Cette thèse porte sur l'étude des détecteurs passifs pour les particules chargées du diagnostic PETAL. Ces détecteurs seront employés plus particulièrement dans SEPAGE (Spectromètres Électrons Protons A Grande Énergie) et SESAME (Spectromètres ElectronS A Moyenne Energie) à LMJ/PETAL. Ces deux diagnostics ont pour but de mesurer les spectres d'énergie des particules accélérées par le laser PETAL (électrons, protons et ions). L'utilisation de détecteurs passifs avec PETAL s'impose par une raison essentielle: l'interaction du laser PETAL avec sa cible va générer, à pleine puissance, une impulsion éléctromagnetique géante dans toute la sphère LMJ qui aveuglera a l'électronique de lecture qui s'y trouve. Les Imaging Plates (IPs) ont été choisis pour cela. Ce choix se justifie par leurs taille legers, son efficacité de detecter les particules chargées dans un grand domaine d'énergie, grande resolution et on peux utiliser ces IPs plusieurs fois. Ces détecteurs doivent être étalonnés pour ces particules dans la gamme d'énergie de 0,1 à $\sim$ 200 MeV, pour laquelle ces diagnostics ont été élaborés.

De plus, les IPs étant sensibles à tout type de rayonnement ionisant, elles devront être protégées, à l'intérieur des diagnostics de particules chargées, contre le bruit de fond des photons génerés soit directement par l'interaction de PETAL avec sa cible soit par l'activation des matériaux de la sphère LMJ−PETAL. Nous avons donc non seulement étudié les réponses des IPs simples mais aussi les réponses de détecteurs composés d'IP et de plaques de matériaux de numéros atomiques élevés tels que le tungstène.

Durant cette thèse, quatre expériences avec quatre sources différentes de particules ont été réalisées et les données expérimentales obtenues ont été analysées et interprétées. Les mesures ont également été comparées avec la littérature.

L'accélérateur TANDEM de l'institut de physique nucléaire d'Orsay nous a fourni une source de protons dans la gamme d'énergie entre 1 MeV et 22 MeV et d'ions de carbone entre 5 et 84 MeV. Cette expérience nous a également permis d'étalonner le transport des particules chargées dans le démonstrateur de la parabole Thomson du "canal à basse énergie" de SEPAGE. La source de synchrotron protonique au Centre de Protonthérapie d'Orsay (CPO) nous a permis d'étudier la réponse des détecteurs aux protons dans la gamme d'énergie de 80 MeV à 200 MeV.

Deux expériences avec les électrons ont couvert le domaine en énergie de 5 à 140 MeV:

- La première à l'accélérateur ELSA de CEA−DAM à Bruyères−le−Châtel pour la partie basse du domaine en énergie
- La seconde au Laboratoire d'Optique Appliquée pour des électrons entre 40 et 180 MeV.

Il était important en effet d'étudier nos détecteurs pour les protons et pour les électrons car dans le domaine en énergie des particules chargées accélérées avec PETAL, les intéractions de ces deux types de particules avec la matiére sont qualitativement différentes.

Deux modèles, qui relient les réponses des détecteurs aux pertes d'énergie moyennes des particules dans la couche active des IPs ont été étudiés pour l'interprétation de nos mesures. Comme les pertes d'énergie des particules à l'intérieur ces couches actives ne sont pas des observables expérimentales, elles doivent être calculées avec des simulations. Pour ce faire, nous avons choisi GEANT4 pour son efficacité à calculer l'énergie déposée dans nos détecteurs, sa rapidité de calcul et sa précision. Il s'agit aussi d'un code dont les prédiction dans l'interaction particules−matières ont été validées par un grand nombre d'expériences.

Avec GEANT4, nous avons extrait de nos mesures le rapport entre les réponses et les pertes d'énergie moyenne des particules pour chaque type de détecteur (MS, SR, TR IPs). Ces sensibilités, combinées avec nos calculs GEANT4, nous ont permis de calculer les réponses du détecteur dans le domaine d'énergie de 0,1 à 1000 MeV, qui décrivent la plupart des données existantes. Ces résultats pourront être utilisés dans le calcul des réponses d'IPs dans le projet PETAL+ et le calcul des détecteurs composites.

La comparaison des sensibilités déterminées pour les protons et les électrons montre des valeurs très semblables pour les types MS et SR. La sensibilité des IP TR est différente pour les électrons et les protons, contrairement aux deux autres types d'IP. Cela reste à expliquer par d'autres experiences.

Nous avons poussé ce concept un peu plus loin avec les mesures des réponses des détecteurs composés de IPs et de couches de matériau à Z élevé. Nos mesures ont montré une augmentation globale des réponses des IPs en présence de telles couches, à la fois devant ou derrière les détecteurs par rapport à la direction des particules entrantes. Nous avons pu prouver qu'une épaisseur de tungstène placée derrière les IPs rend le signal sur les IPs par particule indépendant de la matière qui se trouve au delà. Dans SEPAGE une telle épaisseur permettra de protéger les détecteurs et notre étalonnage rend possible la détermination du nombre absolu des particules détectées.

Ces augmentations sont très bien décrites par l'évolution des pertes d'énergie des particules telles que calculées avec nos simulations GEANT4. Selon le type de particule ainsi que la gamme d'énergie des particules, les contributions à ces augmentations à partir des pertes d'énergie des particules primaires ou des particules d'ordre secondaire ou supérieur provenant des interactions détecteur de particules sont différentes mais peuvent être très importantes.

A l'aide des détecteurs composites épais, nous avons mesuré le pic de Bragg de protons de 160 et 200 MeV (expérience au CPO). La position du pic dans le détecteur et l'évolution du signal dans les différentes IP qui contribuent les détecteurs ont été trés bien déduites avec le modélisation GEANT4 en utilisant uniquement la sensibilité des IPs simples.

Nous avons aussi qualifié GEANT4 avec les options qui vont bien, et qu'on pouvez l'utilisées pour concevoir les détecteurs PETAL+.

Les résultats obtenues avec les sensibilités des IPs simples pour les protons sont en accord avec les données de Bonnet et al. et Mancic et al. Pour les électrons nous sommes en accord avec les données de Chen et al., Bonnet et al. et Nakanii et al.

Nos résultats pourront être efficaces pour des autres installations.

Bibliography

[1] *http : //www−lmj.cea.fr/docs/*2014*/LMJ_PETAL_Users_guide_v*1.0*.pdf*

[2] LMJ−PETAL Scientific Case for academic access program, Institut Lasers−Plasmas and Association Lasers-Plasmas (2014)

[3] Workshop on Basic Research Directions on User Science at the National Ignition Facility, National Nuclear Security Administration, Office of Science (2012)

[4] A. Gurevich et al, Phys. Rev. lett. **42**, 769 (1979)

[5] M.A. True et al, Phys. Fluids. **24**, 1885 (1981)

[6] E.L. Clark et al, Phys. Rev. lett. **84**, 670 (2000)

[7] R.A. Snavely et al, Phys. Rev. lett. **85**, 2945 (2000)

[8] M. Roth and M. Schollmeier, Ion Acceleration - Target Normal Sheath Acceleration, Proceedings of the CAS-CERN Accelerator School: Plasma Wake Acceleration, Geneva, Switzerland, 2014

[9] J. Fuchs et al., Nature Phys 2, **48** (2006)

[10] L. Robson et al., Nature Phys 3, **58** (2007)

[11] D. Batani et al., Acta Politechnica **53**, 103 (2013)

[12] J.-E. Ducret et al., Nucl. Instr. Meth. A **720**, 141 (2013)

[13] DIF/DCRE/SCEP DO203−14

[14] Y. Cauchois, Journal de Physique **3**, 320 (1932)

[15] Report DJC−SEPAGE−LMJ−20000−RXP− CDD−MOS 17982/A.

[16] E. d'Humières et al., Preparation of the high power laser system PETAL for experimental studies of inertial confinement fusion and high energy density states of matter, J. Phys.: Conf. Ser. **688**, 012012 (2016).

[17] D. Jung et al., Rev. Sci. Instrum. **82**, 013306 (2011)

[18] J-E. Ducret, private communication. (2014)

[19] SCEP DO 117-14 . Doc de Synthese Definition SESAME

[20] H. Bouchard, Med. Phys. **36**, 1931 (2009).

[21] $https://en.wikipedia.org/wiki/Photostimulated\_luminescence$

[22] H. Chen et al., Rev. Sci. Instrum. **79**, 033301 (2008)

[23] I. W. Choi, Meas. et al. Sci.Technol. **20**, 115112 (2009).

[24] C. G. Freeman et al. , Rev. Sci. Instrum. **82**, 073301 (2011).

[25] B. Hidding et al., Rev. Sci. Instrum. **78**, 083301 (2007)

[26] J.-P. Nègre, Report CEA-R-6271, ISSN 0429-3460 (2011)

[27] K.A. Tanaka et al., Rev. Sci. Instrum. **76**, 013507 (2005)

[28] T. Bonnet et al., Rev. Sci. Instrum. **84**, 103510 (2013)

[29] T. Bonnet, Doctorate thesis, U. of Bordeaux (2013)

[30] B. G. Cartwright, E. K. Shirk, and P. B. Price, Nucl. Instrum. Methods **153** (1978), p.457-460

[31] S. A. Durrani, and R. K. Bull, Solid State Nuclear Track Detections, Principles, Methods and Applications (Pergamon, New York, 1987)

[32] A. J. Khan et al., Nucl. Tracks Radiat. Meas. **17**, 497 (1990)

[33] Y. Glinec et al, Rev. Sci. Instrum. **77**, 103301 (2006)

[34] H. von Seggern, Nucl. Instr. Meth. A **322**, 467 (1992)

[35] S. Agostinelli et al., Nucl. Instrum. Methods Phys. Res., Sect. A **506**, 250 (2003).

[36] J.D. Jackson, "Classical Electrodynamics", John Wiley and Sons Ltd Eds (1962)

[37] S. Agostinelli et al., Nucl. Instr. Meth. A **506**, 250 (2003)

[38] F. Ingenito, G. Boutoux, M. Cipriani, F. Consoli, G. Cristofari, A. Curcio, R. De Angelis, G. DiGiorgio, J.-E. Ducret, P. Forestier-Colleoni, S. Hulin, K. Jakubowska, N. Rabhi et al. JINST **11** C05012 (2016)

[39] C.J. Joachain and C. Quigg, Review of Modern Physics **46**, 279 (1974)

[40] O. Yevseyeva et al., Comparison of GEANT4 simulations with experimental data for thick al absorbers. AIP Conference Proceedings, v. 1139, p. 97-101.

[41] M. Batic et al., Validation of Geant4 simulation of electron energy deposition. IEEE Transactions on Nuclear Science, vol. **60**, issue 4, pp. 2934-2957

[42] T. Bonnet et al., Rev. Sci. Instrum. **84**, 013508 (2013)

[43] J.A. Rowlands, Phys. Med. Biol. 47, R123 (2002)

[44] H. Ohuchi et al., Nucl. Instr. Meth. A **450**, 343 (2000)

[45] H. Ohuchi and A. Yamadera, Nucl. Instr. Meth. A **490**, 573 (2002)

[46] G. Boutoux, N. Rabhi et al. Rev. Sci. Instrum. **86**, 113304 (2015)

[47] N. Rabhi, K. Bohacek et al., Rev. Sci. Instrum. **87**, 053306 (2016)

[48] R. Weber et al., Rev. Sci. Instrum. **57**, 1251 (1986)

[49] N. Blanchot et al., EPJ Web of Conf. **59**, 07001 (2013)

[50] $https : //www.nist.gov/pml/stopping - power - range - tables - electrons - protons - and - helium - ions$

[51] A. Casner et al., LMJ/PETAL laser facility: Overview and opportunities for laboratory astrophysics, High Energy Density Physics **17**, 2 (2014)

[52] F. Nurnberg et al., Rev. Sci. Instrum. **80**, 033301 (2009)

[53] A. Merouani et al., Int. J. Laser Therapy and Oncology **3**, 3322 (2015)

[54] M. Batic et al., ArXiv 1307-0933 (2013)

[55] V.N. Ivanchekov, GEANT4 collaboration, 3rd Monte-Carlo Conference MC2010, Tokyo (2010)

[56] O. Yevseyeva et al., XXXI Workshop on Nuclear Physics in Brazil, V. Guiranes et al. Eds. (2009)

[57] J.-L. Dubois et al., Phys. Rev. E. **89**, 013102 (2014)

[58] J.-L. Lemaire, Proceedings of LINAC 2004, Lübeck, Germany

[59] W. Mroz et al., Rev. Sci. Instrum. **67**, 1272 (1996)

[60] M. Tabak et al., Phys. Plasmas **1**, 1626 (1994)

[61] A. Rousse et al., Phys. Rev. Lett **93**, 135005 (2004)

[62] A.L Gonzalez et al., Appl. Rad. and Isot. **57**, 875 (2002)

[63] N. Nakanii et al., Rev. Sci. Instrum. **79**, 066102 (2008)

[64] T. Bonnet et al., SPIE **8779**, 8779N-1 (2013)

[65] J. Belloni et al., Nucl. Instrum. Methods. A **539**, 527 (2005).

[66] K. Zeil et al., Rev. Sci. Instrum. **81**, 013307 (2010)

[67] T. Tanimoto et al., Rev. Sci. Instrum. **79**, 10E910 (2008)

[68] J. Sempau et al., Nucl. Instrum. Meth. B **132**, 377 (1997)

[69] https://wci.llnl.gov/codes/tart/nuclearatomic.html

[70] J. Sempau et al., Nucl. Instrum. Meth. B **207**, 107 (2003)

[71] S. Corde et al., Rev. Mod. Phys. **85**, 1 (2013).

[72] J.F. Ziegler and J.P. Biersack (2003), http://www.srim.org

[73] G. E. Giakoumakis and D. M. Miliotis, Phys. Med. Biol. **30**, 21 (1985).

[74] A. Buck et al., Rev. Sci. Instr. **81**, 033301(2010)

[75] E. Esarey, C. B. Schroeder, and W. P. Leemans. Rev. Mod. Phys., **81**, 1229 (2009).

[76] A. Mancic et al., Rev. Sci. Instrum. **79**, 073301 (2008)

[77] http://www.goodfellow.com

[78] GANIL data acquisition: B. Raine et al., "GANIL DAQ General Architecture", GANIL/SPIRAL2 workshop, 10 March, 2010

[79] F. Méot, Zgoubi users' Guide, Report BNL−98726−2012-IR, C-A/AP/470, Brookhaven National laboratory

[80] B.-R. Martin, Nuclear and Particle Physics: An introduction, Wiley, 2006, pages 349-352

[81] Report on the preparation of the TANDEM experiment (2014).